TECHNISCHE
UNIVERSITÄT
WIEN
Vienna University of Technology

Implementation of Longitudinal Phase Space Tomography at MedAustron

DIPLOMARBEIT

zur Erlangung des akademischen Grades

Diplom-Ingenieurin

im Rahmen des Studiums

Physikalische Energie- und Messtechnik

eingereicht von

Katrin Holzfeind, BSc.
Matrikelnummer 11778884

an der Fakultät für Physik

der Technischen Universität Wien

Betreuung: Privatdoz. Dipl.-Ing. Dr.techn. Michael Benedikt
Mitwirkung: Univ.Ass.in DI DI Dr.in techn. Elisabeth Renner, BSc.

Wien, 28. August 2024

Katrin Holzfeind

Michael Benedikt

TECHNISCHE
UNIVERSITÄT
WIEN
Vienna University of Technology

Implementation of Longitudinal Phase Space Tomography at MedAustron

DIPLOMA THESIS

submitted in partial fulfillment of the requirements for the degree of

Diplom-Ingenieurin

in

Physical Energy and Measurement Engineering

by

Katrin Holzfeind, BSc.
Registration Number 11778884

to the Faculty of Physics

at the TU Wien

Advisor: Privatdoz. Dipl.-Ing. Dr.techn. Michael Benedikt
Assistance: Univ.Ass.in DI DI Dr.in techn. Elisabeth Renner, BSc.

Vienna, August 28, 2024

Katrin Holzfeind

Michael Benedikt

Declaration of Authorship

Katrin Holzfeind, BSc.

I hereby declare that I have written this thesis independently, that I have completely specified the utilised sources and resources and that I have definitely marked all parts of the work - including tables, maps and figures - which belong to other works or to the internet, literally or extracted, by referencing the source as borrowed.

Vienna, August 28, 2024

Katrin Holzfeind

Acknowledgements

I want to thank my chair, Michael Benedikt, and express my gratitude to Elisabeth Renner for her guidance and enthusiasm. Furthermore, I want to thank Markus Wolf and Fabien Plassard for their close collaboration, as well as Claus Schmitzer and Tobias Deutsch for their effort and support. This thesis greatly benefited from input from Simon Albright and Florian Kühteubl. I also want to acknowledge the supportive and educational environment established in the ABP and NCR departments at MedAustron.

Lastly, I want to thank my family, close friends and boyfriend supporting me during my studies.

Abstract

MedAustron is an ion therapy facility located in Wiener Neustadt, Austria, which uses third order resonant slow extraction to deliver protons and carbon ions for irradiation. The currently ongoing extensive studies of different extraction mechanisms, as well as general interest in the behaviour of the beam in the longitudinal phase space from injection to extraction motivate the implementation a new diagnostic tool. To further the understanding of longitudinal beam dynamics, orbit pick-up signals are evaluated using longitudinal tomography. This technique, which is well-established in other accelerator facilities, has been successfully implemented at MedAustron. Its iterative reconstruction algorithm relies on longitudinal profiles obtained from orbit pick-ups, along with machine and optics parameters, such as circumference and transition energy. The turn-by-turn data necessary for reconstruction was acquired with two systems: single acquisition distribution system (SADS) and a micro-telecommunication computing architecture (µTCA)-structure. Of particular interest is the comparison between collected data and its reconstruction of the longitudinal phase space of the two acquisition systems, as MedAustron plans to upgrade its low-level radio frequency system using the µTCA-crate. To ensure suitability and adaptability of the measurement set-ups, systematic measurements describing regular operations with clinical beams were undertaken. Additionally, the accuracy of the tomographic reconstruction was evaluated in scenarios where the beam was manipulated and benchmarked against simulation, using the Beam Longitudinal Dynamics (BLonD) tracking code. These mismatched longitudinal phase space distributions were more accurately reconstructed with 1.4× the operationally set, nominal radio frequency (RF) voltage.

Kurzfassung

MedAustron ist eine Ionentherapieanlage in Wiener Neustadt, Österreich, die durch langsame Extraktion mit Resonanzen der dritten Ordnung Protonen und Kohlenstoffionen für die Bestrahlung bereitstellt. Die derzeit laufenden Studien zu verschiedenen Extraktionsmechanismen, sowie das allgemeine Interesse am Verhalten des Strahls im longitudinalen Phasenraum von der Injektion bis zur Extraktion motivieren die Implementierung eines neuen Diagnosewerkzeugs. Zur Vertiefung des Verständnis der longitudinalen Strahldynamik werden Orbit-Pick-Up-Signale mit Hilfe der longitudinalen Tomographie ausgewertet. Diese Technik, die in anderen Beschleunigeranlagen etabliert ist, wurde bei MedAustron erfolgreich eingesetzt. Der iterative Rekonstruktionsalgorithmus stützt sich auf longitudinalen Profile, die aus Orbit-Pick-Up-Messungen gewonnen werden, sowie auf Maschinen- und optische Parameter, wie Umfang und Übergangsenergie. Die erforderlichen Turn-by-Turn Daten wurden mit zwei Systemen erfasst: single acquisition distribution system (SADS) und micro-telecommunication computing architecture (µTCA). Von besonderem Interesse ist der Vergleich zwischen den erfassten Daten und deren Rekonstruktion des longitudinalen Phasenraums von den beiden Erfassungssystemen, da MedAustron plant, sein Low-Level-Readiofrequenz-System mit der µTCA-Struktur aufzurüsten. Um die Eignung und Anpassungsfähigkeit der Messaufbauten sicherzustellen, wurden systematische Messungen mit im Betrieb verwendeten klinischen Strahlen durchgeführt. Zusätzlich wurde die Genauigkeit der tomographischen Rekonstruktion ausgewertet anhand von Szenarien, in denen der Strahl manipuliert wurde, und mit Simulationen des Beam Longitudinal Dynamics (BLonD) Code verglichen. Diese nicht an den Bucket angepassten Verteilungen im longitudinalen Phasenraum wurden besser rekonstruiert mit 1.4× der angenommenen verwendeten radio frequency (RF)-Spannung.

Contents

List of Figures

List of Tables

Acronyms

µTCA	Micro-telecommunication computing architecture.
BLonD	Beam Longitudinal Dynamics.
CERN	European organization for nuclear research.
COSE	Constant optics slow extraction.
CT	Computer assisted tomography.
DSP	Digital signal processor.
EBS	Empty bucket scanning.
ECR	Electron cyclotron resonance.
FB	Flat bottom.
FFA	Fixed field alternating gradient accelerator.
FFT	Fast Fourier-transformation.
FPGA	Field programmable gate array.
FPGAs	Field programmable gate arrays.
FT	Flat top.
GPIO	General purpose input/output.
LHC	Large Hadron Collider.
LINAC	Linear accelerator.
LLRF	Low-level radio frequency.
LXI	LAN extensions for instrumentation.
OAR	Organs at risk.
PSB	Proton Synchrotron Booster.
PU	Pick-up.

PUs	Pick-ups.
PXIe	Peripheral component interconnect extensions express.
RF	Radio frequency.
RFKO	Radio frequency knock-out.
SADS	Single acquisition distribution system.
SFP	Stable fixed point.
SOBP	Spread out Bragg-peak.
SPS	Super Proton Synchrotron.
UFP	Unstable fixed point.

List of Symbols

Symbol	Unit	Remarks
B	T	Magnetic field strength
$\mathcal{C}$	m	Circumference of machine
c	m/s	Speed of light
D_x	m	Dispersion function
E	MeV	Energy of non-synchronous particle
E_0	MeV	Energy of synchronous particle
E_{rest}	MeV	Rest energy
f_{rev}	Hz	Revolution frequency
f_{RF}	Hz	RF frequency
h	-	Harmonic number
l	s	Bunch length
m_0	eV/c^2	Rest mass
p	MeVc or GeVc	Particle momentum
q	N	Particle charge
R_0	m	Average machine radius
T_0	s	Revolution period of synchronous phase
T_r	s	Revolution period
t	s	Time
V	V	Effective voltage of RF cavity
$\mathrm{V}_{\mathrm{nom}}$	V	Operationally set, nominal voltage
v	m/s	Velocity of particle
x, y, z	m	Coordinates in Frenet-Serret coordinate system
α_{c}	-	Momentum compaction factor
β	-	Relativistic factor $\beta = v/c$
δ	-	Relative momentum offset $\Delta p/p$
ϵ_{L}	eVs	Longitudinal emittance
η	-	Slip factor
γ	-	Relativistic Lorentz factor
γ_{T}	-	Transition energy
$\mathcal{E}_0$	V/m	Amplitude of electric field
Φ	rad	Phase of particle

Symbol	Unit	Remarks
Φ_{RF}	rad	Phase of RF cavity
Φ_s	rad	Synchronous phase
ρ	m	Bending radius
θ	rad	Azimuthal angle
ω_0	2π/s	Angular revolution frequency
ω_s	2π/s	Angular synchrotron frequency
ω_{RF}	2π/s	Angular RF frequency
Q_u	-	Transverse ($u = x, y$) and longitudinal ($u = s$) particle tune
Z_t	Ω	Transfer impedance

Introduction

Compared to conventional cancer irradiation therapy based on high-energy X-rays, proton and ion beam therapy centres, like MedAustron, allow treatment of tumors with lower doses to the surrounding healthy tissue. This conformal therapy is possible due to the dose distribution of fast ions in tissue, governed by the Bragg-peak. The range of the Bragg-peak depends on the initial energy of the ion beam. By treating the patient using beams with different energies and scanning the beam in the transverse plane the tumor volume can be actively scanned in three dimensions. Figure A schematically compares the dose-depth distribution, which is achieved with conventional X-ray therapy and therapy using multiple energies to obtain a so-called spread out Bragg-peak (SOBP).

The transverse scanning of the tumor with millimeter precision requires a very stable beam over seconds. The machine at MedAustron utilises third order resonant slow extraction driven by acceleration via betatron core to provide slow and steady spills. This method is only applicable to an unbunched beam. MedAustron is a centre for radiotherapy with proton and carbon ions, as well as a research facility. One way to reduce the patient treatment time is the implementation of multi-energy-extraction [3]. Multi-energy-extraction requires bunched beam extraction, which is incompatible with the betatron core extraction. Different extraction mechanisms such as radio frequency knock-out (RFKO) and constant optics slow extraction (COSE), which allow bunched beam extraction, are under investigation at MedAustron [4]. Throughout these and further studies an extended understanding of the longitudinal phase space is of high value. During these development studies, as well as the beam commissioning, longitudinal properties have been measured using the Schottky frequency analyser and empty bucket scanning (EBS). These measurement methods require long acquisition times over which the measured momentum spread is averaged and only provide the measured momentum distribution, but no illustration of the longitudinal phase space distribution.

A different diagnostic tool, longitudinal tomography [5], uses the turn-by-turn measurements of the longitudinal bunch profile in order to reconstruct the distribution in the longitudinal phase space. It has already been established at different accelerator centres, where it is commonly used for commissioning and machine development activities. Recent examples include the radio frequency (RF) voltage calibration in the Proton Synchrotron Booster (PSB) at CERN [6] and the Super Proton Synchrotron (SPS) [7] and painting of the longitudinal phase space at PSB [8].

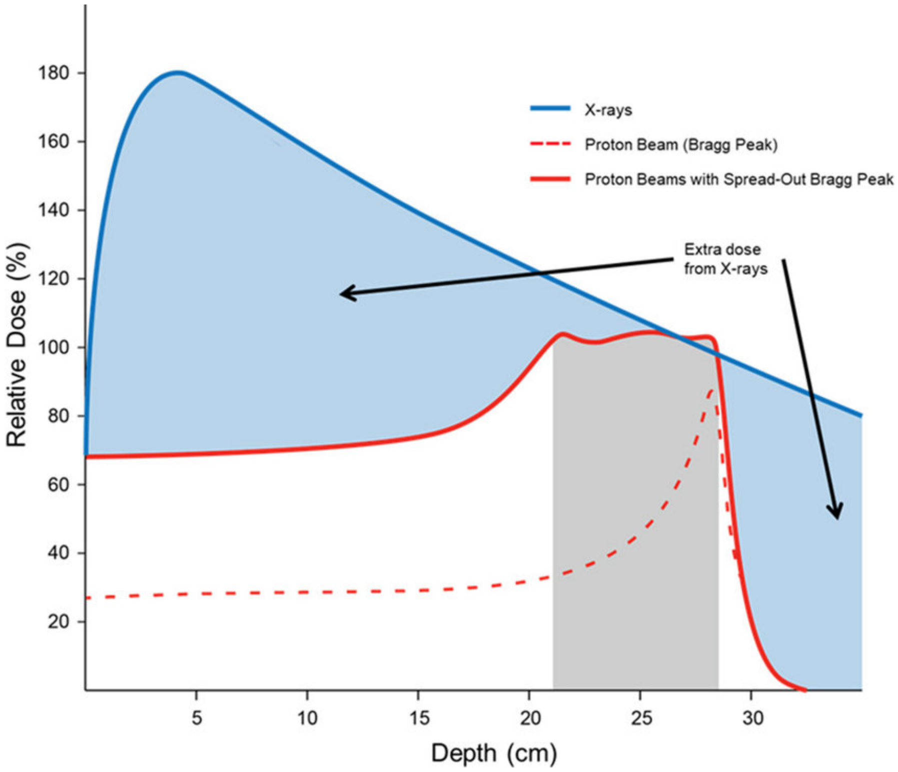

Figure A: Differential depth dose distributions of photons versus protons. Photon beams have the highest dose deposition close to the entrance surface and continuously deposit dose at the whole path throughout the tissue. In contrast, proton beams deposit a lower dose in the entry field, and maximum dose deposition occurs within the so-called Bragg peak or SOBP in clinical applications. The reduced volume of healthy tissue exposed to intermediate and low doses of proton radiotherapy results in a reduced co-irradiation of dose-limiting organs at risk (OAR). Picture and caption taken from [1].

The aim of this thesis is the implementation of longitudinal tomography at MedAustron, a synchrotron-based ion beam therapy centre in Wiener Neustadt, Austria. The possibility to visualise transient behaviour in the longitudinal phase space will benefit the research on novel extraction mechanisms and commissioning activities. Examples of this are the investigation into bunched beam extraction and its successor multi-energy-extraction, as well as multi-harmonic radio frequency (RF) operations, which will be introduced with a planned upgrade of the low-level radio frequency (LLRF) system.

Chapter 1 will address longitudinal beam dynamics, the computational efforts to model them via Beam Longitudinal Dynamics (BLonD) simulations [9] and the intricacies of the longitudinal tomography [10][11]. In Chapter 2 a more detailed overview of MedAustron's facilities and infrastructure will be given. The implementation of longitudinal tomography and its comparison with other measurements methods will be described in Chapter 3. Results of the tomographic reconstructions for the designed test cases and discussion of the findings are presented in Chapter 4.

CHAPTER 1

Longitudinal Beam Dynamics: Theory and Measurement Techniques

This chapter briefly explains the main concepts of longitudinal beam dynamics in a synchrotron. Descriptions and derivation of the equation of motion in longitudinal phase space rely on [2] and [12], as well as [13] and [14]. Furthermore the implementation of the physics in simulations via Beam Longitudinal Dynamics (BLonD) [15][16] and how longitudinal tomography uses the underlying principals to reconstruct a phase space distribution from the measured longitudinal profile are discussed [5][10][11].

1.1 Longitudinal Particle Motion

Particle accelerators use electromagnetic fields to accelerate charged particles to high energies. Collisions of two high energies beams or between a high energy beam and a fixed target are essential in fundamental physics research. Such research applications often require energies up to the TeV range, whereas other applications, such as radiation therapy, advanced imaging techniques and material modification, run with energies below 1 GeV. Electric fields in direction of the charged particle's motion are used for acceleration. In electrostatic accelerators the particle passes the acceleration gap only once, which limits the total achievable energy to the voltage difference of the electrode and ground. Another group of particle accelerators, radio frequency (RF) accelerators, are based on electric fields, which oscillate with radio frequencies in RF cavities. In linear or circular accelerators one or multiple of such cavities are installed. The beam can pass through multiple acceleration gaps or trough the same gap multiple times. The oscillating field has to be synchronised with the arrival time of the passing particles. In circular RF accelerators the particles are guided on a circular trajectory by magnetic fields to arrive back at the acceleration gap. As the particles' energies grow, either the allowed radii or the magnetic field, called B-field, strengths have to increase. In cyclotrons and fixed field alternating gradient accelerator (FFA) the B-field stays constant as the radii change. In synchrotrons the B-field is adapted to keep the particles on one radius. The synchrotron has a ring-like structure, which includes an accelerating block housing an RF cavity. Other main components of the synchrotron are:

- **Dipole magnets**: The dipole bends the charged particles via Lorentz force. B-field strength of the magnets must increase with higher particle energies/momenta,

  $$B = \frac{p}{q\rho} \tag{1.1}$$

  with q being the charge of the particles and ρ the bending radius.

- **Quadrupole magnets**: The quadrupole magnetic force is proportional to the particle's distance to the magnet's centre. Depending on the magnet's orientation the force in the horizontal or vertical plane is focusing, while the other defocuses the beam. Quadrupoles define the linear optics of the machine, especially the betatron tune $Q_{x,y}$, which is the number of transverse oscillations the particles perform along the beamline within one turn in the sychrotron.

- **Sextupole magnets**: The sextupole magnets are mostly usesd to mitigate the chromatic effects, which are defined as "change of linear optics parameter with beam energy" [17].

- **Septa**: The beam has to be injected and extracted from the synchrotron ring. A septum generates two regions one with no field and one with a high homogeneous, electronmagnetic field. This separation allows for spatial- discrimination of the beam and the deflection of specific parts of the beam. For the injection and extraction at MedAustron a magnetic and electrostatic septum are used [18].

- **Kicker magnets**: These magnets have fast field rise and fall times. They are used to create fast ramping orbit bumps for the injection of the beam into the synchrotron. Because the generated field is weaker than the septa's, ripple reduction is very important for kicker magnets [19].

In a synchrotron the revolution frequency f_{rev} and the RF frequency f_{RF} are synchronised, as the particles' energies and radii grow the magnetic field strength B increases. The frequency applied to the accelerating structure f_{RF}

$$f_{RF} = h \times f_{\text{rev}} \tag{1.2}$$

is a multiple of the revolution frequency f_{rev} with the harmonic number h. With Eqs. 1.1 and 1.2 the non-linear relation between f_{RF} and the magnetic field strength B is found to be [20]

$$f_{RF}(t) = \frac{c\,h}{2\pi R_0}\sqrt{\frac{B(t)^2}{B(t)^2 + \left(\frac{m_0}{q\rho}\right)^2}}, \tag{1.3}$$

with R_0 being the mean orbit radius, h the harmonic number and q the charge of the particles. Equation 1.3 defines the frequency applied in the accelerating structure of the synchrotron, the cavities. The cavities are hollow conducting bodies that enable standing electromagnetic waves. Assuming perfectly conducting walls only-loss free modes of the electromagnetic waves are not dampened exponentially [21]. The resonance of the cavities can be driven by the power source.

1.1.1 Energy Gain per Cavity Passage and Synchronous Phase

The alternating electric field in the cavity is synchronised with the passing beam. The synchronicity defining particle is called the synchronous particle with its phase is $\Phi = \Phi_s$, momentum $p = p_0$ and revolution period $T = T_0$. The synchrotron's lattice is designed to optimize this particle's path through the center of all magnets on a closed orbit. As the accelerating electric field is not constant in the cavities, the energy gain depends greatly on the time of arrival at cavity, seen in the equation for the longitudinal electric field of the RF cavity

$$\mathcal{E}(t) = \mathcal{E}_0 \sin\left(h\omega_0 t + \Phi_s\right), \tag{1.4}$$

with $\mathcal{E}_0$ being the amplitude of the electrical field and ω_0 the angular revolution frequency of the sychronous particle. The non-negligible length of the cavity modifies the energy gained

$$\Delta E = q\mathcal{E}_0\beta c\int_{-d/2\beta c}^{d/2\beta c} \sin\left(h\omega_0 t + \Phi_s\right) dt = q\,V \sin\left(\Phi_s\right), \tag{1.5}$$

with d as physical dimension of the RF cavity gap width, q as charge of the particles and β as ratio of the synchronous particle's velocity and the speed of light. V in Eq. 1.5 is the effective voltage seen by the beam and includes the transit time factor

$$T = \frac{\sin\left(\frac{hg}{2R_0}\right)}{\left(\frac{hg}{2R_0}\right)} \tag{1.6}$$

which modifies the RF voltage due to the cavity's dimension. The energy gained per turn

$$\Delta E = v\Delta p = 2\pi R_0 q\rho\frac{dB}{dt} \tag{1.7}$$

is balanced with the change of the B-field. The synchronous phase Φ_s

$$\Phi_s = \arcsin\left(2\pi R_0\rho\frac{\dot{B}}{V}\right) \tag{1.8}$$

is defined by comparing the rigidity equation Eq. 1.1 and the energy gain per turn from the RF cavity Eq. 1.5.

1.1.2 Longitudinal Equation of Motions

The beam consists of many particles, with momenta and revolution frequencies distributed around the synchronous particle. In order to describe deviations from the synchronous particle the parameters $\omega = \omega_0 + \Delta\omega$, $p = p_0 + \Delta p$, $\Phi = \Phi_s + \Delta\Phi$, etc. are introduced. The relative momentum spread $\frac{\Delta p}{p_0}$ is often expressed as δ. The difference in the azimuthal angle $\Delta\theta$, Fig. 1.1, translates to a difference in the revolution frequency

$$\Delta\omega = \frac{d\Delta\theta}{dt} = -\frac{1}{h}\frac{d\Phi}{dt}. \tag{1.9}$$

To relate the difference of the revolution frequency to a difference in energy, the energy change per turn, Eq. 1.5, can be expressed as energy change in regards to time

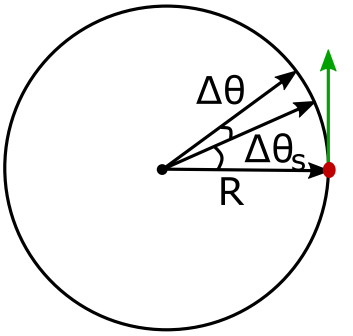

Figure 1.1: Relation of phase and azimuthal angle. Picture taken from [22].

$$\dot{E}_0 = \frac{\omega_0}{2\pi} qV \sin\Phi_s$$

for the synchronous particle. In turn the energy change in regards to time of a particle with a revolution frequency different from the synchronous particle's $\omega \neq \omega_0$ is

$$\dot{E} = \frac{\omega}{2\pi} qV \sin\Phi.$$

The relation, as derived in [22],

$$\Delta(\dot{E}T_\mathrm{r}) \simeq \dot{E}\Delta T_\mathrm{r} + T_{\mathrm{r},0}\Delta\dot{E} = \Delta E\dot{T}_\mathrm{r} + T_{\mathrm{r},0}\Delta\dot{E} = \frac{d(T_{\mathrm{r},0}\Delta E)}{dt} \tag{1.10}$$

of the revolution period T_r and the rate of energy gain $\dot{E}$ is used to derive the equation of motion for the energy in the longitudinal phase space Eq. 1.11.

$$\frac{d}{dt}\left(\frac{\Delta E}{\omega_0}\right) = \frac{qV}{2\pi}(\sin\Phi - \sin\Phi_s) \tag{1.11}$$

Differences in momentum are translated into a difference in path length due to particles

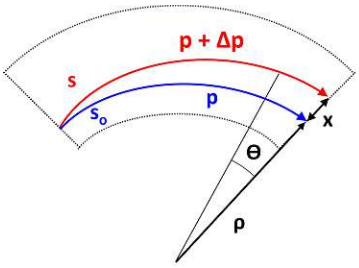

Figure 1.2: Dispersion due to bending particles with different momentum. Picture taken from [22].

with different momenta being bent differently by dipole fields, see Eq. 1.1. The relative path length difference over one revolution for a particle with non-nominal momentum $p + dp$ is calculated by setting the changed path length $ds = (\rho + x)d\theta$ in relation to the reference path $ds_0 = \rho d\theta$, shown in Fig. 1.2. The equation

$$\frac{dl}{ds_0} = \frac{ds - ds_0}{ds_0} = \frac{x}{\rho} = \frac{D_x}{\rho}\frac{dp}{p} \tag{1.12}$$

sets the relation of relative path length difference to the momentum difference by including the dispersion function D_x. The total change dL within one circumference for a particle with relative momentum offset δ is

$$dL = \oint_C dl = \int \frac{x}{\rho} ds_0 = \int \frac{D_x}{\rho}\frac{dp}{p} ds_0. \tag{1.13}$$

The relative change $\frac{dR}{R_0}$ in the average orbit radius is used to define the *momentum compaction factor*

$$\alpha_c = \frac{1}{R_0}\frac{dR}{\delta} = \frac{\langle D_x \rangle_m}{R}, \tag{1.14}$$

with $\langle D_x \rangle_m$ being the dispersion function averaged over all dipole magnets [14]. The momentum compaction factor of linear accelerators is zero as the path length is not impacted by differences in energy. In circular accelerator the momentum compaction factor depends on the optics. At MedAustron the lattice is designed for $\alpha_c > 0$, which makes the path longer for particles with higher energy than that of the synchronous particle. The momentum compaction factor is linked with the *transition energy* γ_T,

$$\alpha_c \equiv \frac{1}{\gamma_T^2}. \tag{1.15}$$

By crossing the transition energy γ_T the conditions for longitudinal stability within the synchrotron change. At MedAustron $Q_x = 1.739$ and $\gamma_T = 1.99$ at injection and $Q_x = 1.67$ and $\gamma_T = 1.97$ at extraction energies [23] are commissioned. The minimum and maximum energy (7 and 800 MeV) at MedAustron lie below the transition energy of the machine, as can be calculated with

$$\beta = \sqrt{1 - \left(\frac{E}{E_{\text{rest}}}\right)^2} \qquad \gamma = \sqrt{\frac{1}{1-\beta^2}} \tag{1.16}$$

to be $\gamma = 1.01$ for 7 MeV and $\gamma = 1.85$ for 800 MeV.

For a synchrotron with the radius R_0 the revolution frequencies is

$$f_{\text{rev}} = \frac{\beta c}{2\pi R_0}, \tag{1.17}$$

which increases with higher energies and decreases with smaller radii. The relative derivative of Eq. 1.17

$$\frac{df_{\text{rev}}}{f_{\text{rev}}} = \frac{d\beta}{\beta} - \frac{dR}{R}$$

can be expressed with the momentum compaction factor α_{c}

$$\frac{df_{\text{rev}}}{f_{\text{rev}}} = \frac{d\beta}{\beta} - \alpha_{\text{c}}\frac{dp}{p}. \tag{1.18}$$

In order to find a relation between the relative change in frequency and the relative change in momentum or energy, an expression for $\frac{d\beta}{\beta}$ with $\frac{dp}{p}$ has to be computed. Using the relativistic momentum

$$p = m_0\gamma\beta c \tag{1.19}$$

and its derivative

$$\frac{dp}{p} = \frac{d\beta}{\beta} + \frac{d\gamma}{\gamma} = \frac{1}{1-\beta^2}\frac{d\beta}{\beta} = \gamma^2\frac{d\beta}{\beta} \tag{1.20}$$

and inserting them into Eq. 1.18 yields the definition of the *slip factor* η in Eq. 1.21.

$$\frac{df_{\text{rev}}}{f_{\text{rev}}} = -\left(\alpha_{\text{c}} - \frac{1}{\gamma^2}\right)\frac{dp}{p} = -\eta\frac{dp}{p} \tag{1.21}$$

An useful relation

$$\frac{\Delta p}{p} = \delta = \frac{1}{\beta^2}\frac{\Delta E}{E} \tag{1.22}$$

is used when combining Eqs. 1.9 and 1.21 for the equations of motions in phase

$$\dot{\Phi} = h\omega_0\eta\delta = \frac{h\omega_0^2\eta}{\beta^2 E}\left(\frac{\Delta E}{\omega_0}\right). \tag{1.23}$$

The two conjugated variables $\left(\Phi, \frac{\Delta E}{\omega_0}\right)$ and their equations of motions can be incorporated in an unified equation motion

$$\frac{d^2}{dt^2}\Delta\Phi = \frac{1}{2\pi}\frac{qV\omega_0^2 h\eta}{\beta^2 E_0}(\sin\Phi - \sin\Phi_s). \tag{1.24}$$

This equation of motion can be linearised for small deviations from the synchronous particle, resulting in a harmonic oscillator. As the amplitude grows the longitudinal motion of the particle around the reference particle becomes non-linear. The restoring potential is only present for some phase offsets. Further discussion of stability in phase space will rely on the stability condition coined by McMillan and Veksler, Eq. 1.25, and a Hamiltonian yielding the equation of motion for energy and phase.

1.1.3 Stability

In this subsection the stability conditions for acceleration will be explained and the concept of the *separatrix* will be introduced. At first the stability conditions will be derived via considerations with the slip factor. The slip factor η, Eq. 1.21, is of great importance when a stable working point has to be set. Below the transition energy ($\gamma < \gamma_T$) higher energies ($\delta > 0$) lead to higher revolution frequencies. The longer path length is compensated by the higher velocity. Exactly at transition energy ω is independent from the momentum offset. For $\eta > 0$ particles with higher energy have smaller revolution frequencies, as the energy is above the transition energy. This observation is the key to the stability condition

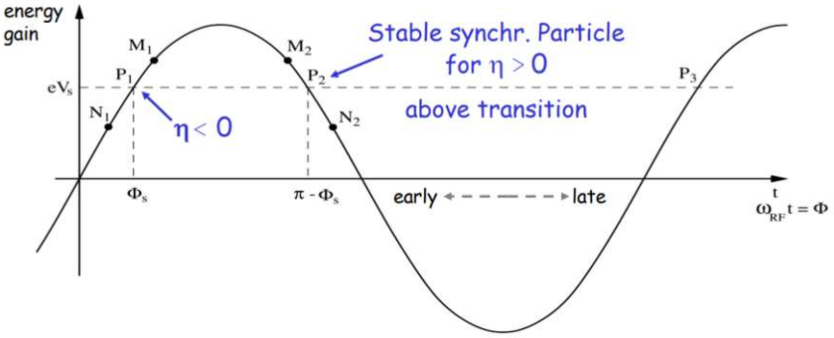

Figure 1.3: Energy gain as a function of particle phase. The oscillations are stable around the synchronous particle P_1 below transition and around the synchronous particle P_2 above transition. Picture and caption taken from [14].

$$\eta_0 \cos(\Phi_s) < 0 \tag{1.25}$$

discovered by McMillan and Veksler (see [2] on page 230). This principle is illustrated in Fig. 1.3.

- $\boldsymbol{\gamma < \gamma_T}$: Below transition the Particle M_1 arrives later then the synchronous particle P_1 with Φ_s and receives a larger kick, gains more energy by passing through the cavity, increasing the revolution frequency. The particle N_1 arrives earlier than the synchronous particle and thus gains less energy than the synchronous particle. In the next turn the M_1 particle arrives earlier and receives less kick and the revolution frequency of the previously early particle N_1 decreased compared to that of the synchronous particle, so that this particle arrives later than the synchronous particle.
- $\boldsymbol{\gamma > \gamma_T}$: Above transition the energy gain depending on the arrival of the particles M_2 and N_2 in reference to the synchronous particle P_2 is reversed.

This condition allows a stable area in the longitudinal phase space called a *bucket* surrounded by the separatrix, which divides stable and unstable regions, see Fig. 1.4. The

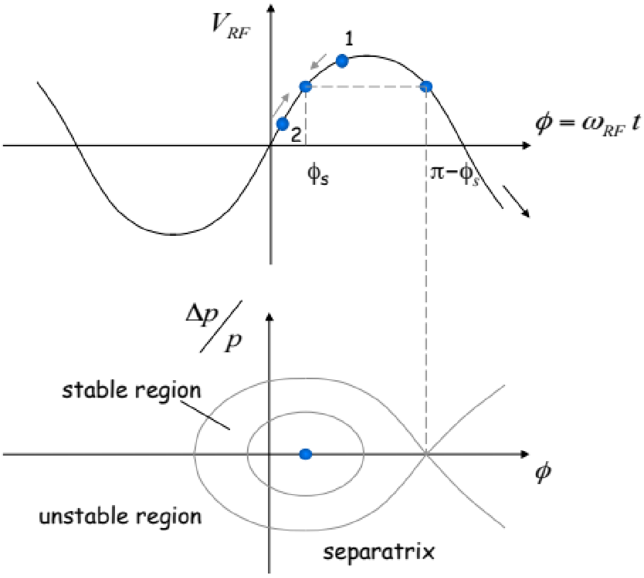

Figure 1.4: RF voltage as a function of particle phase (top) and phase-space picture (bottom) for a non-stationary bucket. Picture and caption taken from [14].

Hamiltonian contour of the stable region features so-called *stable points*: the stable fixed point (SFP) at $(\Phi_s,0)$ and the unstable fixed point (UFP) at $(\pi - \Phi_s,0)$. Small oscillations near the SFP lead to elliptical phase-space trajectories, whereas small oscillations near the UFP follow hyperbolic trajectories. The stable region enclosed by the separatrix is called the bucket. Its shape is defined by the RF voltage, the particle energy and charge, the synchronous phase and machine parameters, such as the momentum compaction factor and circumference. As consequence of this distinction between stable and unstable region, particles can be grouped and accelerated in distinct *bunches*, when the RF system is on. Particles within the bucket perform stable synchrotron oscillations around the SFP.

These particles are called the bunch and beams with this structure are called bunched beams. When the RF system is turned off, the particles' different momenta accumulate into a phase difference over multiple turns. The bunch structure is lost and the beam is called *coasting* or *unbunched beam.*

1.1.4 Synchrotron Oscillations

For small oscillation the aforementioned synchrotron oscillations can be linearised. Linearising the equation of motion, see Eq. 1.24, for small amplitudes in a stationary bucket simplifies it to

$$\frac{d^2}{dt^2}(\Phi - \Phi_s) = \frac{1}{2\pi}\frac{qV\omega_0^2 h\eta}{\beta^2 E_0}(\Phi - \Phi_s), \tag{1.26}$$

which resembles a harmonic oscillator with oscillation frequency ω_s. This longitudinal oscillation frequency is commonly parameterised using the synchrotron tune Q_s

$$Q_{s,0} = \frac{\omega_s}{\omega_0} = \sqrt{\frac{hqV|\eta_0 \cos{(\Phi_s)}|}{2\pi\beta^2 E}}. \tag{1.27}$$

As the amplitude of a particle increases the harmonic oscillator approximation is no

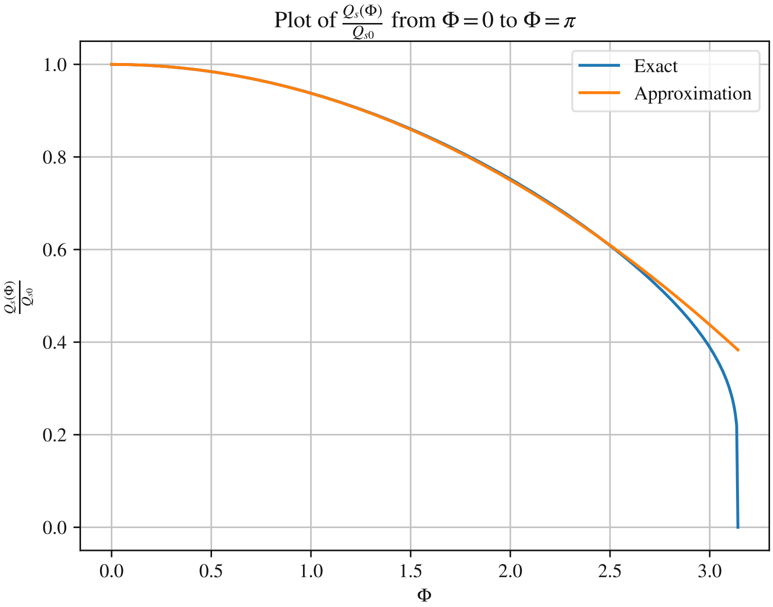

Figure 1.5: Ratio of synchrotron tune of particle with phase amplitude and the central synchrotron tune of the synchronous particle as a function of maximal phase deviation from the SFP in radian. Exact formula (bottom trace, blue) and approximation Eq. 1.29. Non-accelerating bucket ($\Phi_s = 0$) [20].

longer valid. For larger offsets, the synchrotron tune can be derived as [20]

$$Q_s(\Phi) = \frac{\pi \cdot Q_{s0}}{2 \int\limits_0^{\pi/2} \frac{du}{\sqrt{1-\sin^2\left(\frac{\Phi}{2}\right)\sin^2(u)}}}. \tag{1.28}$$

This relation shows that close to the separatrix the synchrotron tune vanishes, meaning that the particle movement in longitudinal phase space slows down. This relation can be used to derive the bunch profile from Schottky spectrum measurements, as shown in [24] and further discussed in chapter Chapter 3. An approximation of Eq. 1.28 [20] for moderate offsets from SFP is

$$Q_s(\Phi) \approx Q_{s0}\left[1 - \left(\frac{\Phi}{4}\right)^2\right]. \tag{1.29}$$

A comparison of the approximation (Eq. 1.29) and the exact equation (Eq. 1.28) can be found in Fig. 1.5, where a good agreement of both equations can be observed from $\Phi = 0$ to $\Phi = 2.5\,\mathrm{rad}$.

The non-linear equation of motion and resulting non-constant synchrotron frequency in the bucket lead to the filamentation of the bunched beam, if the beam's phase space distribution is not matched to the bucket shape. Figure 1.6 shows this phenomenon after many turns. In order to avoid this filamentation the beam and the RF bucket have to be matched.

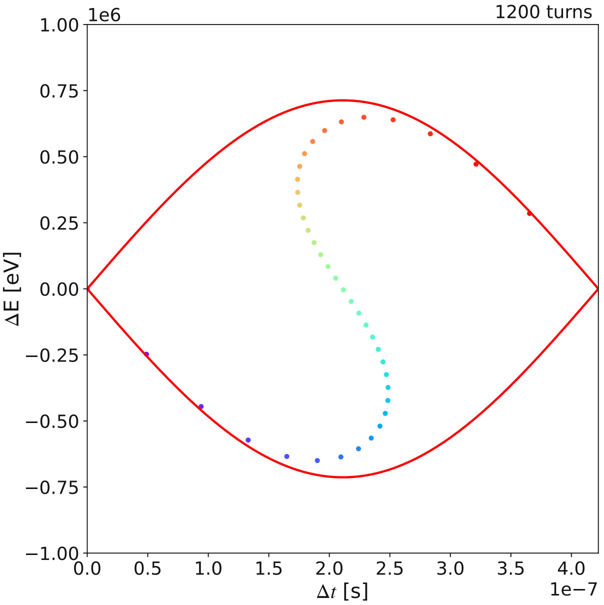

Figure 1.6: Filamentation in phase space after 1200 turns after initialising all particles with no energy offset and different phase offsets.

1.1.5 Hamiltonian and Separatrix

The equations of motions Eqs. 1.11 and 1.23 can be derived from a Hamiltonian with the canonical variables $(\Phi, \frac{\Delta E}{\omega_0})$

$$H = \frac{1}{2}\frac{h\omega_0^2\eta_0}{\beta^2 E}\left(\frac{\Delta E}{\omega_0}\right)^2 + \frac{qV}{2\pi}[\cos(\Phi) - \cos(\Phi_s) + (\Phi - \Phi_s)\sin(\Phi_s)]. \tag{1.30}$$

With the Hamiltonian, the separatrix can easily be determined. The separatrix crosses $\delta = 0$ at the UFP and the Hamiltonian-potential can be calculated via the conditions for no movement of the specific points

$$\dot{\Phi} = \frac{\partial H}{\partial\left(\frac{\Delta E}{\omega_0}\right)} = 0 \qquad \left(\frac{\Delta\dot{E}}{\omega_0}\right) = -\frac{\partial H}{\partial \Phi} = 0. \tag{1.31}$$

We obtain the SFP at $\Phi = \Phi_s + n \times 2\pi$ and $\delta = 0$ and UFP at $\Phi = \pi - \Phi_s + n \times 2\pi$ and $\delta = 0$. These points correspond to a minimum and a maximum in the potential well as seen in Fig. 1.7, which shows the potential as described in the Hamiltonian in the lower plot. The restoring force is non-linear, which is reflected in Eq. 1.28. As the synchronous phase changes, the potential well changes as well. This in turn changes the shape of the bucket. The separatrix equation is obtained by the Hamiltonian $H = H_{\text{sep}}$, which passes

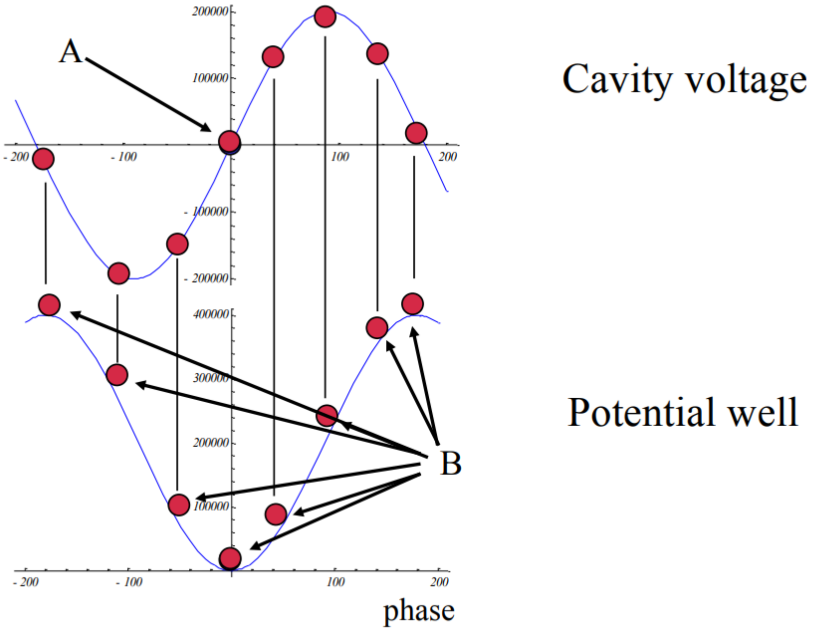

Figure 1.7: Relation between the RF voltage (top) and the potential well (bottom). Picture taken from [14].

through the UFP,

$$\delta_{\text{sep}}^2 + \frac{qV}{\pi h \eta E \beta^2}[\cos(\Phi_s) + \cos(\Phi) - (\pi - \Phi - \Phi_s)\sin(\Phi_s)] = 0. \tag{1.32}$$

The height of the bucket is called the energy or momentum acceptance. Its phase coordinate is at the SFP. In a stationary bucket ($\Phi_s = 0$) the maximum acceptance is

$$\delta_{\max} = 2\left(\frac{qV}{2\pi\beta^2 Eh|\eta|}\right)^{1/2} \tag{1.33}$$

and its bucket area, enclosed by the separatrix, can be calculated with

$$A = 16\left(\frac{qV}{2\pi\beta^2 Eh|\eta|}\right)^{1/2}. \tag{1.34}$$

Changing the synchronous phase for acceleration, the bucket becomes a *running bucket*. Its fixed points are shifted and its area decreases (for constant RF voltage). Equations 1.33 and 1.34 are modified by the bucket height factor $Y(\Phi_s)$ and the bucket area factor $\alpha_b(\Phi_s)$ respectively. Their values can be found in Table 1.1 for different synchronous phases. The difference between *stationary* and running bucket is visualised in Fig. 1.8.

$\sin\Phi_s$	Φ_u	$\pi - \Phi_s$	$Y(\Phi_s)$	$\alpha_b(\Phi_s)$
0.00	-180.00	180.00	1.0000	1.0000
0.10	-118.90	174.26	0.9208	0.8041
0.20	-93.71	168.46	0.8402	0.6611
0.30	-73.59	162.54	0.7577	0.5388
0.40	-55.66	156.42	0.6729	0.4305
0.50	-38.69	150.00	0.5852	0.3333
0.60	-21.88	143.13	0.4936	0.2460
0.70	-4.48	135.57	0.3967	0.1679
0.80	14.59	126.87	0.2919	0.0991
0.90	37.77	115.84	0.1731	0.0408
1.00	90.00	90.00	0.0000	0.0000

Table 1.1: Turning point (Φ_u in degree), UFP ($\pi - \Phi_s$ in degree), bucket height factor $Y(\phi_s)$ and bucket area factor $\alpha_b(\phi_s)$. Table taken from [2]. The separatrix has two points where $\delta = 0$: Φ_u and the UFP.

1.1.6 Mismatched Beams, Coherent Oscillations and Filamentation

A matched beam does not typically occupy the whole bucket. Each particle has its energy and phase or time coordinates. The distribution of the particles are of importance. The area the beam occupies in phase space is called the longitudinal *emittance* ϵ_{L}, which is defined as

$$\epsilon_{\text{L}} = \pi\sigma_E\sigma_t \tag{1.35}$$

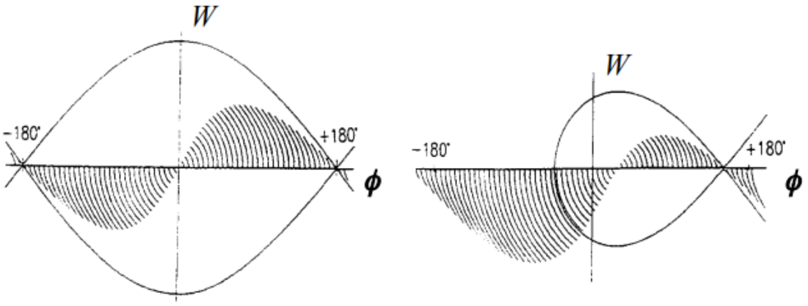

Figure 1.8: Phase-space trajectories for 1/8 of the synchrotron period for a stationary (left) and an accelerating bucket (right). Picture and caption taken from [14].

in this thesis. The units of the longitudinal emittance are eVs. For a matched beam the particle distribution fits the bucket shape, so that, while each particle oscillates around the SFP, the area the entire beam occupies does not change. This bunch is characterised with a *bunch length*, which is defined as $4 \times \sigma_t$ in this thesis. As seen before in Fig. 1.6 the stable conditions are dependent on the beam's physical dimensions and RF parameters such as voltage and phase.

An example of a mismatch is a decline in voltage for a former matched beam. The bunch shape in the longitudinal phase space no longer fits the bucket shape. First the bunch starts to oscillate in phase space performing coherent bunch oscillations. Due to non-linear forces the phase space distribution dilutes. This so-called *filamentation* results in a new equilibrium distribution, matched to the new bucket shape but with increased longitudinal emittance. While changing from a stationary to a running bucket the stable bucket area also decreases, which can result in losses if the longitudinal emittance exceeds the shrinking acceptance.

A sudden increase in the voltage is shown through BLonD simulations in Fig. 1.9. The oscillations stemming from the mismachted phase space distribution are called quadrupolar-mode oscillations. The change from high momentum spread and small bunch length to small momentum spread and long bunch length happens at twice the synchrotron frequency. The center of mass does not change for these oscillations.

If an offset of Φ_{RF} and Φ_s is introduced the whole bunch is shifted away from the bucket centre. These oscillations are called dipolar-mode oscillations and their frequency is the synchrotron frequency. The particle follow the iso-Hamiltonian lines from their position. This is used in the phase jump at MedAustron, see chapter 2. Figure 1.10 illustrates oscillations simulated with BLond. The filamentation of the distribution due to the non-linear equation of motion and the resulting change in synchrotron tune with offset is well visible.

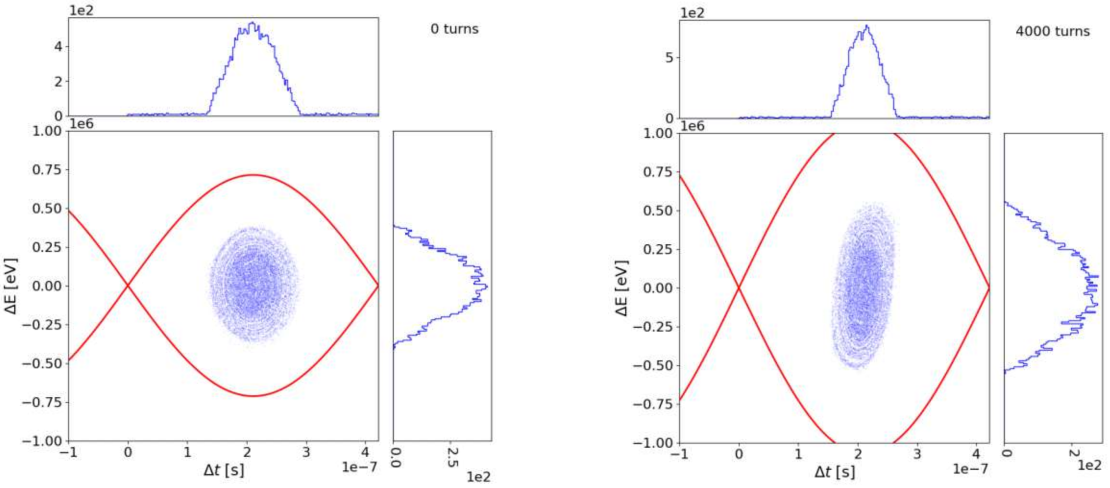

a) b)

Figure 1.9: BLonD simulations: a) Matched beam and b) sudden voltage increase leads to mismatched beam and rotation of the particles distribution in the longitudinal phase space.

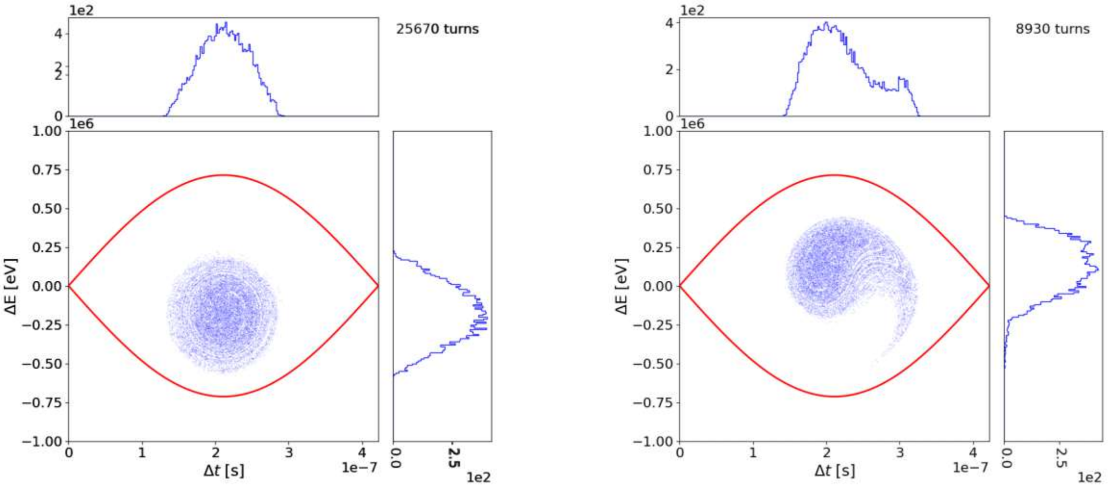

a) b)

Figure 1.10: BLonD simulations: a) Initial mismatched beam with energy offset, b) the beam starts to filament.

1.2 Introduction to BLonD Simulations

The described 2D longitudinal particle motion can be simulated using dedicated simulation codes. This section provides a brief introduction to the Beam Longitudinal Dynamics (BLonD) simulation framework. Further details can be found in [15] and [16].

First the machine is modeled using the lattice parameters, such as machine circumference and momentum compaction factor. The BLonD ring module allows for the initialisation of different sections with an RF station each if necessary. These sections are noted with the index k. If only one RF station needs to be modeled the whole ring can be initialised with the circumference, the linear momentum compaction factor, the particle type, including charge and rest energy and information on the synchronous particle. The information on the energy of the synchronous particle can be given in momentum in eV, the kinetic or total energy in eV or the bending field on the design orbit in T with the bending radius.

```
blond.input_parameters.ring.Ring(ring_length, alpha_0, synchronous_data,
    Particle, n_turns=1, synchronous_data_type='momentum', bending_radius=
    None, n_sections=1, alpha_1=None, alpha_2=None, RingOptions=<blond.
    input_parameters.ring_options.RingOptions object>)
```

An external reference clock time is defined as the summation of the revolution time across turns, $t^n_{\mathrm{ref}} = \sum_{i=1}^{n} T_0^i$. The RF station is defined as

```
   blond.input_parameters.rf_parameters.RFStation(Ring, harmonic, voltage,
    phi_rf_d, n_rf=1, section_index=1, omega_rf=None, phi_noise=None,
    phi_modulation=None, RFStationOptions=<blond.input_parameters.
    rf_parameters_options.RFStationOptions object>)
```

with the ring class mentioned before, the harmonic number h of the RF system, the RF cavity voltage V_0, the designed RF cavity phase, etc. As initial condition the phase of the sinusoidal RF wave

$$V_{\mathrm{RF},0}(t) = V_0 \sin\left(\omega_{\mathrm{RF},k} t\right) \tag{1.36}$$

of the main RF system was chosen to be zero at $t = 0$. The arrival time of any particle n at the RF station is defined relative to the reference time in that turn. The phase of the RF voltage of cavity system k at the arrival time is

$$\phi_{\mathrm{RF},k}(t^{(n)} - t^{(n)}_{\mathrm{ref}}) = \sum_{i=1}^{n} 2\pi h_k^{(i)} \frac{\omega^{(i)}_{\mathrm{RF},k} - h_k^{(i)} \omega_0^{(i)}}{h_k^{(i)} \omega_0^{(i)}} \tag{1.37}$$

for the most basic use case with no phase offset and phase noise. A beam is initialised by

```
    blond.beam.beam.Beam(Ring, n_macroparticles, intensity)
```

with the ring module, the total number of macro particles and the total intensity of the beam in number of charges. The beam class holds the beam arrival times with respect to the synchronous time dt in seconds and the beam energy offset with respect to the synchronous particle dE in eV. For each turn the energy gained is calculated for the energy offset with regards to the synchronous energy in the C++ script [25] below.

```
extern "C" void kick(const real_t * __restrict__ beam_dt,
                       real_t * __restrict__ beam_dE, const int n_rf,
                       const real_t * __restrict__ voltage,
                       const real_t * __restrict__ omega_RF,
```

```
                        const real_t * __restrict__ phi_RF,
                        const int n_macroparticles,
                        const real_t acc_kick) {

// KICK
for (int j = 0; j < n_rf; j++)
    #pragma omp parallel for
    for (int i = 0; i < n_macroparticles; i++)
        beam_dE[i] = beam_dE[i] + voltage[j]
                    * FAST_SIN(omega_RF[j] * beam_dt[i] + phi_RF[j]);

// SYNCHRONOUS ENERGY CHANGE
    #pragma omp parallel for
    for (int i = 0; i < n_macroparticles; i++)
        beam_dE[i] = beam_dE[i] + acc_kick;

}
```

The arrival time drift is calculated by

$$\Delta t_{(n+1)} = \Delta t^{(n)} + T_0^{(n+1)} \left(\frac{1}{1 - \eta(\delta^{(n+1)})\delta^{(n+1)}} - 1 \right). \tag{1.38}$$

After each turn the tracker module

```
    blond.trackers.tracker.RingAndRFTracker(RFStation, Beam, solver=’simple’,
     BeamFeedback=None, NoiseFeedback=None, CavityFeedback=None, periodicity=
    False, interpolation=False, Profile=None, TotalInducedVoltage=None)
```

applies the kick function and the drift function, with $\eta(\delta^{(n+1)})$ as defined by the momentum compaction factors and the reference energy in the ring class.

A typical simulation output is seen in Fig. 1.11. The setup of the BLonD simulation for the synchrotron at MedAustron will be discussed in further detail in Chapter 2.

1.3 Introduction to Longitudinal Tomography

The longitudinal tomography algorithm, provided by CERN, can be used to reconstruct the 2D longitudinal phase space from a non-invasive beam profile measurement. In this section the theoretical background to the implementation at MedAustron will be presented.

1.3.1 Tomography and Radon Transform

The word *tomography* is appropriately named after the old-greek words for cut and writing/depiction, as it is a technique to reconstruct an n-dimensional object from its $(n-1)$-dimensional projections. The mathematical foundation for tomography was developed by Johann Radon in 1917 [26] and will schematically be described in the following paragraph with the references [26][27].

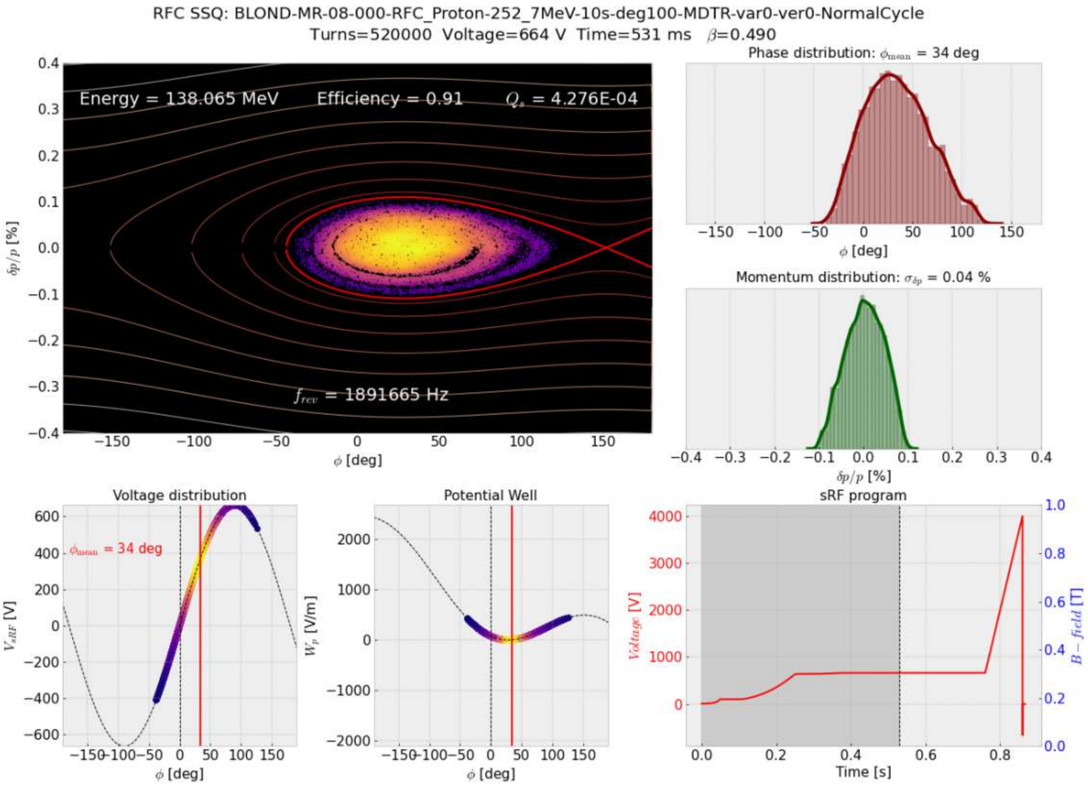

Figure 1.11: BLonD simulation of an operational 252.7 MeV proton cycle at MedAustron.

By slicing the object by all families of parallel lines characterized in the Cartesian system by

$$x\cos(\phi) + y\sin(\phi) = \rho \tag{1.39}$$

with the angle ϕ between the line and horizontal axis and ρ as the distance from the origin, the Radon transform r can be defined as the line integral of the field μ along the line $\delta(\rho - x\cos(\phi) - y\sin(\phi))$, shown in Eq. 1.40. This equation encompasses the fundamental problem: The expression of $\mu(x, y)$ by its Radon transform [27].

$$r_\mu(\rho, \phi) = \int_{L(\rho,\phi)} \mu \, ds = \int_{-\infty}^{\infty}\int_{-\infty}^{\infty} \mu(x, y)\, \delta(\rho - x\cos(\phi) - y\sin(\phi))\, dx\, dy \tag{1.40}$$

Applying a Fourier transformation to $r_\mu(\rho, \phi)$ to $R_\mu(k, \phi)$, the Fourier Slice Theorem

$$R_\mu(k, \phi) = \sqrt{2\pi} F(k\cos(\phi), k\sin(\phi)) \tag{1.41}$$

can be applied, where (k_1, k_2) is the 2D-Fourier-Transformation of $\mu(x, y)$. Calculating the 2D inverse Fourier Transformation of (k_1, k_2) yields the desired $\mu(x, y)$.

1.3.2 Longitudinal Tomography in Particle Accelerators

This principle can be applied to the longitudinal profiles, obtained from the induced signal in a wall pick-up monitor, described in further detail in Chapter 3. The turn-by-turn measurement of the particles as they perform their synchrotron motion is comparable to the patient in the computer assisted tomography (CT)-machine. A code developed at CERN [5][10][11] enables a simple implementation of longitudinal tomography to reconstruct the longitudinal phase space from measurements. The profiles chosen for tomography should span at least half a synchrotron period. The bins, which define the time resolution within an RF period, thus of one bunch profile, should be small enough to resolve the bunch structure. The number of profiles should approach the number of bins within one bunch profile for a successful reconstruction. Requirements on the hardware side are sufficient bandwidth for the resolution of the bunch structure and a good low-frequency response to establish the no-beam baseline [5]. These requirements show that the tomographic reconstruction is not suitable for ultra-relativistic machines such as the Large Hadron Collider (LHC) at CERN. The bunch-length becomes too small (2.5 ns) to be accurately described by the tomography. With a synchrotron tune of 1.9×10^{-3} at collision energy [28], a sampling rate of 200 GS/s would be necessary for an accurate tomographic reconstruction. Standard bunch lengths of electrons in circular accelerators are in the 10-100 ps-range, which is even smaller than the LHC- bunches. The tomography algorithm is best used for low- or mid-β hadron circular accelerators, such as the synchrotron at MedAustron.

CERN Code

The implementation of longitudinal tomography requires knowledge of some beam and machine parameters to initialize a machine object, that stores voltage-, B-field-, slippage factor and other machine-values for each turn. The necessary user input is described in the documentation of the Python rewritten FORTRAN-based tomography code [11], as well as in Chapter 3. The reconstruction is based on ART [29]. The ART relies on iterative back-projection and projection. The contents of one bin in the projection is shared by all cells in the 2-dimensional array that could have contributed. The coefficients used to distribute one bins content along the cells in the projected path can be used to calculate a new projected profile. This allows coherent and efficient transformation between forward and backwards projection. The ART assumes linear and rigid motion in the reconstructed phase space. This is circumvented by the introduction of test particles. If the particles are uniformly distributed within the cell in the phase space, the redistribution coefficients are calculated by counting the particles in column of cells. This approach requires the tracking of particles for all time instances in the reconstruction set.

The induced voltage signal from the pick-up (PU), see Section 3.1.1, is transformed into a *Profile* object, which holds the baseline-corrected and normalised measurement data in an M×N-array, where M is the number of turns and N the number of measurement points, i.e. bins, per turn. The input can also include the time bin (can be a float) of the synchronous phase or its location can be ascertained by a linear fit within the tomography framework.

From the given parameters, the reconstruction area limits and the size of a time and energy bin, dt_{bin} and dE_{bin}, are calculated. This is called the *MapInfo* object. The next object, the *ParticleTracker*, populates the phase space with particles. The particle distribution can either be determined by user-inputs or the *ParticleTracker* allows the population of either all of the phase space or within the separatrix.

The phase space is divided into cells whose energy and time division depended on the time resolution of the measurement, the length of the provided profiles and energy limits of the reconstructed phase space. The particles' path through the cells will be tracked with the kick-and-drift mapping equations [2]

$$\Delta E_{n+1} = \Delta E_n + qV(\sin(\Phi_n) - \sin(\Phi_s)), \tag{1.42}$$

$$\Phi_{n+1} = \Phi_n + \frac{2\pi h\eta}{\beta^2 E}\Delta E_{n+1} \tag{1.43}$$

for each turn. The coordinates for each particle at each turn are stored. After the tracking to the last profile is completed the physical coordinates are transformed into phase-space coordinates x_p and y_p

$$x_p = \frac{\Delta\Phi_{\text{tracked}} + \Phi_{0_i}}{h\omega_{0_i} dt_{\text{bin}}} - x_{\text{origin}}, \tag{1.44}$$

$$y_p = \frac{\Delta E_{\text{tracked}}}{dE_{\text{bin}}} + y_{\text{origin}}, \tag{1.45}$$

with x_{origin} and y_{origin} being the phase-space coordinates of the synchronous particle. This allows the parallelisation of the tracking process.

Algorithm

The back-projection, projection and creating of difference profiles are the fundamental steps of the reconstruction algorithm. They work by adjusting the weight and thus the contribution to the projected profile of each particle. Through iteration, this projection onto the time axis and its difference to the original longitudinal profiles are used to create a back-projection, a phase space distribution, that minimises the difference [30]. This process is visualised in Fig. 1.12.

- **Back-Projection**: In the first iteration the weight of each particles is assumed to be the sum of its contributions over all measured profiles. The initial weight W_i for the particle i

$$W_i = \sum_{j=0}^{N} P_j(X_{i,j}) \tag{1.46}$$

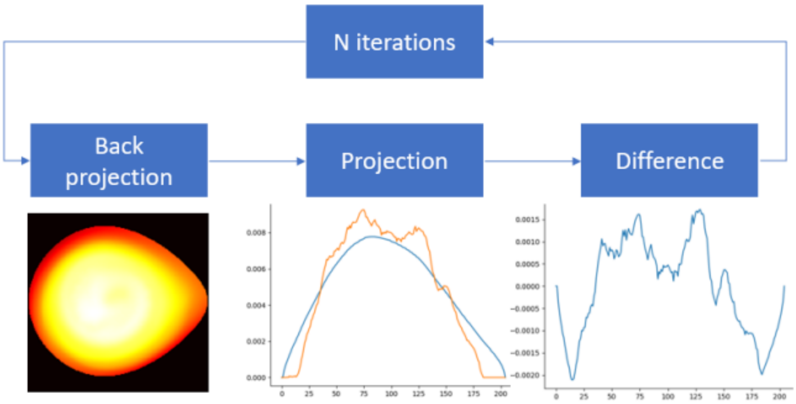

Figure 1.12: The tomography algorithm. Picture and caption taken from [11].

is calculated by summation of the contribution of bin $X_{i,j}$ to the jth profile P_j over all measured profiles N [30].

- **Projection**: A histogram of the assumed phase distribution is created and normalised to be compared to the measured profile. The nth bin of the jth reconstructed profile $\overline{P_{j,n}}$

$$\overline{P}_{j,n} = \sum_{i=0}^{M} w, w = \begin{cases} W_i, & \text{if } X_i, j = n \\ 0, & \text{otherwise} \end{cases} \tag{1.47}$$

  is calculated by the summation of all contribution to the profile bin over all tracked particles M [30]. All reconstructed profiles are normalised by dividing through the summation of bins in one profile.

- **Differences**: The differences between the normalised measured profiles $P_{j,n}$ and the reconstructed profiles $\overline{P}_{j,n}$ are given by $\Delta P_{j,n}$. The weight of each particle is adjusted according to their difference and the ratio of the maximum number of particles M_{max} to particles in the bin M_n. The factor $\frac{M_{\text{max}}}{M_n}$ is included to mitigate effects of non-homogeneous particle distribution. The resulting profile

$$\Delta\tilde{P}_{j,n} = \Delta P_{j,n} \frac{M_{\text{max}}}{M_n} \tag{1.48}$$

  is used as input for the next iteration of back-projection [30].

The quality of the reconstruction is measured with the *discrepancy*

$$d = \sqrt{\frac{\sum_{j=0}^{N} \sum_{n=0}^{M} \Delta P_{j,n}^2}{NM}} \tag{1.49}$$

defined as the root-mean-squared error with N the number of profiles and M the number of bins.

CHAPTER 2

MedAustron Facility Overview

This chapter will give an overview of the facilities at MedAustron, relying on [31] with a focus on the radio frequency (RF) operations. This includes BLonD [15][16] simulations of the longitudinal particle motion in the synchrotron at MedAustron and the frequency regulation of the low-level radio frequency (LLRF) system and its planned upgrade.

MedAustron is a cancer irradiation centre. It is a synchrotron based facility with three irradiation room used for medical treatment and one for non-clinical research. Currently proton and carbon ions are available for cancer therapy, with energy ranges of 62.4-252.7 MeV and 120-402.8 MeV/u, respectively. The first irradiation room in Fig. 2.1 is dedicated to non-clinical research and development. For this room proton beams of low intensity and high energy (800 MeV) [32] and helium beams [33] have been commissioned in addition to medical beams. The complex comprises three separate ion sources, one for helium, carbon and protons, respectively. All three ion sources are electron cyclotron

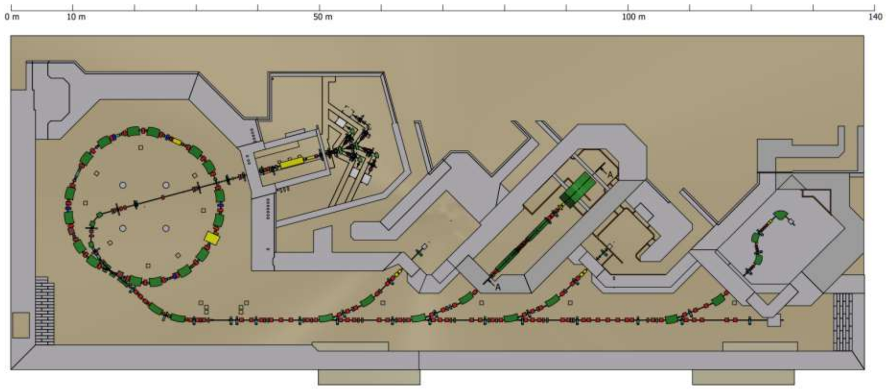

Figure 2.1: Layout of the accelerator complex at MedAustron.

resonance (ECR) sources and extract the ions at 8 keV/u. An RF quadrupole accelerates the beam to 400 keV/u. After a buncher cavity, the beam is then accelerated in an interdigitidal H-mode drift tube linear accelerator (LINAC) to 7 MeV/u [34]. Before being injected into the synchrotron the energy of the injected beam can be tailored using a debuncher cavity. This cavity decreases the energy spread, as the bunch length increases. The beam is injected into the synchrotron using a multi-turn injection scheme. After injection the coasting beam is then captured and accelerated. During clinical operation the beam is extracted via third order resonance, which requires a large energy spread in an unbunched beam, for a slowly extracted beam with stable particle rate. To fulfill these requirements a phase jump of 180° is implemented, in which the bunch elongates along the separatrix, and then debunched. For each patient a treatment plan is created, which specifies the doses each cancer tissue volume should receive. The beam actively scans the cancer tissue volume. The particle's deposited doses along its penetration is mathematically described by the Bragg curve [35]. Its distinctive peak depends on the particle's energy. Scanning the tumor tissue with a precision of sub-millimeters thus requires specific energies and high spatial accuracy, as well as high intensity stability over 1-10 s.

2.1 Synchrotron Radio Frequency System

This section provides a brief overview over the synchrotron RF sytstem at MedAustron. The RF system currently operates the one cavity in the ring with single harmonic mode. The 0.47-3.26 MHz Finement® loaded wideband cavity is driven by 12 × 1 kW solid state power amplifiers, which are connected to the LLRF system [36].

The available frequency range would also allow operations with the second harmonic, which will be tested with the upgrade of the LLRF system [37]. The frequency of the RF cavity increases with increasing energy and magnetic field strength, as described in Eq. 1.3. At MedAustron three loops are engaged to regulate the RF frequency. These loops, used to control the beam's phase and energy, are implemented in the LLRF system.

2.1.1 Radio Frequency Cavity Loop

The first loops that ensures the RF stability is the cavity loop, as described in [38]. The cavity is driven by RF power amplifiers, for example a klystron. A probe detects the RF signal of the cavity, which is evaluated in the field detector. An RF field controller ensures amplitude and phase stability of the cavity's field. The regulations systems should correct for random errors such as phase jitters, bunch charge fluctuations, etc. with feedback and applying feed forward to compensate systematic errors such as Lorentz force detuning and beam loading. The regulation can lock unto different parameters to describe RF, examples for this is the phase and amplitude regulation or the I and Q-regulation (imaginary and real-component of the RF signal).

2.1.2 Phase and Radial Loop

As described above, the RF frequency defines the particle revolution frequency. The frequency and phase with respect to the particle bunch are regulated using the feedback loops of the LLRF system, the radial and phase loop, respectively. Further information on the design and functionality of the loops can be found in [20].

To correct differences between the beam and cavity phase the phase loop introduces a small $\delta\omega$ modulation into the linearised synchrotron oscillation (Eq. 2.1).

$$\frac{d^2\langle\hat{\Phi}\rangle}{dt^2} + \omega_s^2\langle\hat{\Phi}\rangle = \frac{\delta\omega}{dt} \tag{2.1}$$

The phase loop uses the phase error between cavity sum and the beam measured by longitudinal pick-ups to apply a linearly proportional dampening factor, $\delta\omega = -k_\phi\langle\hat{\Phi}\rangle$. $\langle\hat{\Phi}\rangle$ is the phase difference average over all bunches. This loop must react fast to avoid filamentation. The main goal of the phase loop is to preserve emittance, thus it follows the beam's lead.

To keep the beam centred on the reference orbit a radial loop is employed. The controlling parameter is the radial position error average $\langle\hat{R}\rangle$, measured from transversal pick-ups, by comparing the sum and delta signal recorded. The correction of the RF frequency combines the phase and radial loop in $\delta\omega = -k_\phi\langle\hat{\Phi}\rangle - k_R\langle\hat{R}\rangle$. With the momentum compaction factor Eq. 1.14 and inserting the modulation $\delta\omega$ into the linearised synchrotron motion equation yields

$$\frac{d^2\langle\hat{\Phi}\rangle}{dt^2} + k_\phi\frac{\langle\hat{\Phi}\rangle}{dt} + \left(\omega_s^2 + k_R\frac{qV\cos(\Phi_s)}{2\pi\, p\,\gamma_T^2}\right)\langle\hat{\Phi}\rangle = 0. \tag{2.2}$$

In contrast to the phase loop, the radial loop does not dampen the frequency, but increases or decreases the frequency.

2.1.3 Upgrade of the Synchrotron Low Level Radio Frequency System

The current RF operation at MedAustron is described in [36]. As the components of the current LLRF system reach their end of life, an upgrade is foreseen in the coming years. The current systems consists of three VME carrier boards each holding an ADSP-21368 SHARP digital signal processor (DSP) and two Xilnix Virtex5 field programmable gate arrays (FPGAs). As these components reach their end of life, the LLRF system will be upgraded using a micro-telecommunication computing architecture (µTCA)-based platform controlled by the existing MedAustron control system based on peripheral component interconnect extensions express (PXIe). A similar upgrade is also performed for the injector and its beam transfer lines [37][39]. The modular approach allows connection to components, such as the beam interlock system, which will improve the robustness of the accelerator. The same hardware can be used for time-of-flight measurements in the injector complex and has many application in the synchrotron such as: Beam position measurements with the shoebox pick-up (PU), Schottky monitor measurements and control over the radio frequency knock-out (RFKO) extraction.

Advantages of using the µTCA-crate based LLRF system are the reduction of hardware components and the enabling of higher RF harmonics. The current system can only provide a single harmonic at a time, whereas the upgraded system supports operation with multiple harmonics.

2.2 Operational RF program

Figure 2.2 shows the voltage program along a typical 252.7 MeV proton cycle [36][40].

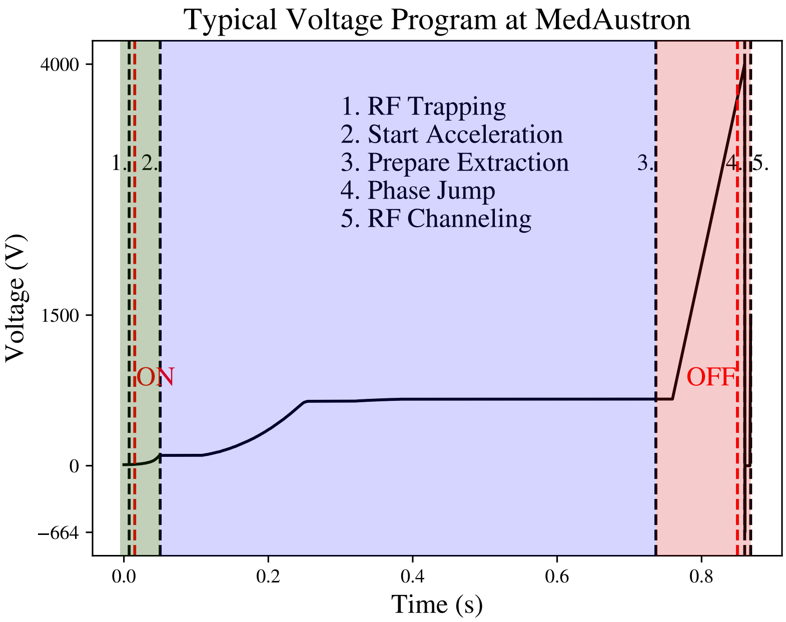

Figure 2.2: RF voltage program of a typical 252.7 MeV proton cycle. The red lines show the activation and deactivation of radial and phase loop. The loops are turned off before the phase jump. Green region: injection and capture; blue: acceleration, red: flat top (FT) and extraction preparation.

The beam is injected into the synchrotron with 7 MeV and a momentum spread of $\delta_{\mathrm{rms}} = 7 \times 10^{-4}$. The coasting beam is subsequently captured by a constant RF frequency and an increasing RF voltage, see 1. in Fig. 2.2. A few milliseconds after the initial capture the phase and radial loop are turned on to regulate the beam. During commissioning the fixed capture frequency capture was optimised via empty bucket scanning (EBS) [36]. The beam is kept at flat bottom (FB) after the capture and before the acceleration with constant voltage and B-field.

The RF voltage program, see 2. point in Fig. 2.2, during capture and the beginning of the ramp was optimised empirically during beam commissioning by minimising beam losses. The relevant losses are longitudinal and transverse losses, which have to be balanced. The longitudinal losses originate in the shrinking bucket as the synchronous phase changes. To minimise longitudinal losses the bucket area should be kept constant, thus the voltage has to be increased. A higher voltage in turn means a higher momentum spread, which leads to an increase in transverse beam size due to dispersion. Figure 2.3a shows the beginning of the acceleration process in a BLonD simulation, which only considers longitudinal but neglects transverse losses. Some particles are lost due to the separatrix closing. The beam is accelerated with constant energy kicks after finding a stable working point (Fig. 2.3b).

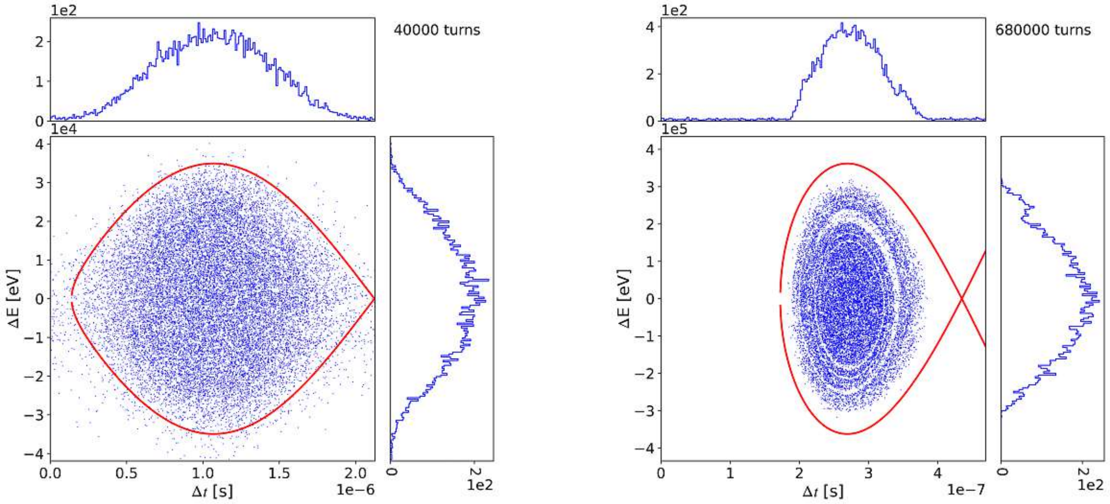

a)

b)

Figure 2.3: BLonD simulation: a) Beginning and b) middle of acceleration.

After reaching the desired energy the synchronous phase is set back to $\Phi_s = 0$ at flat top (FT). The slow extraction implemented at MedAustron requires a large momentum spread. Therefore a phase jump of 180° is applied by switching the phase of the RF voltage within 10 µs, seen in Fig. 2.2 at point 4. The synchronous phase is set to the UFP, the beam is "on" the separatrix. From there the particles follow the respective Hamiltonian equipotential lines, as illustrated in Fig. 2.4. The momentum spread is increased to $\delta \approx 1 \times 10^{-3}$.

It was noted during beam commissioning that the phase jump alone did not meet the requirements for higher proton energies. Consequently, for these energies, the voltage is further ramped at FT to obtain an additional momentum spread increase prior to the phase jump. For a 252.7 MeV proton beam, for example, the voltage is ramped from

663.5 to 4000 V, causing an increase in momentum spread from $\delta = 3.6 \times 10^{-4}$ up to $\delta = 5.9 \times 10^{-4}$.

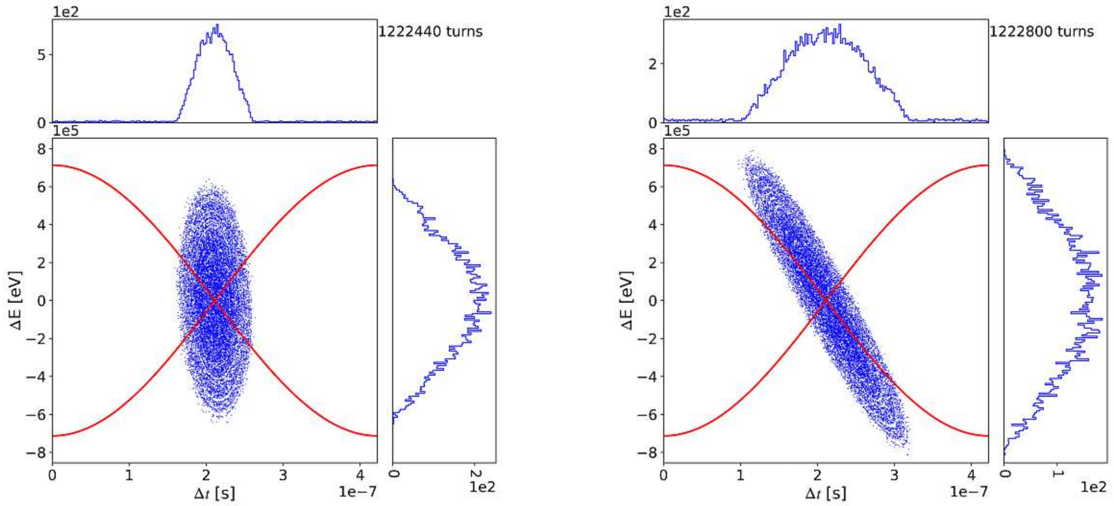

a) b)

Figure 2.4: BLonD simulations: a) Phase jump of 180° and b) momentum spread blow-up along the separatrix.

After the expansion at the UFP the RF voltage is turned off, allowing the beam to unbunch. This beam is ready for extraction. It waits at a stable working point to either be moved into the resonance or the resonance being moved to it during the slow extraction, which is why it is also called the *waiting beam.* At Medaustron the beam is moved into the resonance via betatron core acceleration.

The extracted beam is called the *spill.* For medical beams the spill intensity has to be very stable. To mitigate intensity ripples, for example arising from magnet power supply ripples, empty bucket channeling is implemented, which is described in more detail in [41][42]. Empty bucket *RF channeling* [41] uses an empty bucket created at the resonance energy with a bucket height a tleast twice a large as the of energy spread of band of unstable particles (see [35] page 130). The particles are accelerated by the betatron core and move along the equipotential lines of the bucket. In the longitudinal phase space the particles follow the equipotential lines created by the RF bucket, without entering it. The presence of the bucket provides an additional front-end acceleration that channels the particles towards the resonance [42].

CHAPTER 3

Longitudinal Tomography Set-Up at MedAustron

This chapter outlines the measurement set-up and methods required for implementing longitudinal tomography at MedAustron and compares the tomographic reconstruction with other measurements of the momentum spread.

3.1 Acquisition of Beam Profiles

In the synchrotron at MedAustron shoebox pick-ups (PUs) are used for transverse position measurements, thus also called beam position monitors. The raw signal acquired by each of the horizontal and vertical PU plates is the turn-by-turn measurement of the longitudinal bunch profile. This signal is used for the longitudinal tomography, described further in [5]. The processing of the data for longitudinal tomography is schematically shown in Fig. 3.1. Each longitudinal profile acquisition is a projection of the phase space distribution onto the time-axis and comparable to a different angle in a conventional computer assisted tomography (CT) scan due to the particles' synchrotron motion. By arranging many profiles over time a waterfall diagram is constructed. This waterfall diagram combined with machine and beam parameters, required for the tracking of the particles, are the input needed for the tomographic reconstruction.

3.1.1 Beam Position Monitors

The raw signal acquired by the PU is the voltage induced in each PU plate as the bunch passes, which is described in further detail in [43]. The charged particles induce image charges in the vacuum chamber walls. The wall/image current I_{im} is inferred from the

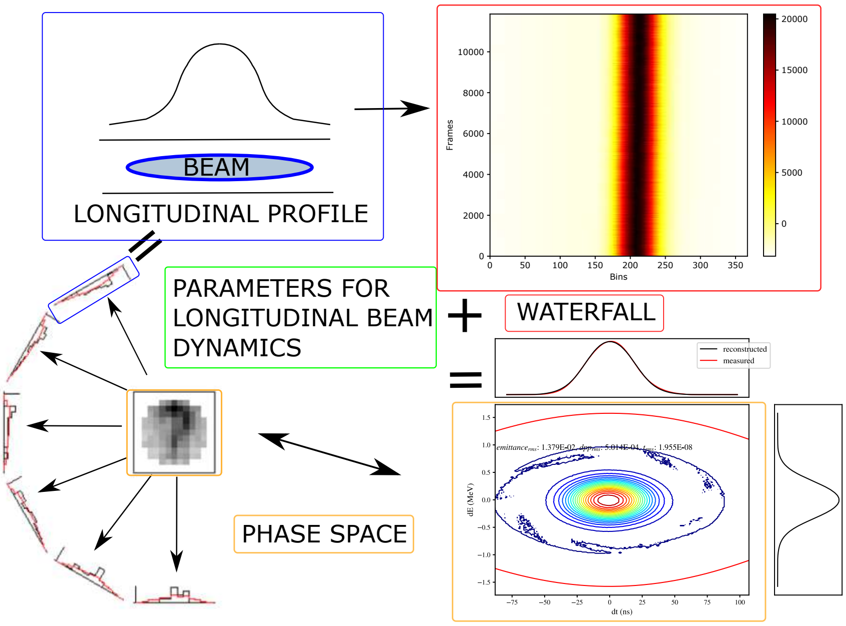

Figure 3.1: Schematic of longitudinal tomography. The upper left picture shows a longitudinal profile acquired with a PU. The sequentially arrangement of many profiles over time is called waterfall diagram (upper right). Each profile can be interpreted as a different angle in a conventional CT scan (bottom left) for the longitudinal phase space (bottom right). By using parameters describing the longitudinal beam dynamics of the reconstructed system and the waterfall diagram the phase space can be reconstructed. Bottom left picture taken from [5].

measurement schematic Fig. 3.2 as

$$I_{\mathrm{im}} = \frac{A}{\pi\, 2a} \frac{l}{\beta c} i\omega I_{\mathrm{beam}}(\omega), \tag{3.1}$$

where l is a length in the longitudinal direction, A the area of the monitor plate, $2a$ the distance between the monitor plates and ω and β the revolution frequency and the relativistic factor of the beam respectively. The beam current $I_{\mathrm{beam}}(\omega)$ is

$$I_{\mathrm{beam}}(\omega) = i\frac{\omega\beta c}{l} \frac{dQ_{\mathrm{beam}}(t)}{dt}, \tag{3.2}$$

originating from charged ions in the bunch dQ_{beam}. The induced voltage U_{im}

$$U_{\mathrm{im}} = Z_{\mathrm{t}} I_{\mathrm{beam}} = \frac{R}{R + i\omega RC} I_{\mathrm{im}} \tag{3.3}$$

is measured across the resistor R and relates to I_{beam} through the transfer impedance Z_{t}. The equivalent circuit corresponds to a high pass filter with a cut-off frequency of $\omega_{\mathrm{cut}} = \frac{1}{RC}$, defined by the resistor R and the capacity C. For $\omega > \omega_{\mathrm{cut}}$ an PU signal with no phase shift is acquired. The voltage signal is proportional to the bunched beam signal. Signals with frequencies below the cutoff frequency are attenuated and their phase is shifted. The PU at MedAustron have high resistance and the capacity is $C \approx 10^{-12}\,\mathrm{F}$.

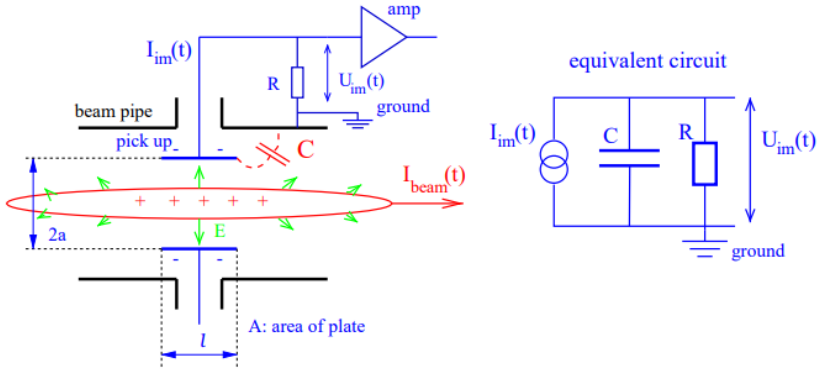

Figure 3.2: Schematic of a pick-up electrode and its equivalent circuit. The image current I_{im} can be calculated using the area of the monitor plate A, the distance of the monitor plates $2a$, the revolution frequency and the relativistic factor of the beam ω and β and the beam current I_{beam}. The induced voltage U_{im} is measured across the resistor R, which together with the capacity C allows a comparison of the pick-up electrode to an equivalent circuit. Picture taken from [43].

3.1.2 Acquisition Systems

To process the longitudinal profiles two acquisition systems are available at MedAustron. The single acquisition distribution system (SADS) has been in use since the first commissioning. As components of the low-level radio frequency (LLRF) system reach their end-of-life and new techniques, such as multi-energy extraction emerge, a new synchrotron LLRF system based on a micro-telecommunication computing architecture (µTCA)-crate [37] is being developed.

The processing chain at MedAustron from the PU to the two acquisition systems is shown in Fig. 3.3 [40]. First the signals are amplified in the head amplifier modules, which are located in the synchrotron hall close to the PUs and part of the front-end electronics. This signal is then further processed in the back-end electronics, more specifically the distribution amplifier, which offers three outputs. The NORM output allows the connection of the PU signals from the head amplifier to the Normalizer module inputs with short LEMO® cables. The SCOPE output connects to the SADS. The µTCA-crate connects to the low-pass filtered ADC output.

Single Acquisition Distribution System

The SADS [40], described in more detail in the Appendix, comprises three oscilloscopes, which are used for acquiring, processing and observing of analogue signals and are connected to the main timing system and the signal routing control. This offers a selection from 144 analogue signals with 50 MHz and 8 analogue signals with 500 MHz

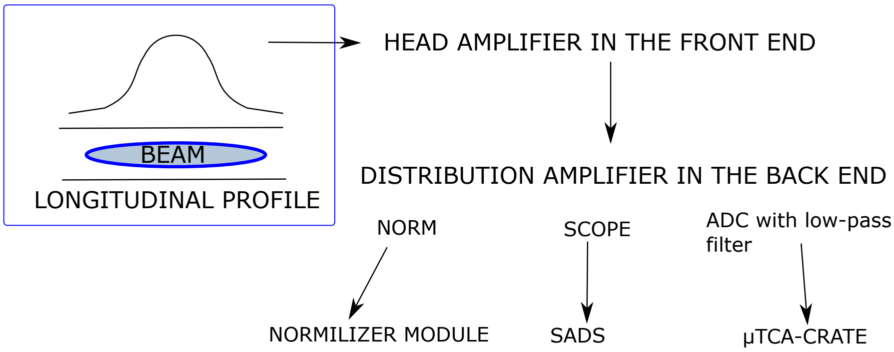

Figure 3.3: Schematic of processing chain from PU signal to SADS and µTCA-crate.

frequency range. The oscilloscopes used are MSO 5054B from TEKTRONIX with a band width of 500 MHz and a sampling rate of up to 5 GS/s. The internal data storage can hold up to 5×10^6 samples and should not be exceeded.

Micro Telecommunication Computing Architecture based Set-up

The µTCA-based system, described further in [37] and the Appendix, will be used for beam measurements required for the new LLRF system for the RF system in the injector and the synchrotron at MedAustron. The µTCA-crate has the option to generate an internal reference clock or to synchronize to an external clock. A valid external reference clock could be provided by MedAustron's timing system. As this reference clock is derived from the GPS time, it allows higher accuracy and a better compatibility to the MedAustron infrastructure. The µTCA-crate is capable of sampling PU (or other) data at rates up to 1 GS/s and a frequency range of 400 kHz to 500 MHz. Up to ∼60 ms of raw ADC data at the highest sampling rate can be digitalised and stored. Data can be preprocessed and demodulated for beam phase and position measurements, which are used in the LLRF system.

3.1.3 Data Processing

The pre-processing of the data is the most computationally extensive part of a full tomographic reconstruction at MedAustron. The PU data was obtained as stream of values. For the tomography the relative position of the profiles to each other is of great importance, so the correct 'slicing' of the data was crucial. The first attempt was to rely this pre-processing step on fast Fourier-transformation (FFT). However, estimating the revolution frequency with the precision needed for this pre-processing step from FFT requires a periodic signal over several milliseconds, which is not applicable, as the number of acquired data points exceeds the internal storage of the SADS, when acquiring with a sampling rate of 1 GS/s, and the LLRF loops change the frequency during normal operation. If the signal is sliced based on an imprecise frequency estimate, the beam erroneously appears to feature a turn-by-tun phase slip. In Fig. 3.4 the waterfall diagrams

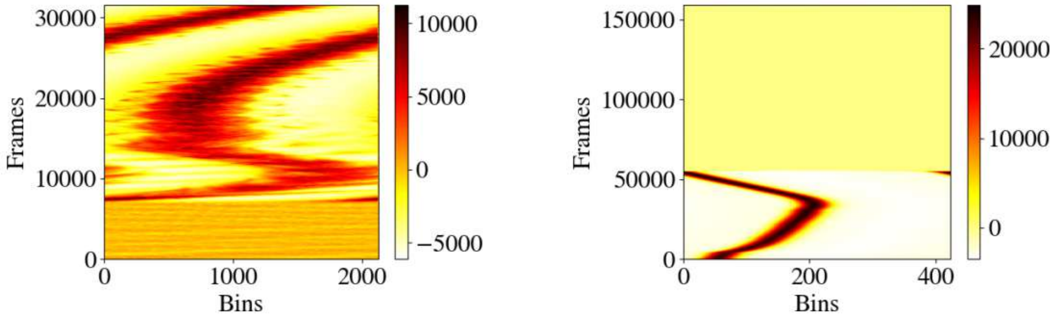

a) b)

Figure 3.4: Waterfall diagram of an µTCA-crate measurement at a) FB and b) FT of a proton beam arranged with FFT. In a) the capture process of a coasting beam from frame 0 to ≈ 8000 frames is shown. At ≈ 13000 frames the beam stabilises and the acceleration begins. In b) the accumulation of a slight frequency error contorts the beam phase as shown in the waterfall diagram. After ≈ 52000 frames the phase jump and the debunching of the beam, described in Section 2.2, can be observed.

of µTCA-crate data acquired at FB and FT of a 252.7 MeV proton beam, arranged via FFT, are shown. The waterfall diagram at FB depicts the capture and the start of the acceleration process. The coasting beam is captured in an increasing RF bucket and stabilised with the LLRF loops, which were discussed in Section 2.1.2. The rising frequency of the beam, as it is accelerated, makes an accurate depiction of the longitudinal profiles with FFT very difficult. Even a stationary beam, such as the proton beam at FT, shown in Fig. 3.4b, accumulates a phase error, if the frequency resolution of the FFT is not precise enough.

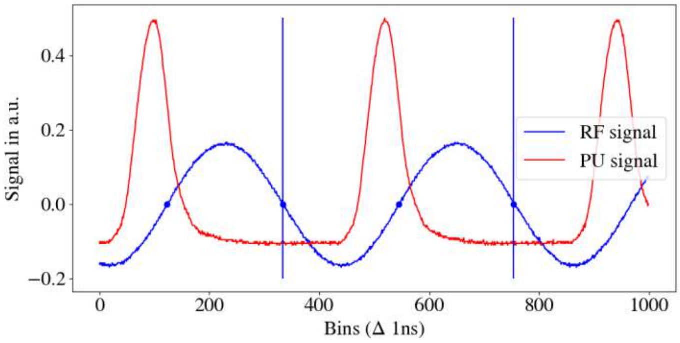

Figure 3.5: The raw PU signal's periodicity is determined with the recorded RF signal by finding the zero-crossings of the RF signal and selecting every second zero-crossing as the start of a new profile.

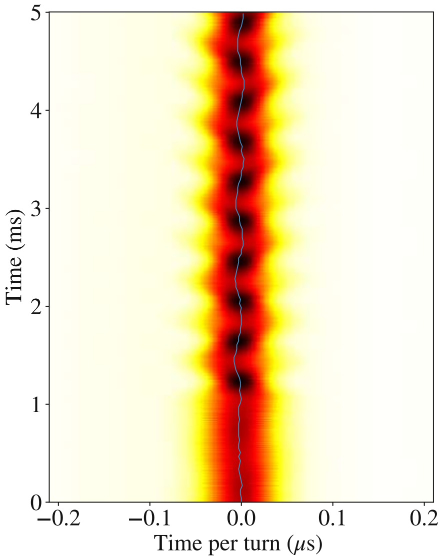

Figure 3.6: The profiles are then arranged into a waterfall diagram, shown here, with the symmetry point in bright blue, see Eq. 3.4. In this measurement quadrupolar-mode oscillations were introduced 1 ms after the beginning of the acquisition, see Sections 4.1.3 and 4.4.2 for further details.

A remedy was found by measuring the RF voltage signal and its periodicity with the SADS, simultaneously to the PU measurements. The RF signal has a clearly defined periodicity. The beam will always be confined within the period of the acquired RF signal $\Phi \in [-\pi, \pi)$, see Fig. 3.5. Thus the RF period was used to cut the data stream into separate beam profiles, which were sequentially arranged to form a waterfall diagram, see Fig. 3.6. Since the RF signal and the PU-signal are measured at different locations in the ring, a phase shift between beam and RF signal is observed. After determining the revolution frequency, the symmetry point [44] for each turn is calculated by

$$\Delta = \left| \sum_{\Phi_1-\pi}^{\Phi_1} f(\Phi) - \sum_{\Phi_1}^{\Phi_1+\pi} f(\Phi) \right| \tag{3.4}$$

which finds the phase Φ_1, which minimises the Riemann sum of the left hand and right hand side of the PU-signal. This calculation is useful for estimating the bunch centroid's phase.

3.2 Tomographic Reconstruction

The longitudinal tomography requires the signal obtained from the PU formatted turn-by-turn. The tomography code [10][5][11] provides a baseline correction with the first 5%

of the reference profile and normalises the turn-by-turn signals. In the documentation of the tomography the raw, but formatted data is called *frames* and the baseline corrected and normalised signals are referred to as *profiles*. The flow chart for the tomography reconstruction are briefly summarised here, for more details of the implementation in the code see Section 1.3.2:

- First the PU-signal and RF voltage signal are measured with a fitting sampling rate for at least half a synchrotron periods.
- The pre-processing of the acquired data includes the arranging into turn-by-turn signals and the calculation of the centroid bunch's phase.
- An input file, formatted as shown in the Appendix, has to be created with the necessary parameters, described in the next section, and the raw but arranged profiles.
- The tomography algorithm first creates a phase space, which is defined by the input parameters, populates it with particles and tracks them over all turns provided by the measurement data.
- Then the baseline corrected and normalised profiles from the measurement are compared to the reconstructed profiles and the weights of each particle are adjusted to minimise the difference. The resulting phase space distribution can be used to calculate the relative momentum spread, bunch length and longitudinal emittance. The output is visualised in a graph similar to Fig. 3.7.

3.2.1 Input Parameters

As mentioned before the tracking of the particles is based on user-defined input regarding beam and machine parameters. The input parameters for the tracking of particles and tomographic reconstruction are listed here, further information on parameters and the longitudinal tomography can be found in [11]:

- **Number of profiles**: The number of profiles in the measurement data should at least cover one half of a synchrotron period. Further, it is stated as a practical rule of thumb [5] to chose the number of profiles similar the number of bins per profile.
- **Number of bins per profile**: This value is determined by the time resolution of the measurement and the user's decisions how much no-beam data to include.
- **Width in seconds**: The time resolution of the measurement.
- **Maximal energy**: This value defined the energy range $\pm E_{\max}$ of the longitudinal phase space, which is considered during reconstruction. It can either be given by the user or ascertained by the algorithm. The phase space is divided in discrete

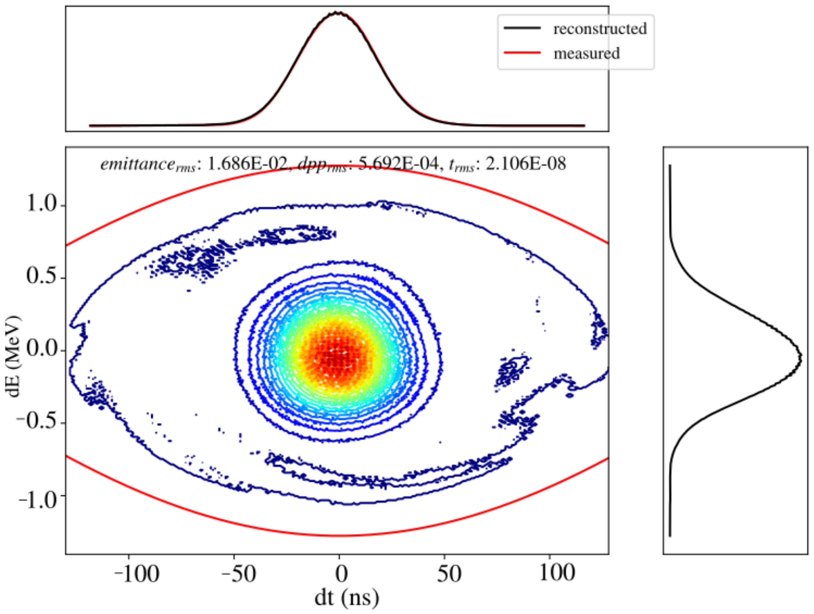

Figure 3.7: The reconstructed phase with the output parameters longitudinal emittance, root-mean-square of the relative momentum distribution and the root-mean-square of the relative time distribution.

intervals of time and energy. The energy bin width is given by $2E_{\mathrm{max}}$ divided by the number of bins per profile. With prior knowledge of the maximal deviation from the synchronous particles' can be estimated and the binning refined.

- **Rebinning factor**: By rebinning the profiles the number of data points used for the reconstruction is reduced, which reduces the required computational resources.

- **Time in bins of the synchronous phase**: This value can either be ascertained by the algorithm or defined by the user, as might be advantageous in some cases. It describes the relative position of the synchronous particle within the reference beam profile. Currently the best estimation is the calculated symmetry point, see Eq. 3.4. This allows the determination of the time bin of the synchronous particle within $\approx \pm 5$ bins. For a 252.7 MeV proton cycle at FT recorded with 1 GS/s defining the synchronous phase using this procedure results in a phase uncertainty of approximately 4.24°.

- **Number of turns between profiles**: The number of profiles should be similar to the number of bins per profile but span at least half of one synchrotron period. Thus not all profiles are selected for tomographic reconstruction but for example every 10th turn over one synchrotron period. By giving this value the tracked particles are projected every 10th profile and the projected profile is compared to the measured profile.

- **Iterations**: 20-30 iterations of projection and back-projection, as described in Section 1.3.2, have been found to be sufficient.
- **Square root of test particles per cell**: This parameter is used for defining the initial longitudinal phase space distribution of the test particles prior to tracking. The user can either choose a custom distribution or the distribution is created by uniformly populating each phase space cell. This input parameter is used for defining the number of test particles in the second case. 2-4 are acceptable values for our application, depending on the computational effort. For example the phase space cell $t \in (t_s, t_s + \Delta t]$ and $E \in (E_s, E_s + \Delta E]$ with t_s and E_s the synchronous particle's coordinates in phase space and Δt and ΔE the bin width in time and energy is populated with 2^2 particles with the following coordinates:
    - Particle 1: $(t_s + \frac{\Delta t}{2}, E_s + \frac{\Delta E}{2})$
    - Particle 2: $(t_s + \Delta t, E_s + \frac{\Delta E}{2})$
    - Particle 3: $(t_s + \frac{\Delta t}{2}, E_s + \Delta E)$
    - Particle 4: $(t_s + \Delta t, E_s + \Delta E)$

  These particles are then tracked along the iso-Hamiltonian according to the other input parameters.
- **Flag for population**: The user can choose to either distribute test particles within the separatrix (= 0), which is calculated based on the RF input parameters, or all cells of the longitudinal phase space (= 1).
- **Peak RF voltage of principal RF system and its time derivative**: This value is of particular importance as it is usually the least well defined. It is used in the determination of the reconstruction area (separatrix) and crucial for accurate tracking.
- **Harmonic number**: The harmonic number of the principal RF system is currently $h = 1$ at MedAustron, but the algorithm is capable of the reconstruction with higher harmonics.
- **Dipole *B*-field and its derivative**: In the tomography algorithm this value is used to calculate the energy and revolution frequency of the beam, knowing the machine circumference. At MedAustron, the frequency and the energy at FT are known with high accuracy, compared to the B-field. Consequently, as the final parameters of interest are the frequency and the energy, the B-field, which is provided as input parameter for the tomography is considered as a working parameter and is computed so that it returns the actual measured frequency. It is worth noting, that the synchrotron at MedAustron commonly operates off-momentum with momentum offsets of $\frac{\Delta p}{p}$=$\mathcal{O}(10^{-3})$. As the computation in the tomography code does not consider any radial loop offsets, the B-field has to be

regarded as a virtual, effective B-field to provide the respective revolution frequency for a specific energy.

- **Machine parameters**: The machine radius, the bending radius and the transition energy fall beneath this category.
- **Beam parameters**: The rest energy and the charge state of the particles.
- **Space charge parameters**: If desired the tomography can perform its tracking including direct space charge effects. As their contribution can be neglected at MedAustron due to low intensity, this option was disabled for now.
- **Tomoscope parameters**: These parameters allow to save the output of the reconstruction at different time frames. The created phase space images can be spliced together in an animation, allowing for great visualisation of the phase space. An example: In measurement of 4000 turns every 10th turn was selected as input for the tomography. If the tomoscope option is enabled the reconstructed phase space distribution can be visualised every x-th turn. With this option an animation of the evolution in phase space is possible.

An example file is shown in the Appendix. The tomography code provided by CERN [10][5] has been installed on the Linux server at MedAustron. The server provides 8 cores per CPU. A reconstruction based on the following input parameters takes about 90 seconds on the Linux server at MedAustron, with memory usage of 725.52 MB and 78 % CPU usage:

- 400 raw profiles with 10 turns between profiles between each profile are used as input data.
- The profiles have been acquired with a sampling rate of 1 GS/s and thus a bin width of 1 ns.
- Restricting the signal to the region of interest around the bunch centroid, only 170 of the 422 bins per profile were used.
- The test particle distribution is initialised with 3^2 particles per phase space cell.
- The longitudinal tomography is run over 30 iterations.
- The tomoscope option, which provides the phase space distribution every x-th turn, is enabled to visualise the phase space every 10th profile.

3.2.2 Further Notes on the Implementation at MedAustron

Section 4.3 will discuss uncertainties concerning the RF voltage at MedAustron. As a result of these findings, the input voltage for the tomographic reconstruction is specified as

$$V_{\text{rec}} = 1.42 \times V_{\text{nom}}, \tag{3.5}$$

where V_{nom} is the voltage as measured by the RF system.

Further, all measurements presented in this thesis are acquired with the horizontal pick-up MR-04-000-PUH. Selected tests with other PUs where performed during the preparation for these studies, which did not result in any significant difference between the PUs. All measurements further used the sum of the plates signal (Σ-signal) of the PU plates, which is justified in Section 4.2.

3.3 Alternative Methods for Measuring the Momentum Spread

An important output of the longitudinal phase space reconstruction described in tomography set-up is the momentum spread and its evolution over the measured time intervall. In this section alternative measurement methods for the momentum spread, the Schottky monitor and empty bucket scanning (EBS), are presented.

3.3.1 Schottky Monitor

Schottky monitors in synchrotrons measure the signal caused by fluctuations of charge carriers as they repeatedly pass the monitor. The current of coasting beams, under the assumption of randomly distributed particles, which are characterized by their phase θ_n and have the same revolution frequency f_0, can be described as

$$I(t) = ef_0 \sum_{n=1}^{N} \cos(\theta_n) + 2ef_0 \sum_{n=1}^{N} \sum_{h=1}^{\infty} \cos(2\pi f_0 ht + h\theta_n) \tag{3.6}$$

as explained in Peter Forck's lecture on "Beam Measurements using Schottky Signal Analysis" [45]. The integral power of each harmonic $P_h = Z_t \langle I^2 \rangle_h$ is constant. While the coasting beam's spectrum displays only incoherent single particles contributions, the spectra of bunched beams are expressed as

$$I(t) = e\omega_0 \sum_{n=1}^{N} \delta_{2\pi}(\omega_0 t + \theta(\Omega_n, \Phi_n + \Omega_n t)) \tag{3.7}$$

with $\delta_{2\pi}$ being the periodic Delta-function, θ being the azimuthal angle between nth particle and the bunch centre depending on the synchrotron frequency Ω_n and the initial phase Φ_n, as described in detail in [46]. The measured signal is processed by a spectrum analyser, which evaluates amongst other parameters, the revolution frequency distribution. With the relation Eq. 1.21 the relative momentum spread can be obtained. These measurements can be quite slow as the spectrum analysers sweep through the frequency span Δf_s slow enough to provide the required frequency resolution Δf_r. While the tomography measurements takes $\approx 2 - 4\,\mathrm{ms}$ acquiring data within one synchrotron period, the Schottky frequency analyser measurement takes up to 100 ms.

3.3.2 Empty Bucket Scan

Another method of measuring the momentum spread is the EBS. This method has been used during the commissioning at MedAustron [36] and is based on moving a small bucket of 5 to 10 V slowly, i.e. with a ramp rate of $df/dt \approx 2\,\mathrm{kHz/s}$, through the relevant frequency range. During the ramp, the part of the beam matching the bucket frequency, is displaced and the longitudinal PU-signal changes. Recording the signal as I and Q value by demodulation allows the calculation of the momentum spread. This method is not applicable for normal operation. Firstly, it requires a specifically modified cycle as the EBS takes up to seconds. Secondly, it is an invasive measurement technique, which makes the beam unusable for further usage.

3.3.3 Comparison of Measurement Methods

In Table 3.1 the three mentioned measurement methods, Schottky spectrum analyser, EBS and tomographic reconstruction, are compared. It is worth highlighting, that even if measuring the momentum spread of a bunched beam with the Schottky monitor, the long acquisition time averages any information regarding the evolution of the momentum spread. The tomography offers a non-invasive method to visualise the longitudinal phase-space distribution and its evolution.

Technique	Required time	Beam	Non-invasive	Phase-space
Tomography	2-4 ms	bunched	✓	✓
Schottky	100 ms	both*	✓	
EBS	1-2 s	coasting / unbunched		

Table 3.1: Comparison of different momentum spread measurement methods concerning the required acquisition time in order of magnitude, the compatibility with coasting or bunched beam, whether the beam is disturbed or not and whether the results yield transient behaviour in phase space or an averaged value of the momentum spread. *While the Schottky frequency analyser works with bunched and coasting beams, the method has proven to be more reliable for unbunched beams at MedAustron [47].

CHAPTER 4

Benchmarking Measurements and Simulations

This chapter presents measurement results to benchmark the newly implemented longitudinal tomography set-up. An overview of the presented test cases is provided in Section 4.1. As preparatory study in Section 4.2, the profiles of the two available acquisition systems are compared and evaluated regarding their suitability for tomographic reconstruction. Section 4.3 describes a suspected radio frequency (RF) voltage error, which was observed during the presented studies, and discusses the consequent beam-based RF voltage calibration and its implications for the implementation of longitudinal tomography at MedAustron. In Section 4.4 the tomography results for various test cases are presented, including beam capture after injection, matched and mismatched beams at flat top (FT). The reconstructed phase space distributions and common longitudinal beam parameters, i.e.

- longitudinal emittance $\epsilon_{\mathrm{L}} = \pi\sigma_E\sigma_t$
- root-mean-square of the relative momentum spread δ_{rms}
- bunch length, defined as $l = 4\sigma_t$ in this thesis,

are shown. The overall performance of the tomography set-up at MedAustron is summarised and discussed in Section 4.5.

4.1 Settings for Measured and Simulated Test Cases

For all measurements, the longitudinal signal was obtained by two acquisition systems: SADS and µTCA-crate, which have been described in detail in Section 3.1.1. If not

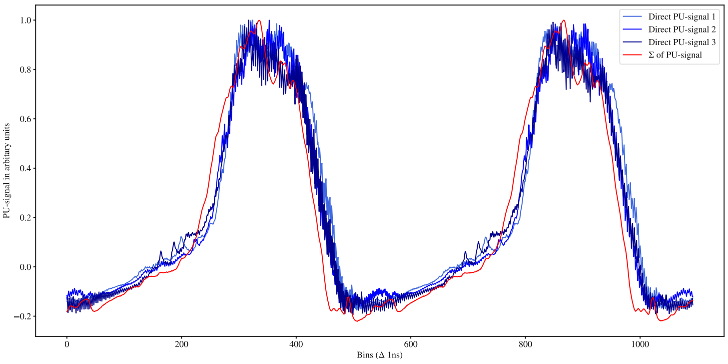

Figure 4.1: Comparison of normalised sum Σ-signal and direct plate signals acquired from the same PU (MR-08-000-PUH).

otherwise specified the Σ-signal of the horizontal pick-up (PU) MR-04-000-PUH with a sampling rate of 1 Gs/s was used. Several test were devised to benchmark the performance of the newly implemented tomoscope, particularly aiming at the following:

- Optimise the data acquisition and the pre-processing procedure.
- Evaluate the tomographic reconstruction of operational, matched beams of different ion species at different energies and intensities.
- Benchmark the tomographic reconstruction using the developed set-up by reconstructing non-nominal, mismatched longitudinal distributions.

4.1.1 Preparatory Measurements

First preparatory measurements for developing the data acquisition procedure were performed. One aim of these measurements was to compare the raw signal of a single plate, referred to as *direct plate signal*, with the sum signal of the two PU plates. The second objective was to select a suitable input impedance of the SADS. Figure 4.1 illustrates both, direct plate and sum signals, measured with the MR-08-000-PUH. The measurements are taken at flat bottom (FB) of a proton beam, directly after the capture. It should be noted, that Fig. 4.1, aims at a purely qualitative comparison, as the individual signals are acquired from different cycles. The overall form of the Σ-signal is reflected in the direct plate signals. However the Σ-signal is less noisy and was thus chosen for the tomographic reconstruction.

The termination of the µTCA is 50 Ω, whereas the SADS allows the user to select an input impedance of either 50 Ω or 1 MΩ. As Fig. 4.2 depicts, the 50 Ω termination provides a more symmetric and clearer signal and was thus chosen in the following measurements. This can be explained by the 50 Ω termination suppressing internal

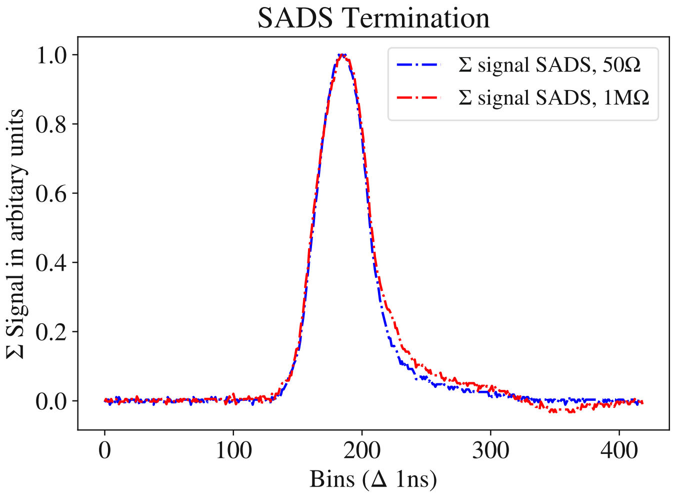

Figure 4.2: Comparison of the acquired signal with the SADS when measuring with 50 Ω and 1 MΩ termination. The illustrated data belongs to measurements taken at FT of a 252.7 MeV proton cycle and are baseline corrected and normalised.

reflections [48]. The signals will be further compared in Section 4.2 for different energies and intensities.

4.1.2 Settings for Matched Beams

The first measurement series, labelled P1-P5, aims at reconstructing the phase space of operational proton beams with nominal RF settings, but different intensities. For each entry shown in Table 4.1 three measurements were performed. The acquisition starts with a trigger from the main timing systems, which was either StartEVS, i.e. triggers at FT 23 ms before the phase jump (compare to Fig. 2.2), or StartAcceleration (StartAcc), which triggers at FB, after the capture and before acceleration.

Label	Kinetic Energy [MeV]	Trigger	Percent of design intensity	Results in Sec.
P1	7	FB	100	Section 4.4.1
P2	7	FB	50	Section 4.4.1
P3	62.4	FT	100	Section 4.4.1
P4	62.4	FT	50	Section 4.4.1
P5	252.7	FT	100	Section 4.4.1

Table 4.1: Parameter overview of the benchmarking experiments for reconstructing the longitudinal phase space distribution for matched proton beams.

A similar test series with nominal RF settings was conducted with carbon beams. Table 4.2 shows the specifics of the applied cycle. For each cycle three measurements were done.

Label	Kinetic Energy [MeV/u]	Trigger	Percent of design intensity	Results in Sec.
C1	7	FB	100	Section 4.4.1
C2	7	FB	20	Section 4.4.1
C3	120	FT	100	Section 4.4.1
C4	120	FT	20	Section 4.4.1
C5	402.8	FT	100	Section 4.4.1

Table 4.2: Parameter overview of the benchmarking experiments for reconstructing the longitudinal phase space distribution for matched carbon beams.

4.1.3 Settings for Mismatched Beams

In order to test the validity of the reconstruction intentional mismatches were introduced. The test cases included instantaneous jumps of the RF voltage, resulting in a mismatch between bucket shape and the longitudinal phase space distribution (Section 1.1.6), as well as instantaneous phase and energy offsets of the bunch with respect to the synchronous particle. For these measurements the regulation loops were turned off 10 ms before the measurements. These measurements were taken at FT of a 252.7 MeV proton cycle with no voltage ramp to 4000 V, opposed to the normal operations, see Fig. 2.2, and 100% intensity. The parameters for each test case are listed in the Tables 4.3 to 4.5. The results from these measurements can be found in Section 4.4.2.

Settings for Introducing Quadrupolar-Mode Oscillations: The tests concerning the reconstruction of quadrupolar-mode oscillations were performed with a stationary 252.7 MeV proton beam with nominal intensity, as listed in Table 4.3. The instantaneous jump in the RF voltage was applied 1 ms after the trigger event. The newly set voltage (900 or 1500 V) is reached within 30-50 µs, which corresponds to approximately 1/10 of a synchrotron period and is hence non-adiabatic. As the voltage increases, the bucket height increases as well. For instantaneous, which means very fast compared to the synchrotron period, voltage changes the longitudinal distribution no longer matches the bucket and starts to oscillate. During these oscillations the beam's centre of mass' position in the longitudinal phase space does not change. Instead the shape and orientation of the longitudinal distribution in phase space oscillate. The input for BLonD simulations uses to specified voltage jump from 663.5 to 900 or 1500 V. The radial and phase loop were turned off 11 ms before the voltage jump.

Label	Kinetic Energy [MeV/u]	Trigger	Jump to [V]	Jump from V_{nom} [V]
V1	252.7	FT	1500	663.5
V2	252.7	FT	900	663.5

Table 4.3: Parameter overview of the benchmarking experiments for reconstructing the longitudinal phase space distribution during quadrupolar-mode oscillations.

Settings for Introducing Dipolar-Mode Oscillations: In dipolar-mode oscillations, the whole bunch is off-centre and starts to rotate around the synchronous particle. This can be caused by an energy offset, which corresponds to an offset between revolution frequency and RF frequency, or phase offset between the bunch centroid and the synchronous phase. Such a phase offset was introduced at MedAustron by applying a small frequency offset over a limited time, according to the program shown in Fig. 4.3. The frequency program jumps to the specified frequency offset, stays at that offset for 20 µs and then returns to the fixed frequency. The expected phase offset per turn in degrees is calculated with

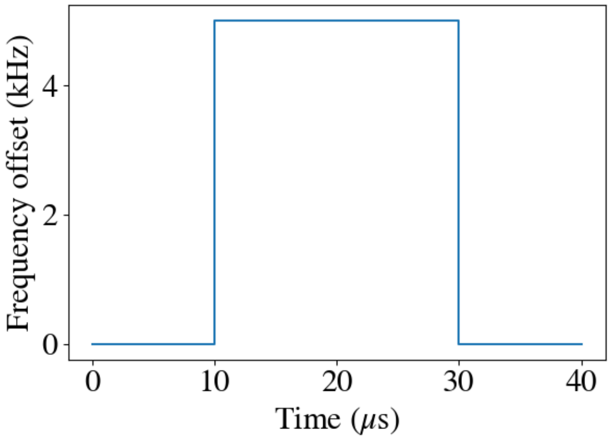

Figure 4.3: Applied short frequency offset to accumulate a phase offset between bunch centroid and synchronous particle, inducing dipolar-mode oscillations.

$$\Delta\Phi = 360^\circ \frac{\Delta f}{f}. \tag{4.1}$$

The resulting phase offset was modeled in BLonD by introducing a phase jump of the expected value at FT, by loading the beam distribution with the expected energy offset. For test case F1, which is matched for 663.5 V and a frequency of 2368143.8 Hz, an energy offset of 143.7 keV was calculated for a phase offset of 36°. Similarly, for the test case F2 an energy offset of 287.5 keV was calculated for a resulting phase offset of 72°. Table 4.4 shows the test series F, which was carried out with a stationary 252.7 MeV proton beam of 100% intensity. The LLRF loops were turned off 11 ms before the induced phase offset.

Label	Kinetic Energy [MeV/u]	Trigger	Frequency Offset [kHz]	Expected Phase Offset
F1	252.7	FT	5	$\approx 36^\circ$
F2	252.7	FT	10	$\approx 72^\circ$

Table 4.4: Parameter overview of the benchmarking experiments for reconstructing the longitudinal phase space distribution during dipolar-mode oscillations.

Another cause for dipolar-mode coherent bunch oscillations in longitudinal phase space is an offset in energy. This was introduced in the MedAustron control system by applying a constant frequency offset at FT. The experiments were performed with a 252.7 MeV proton beam. Compared to the operational cycle, the voltage ramp, which is operationally applied at FT to increase the momentum spread prior to the phase jump, was removed in the test cycle. To avoid losing the beam, it is important to assure that the introduced energy offset is smaller than half the bucket height. The height of the separatrix was calculated according to

$$\delta_{\max} = 2\sqrt{\frac{qV}{2\pi\beta^2 Eh|\eta|}}Y(\Phi_s) \tag{4.2}$$

and used to estimate the frequency offset needed to achieve a 45° phase offset [2]. For 252.7 MeV and the nominal voltage, 663.52 V, a frequency offset of 350 Hz needs to be applied.

The same test, i.e. introducing an energy offset between bunch and synchronous particle, is repeated for a larger RF voltage and hence bucket height. In this case the voltage is adiabatically increased from 663.5 to 900 V before applying a frequency offset of 416 Hz. The parameters of both experiments are listed in Table 4.5. The LLRF loops are turned off 11 ms before the respective changes in the RF frequency. To simulate these measurements in BLonD, the frequency jump was introduced in simulation by introducing an instantaneous path length decrease to mimic the increased driving RF frequency. The matched beam distribution is then loaded into the new ring with an initial, calculated energy offset.

Label	Kinetic Energy [MeV/u]	Trigger	Frequency Offset [Hz]	Nominal Voltage [V]
K1	252.7	FT	350	663.52
K2	252.7	FT	416	900

Table 4.5: Parameter overview of the benchmarking experiments for reconstructing the longitudinal phase space distribution during dipolar-mode oscillations.

4.2 Analysis of Acquired Longitudinal Profiles

In this section the impact of the beam energy and the intensity on the measured PU-signal will be discussed.

Comparison of SADS and µTCA-crate Acquisitions at FB

Figures 4.4 and 4.5 depict the signals obtained from SADS and µTCA-crate, when measuring a 7 MeV proton beam. These measurements were taken at FB, prior to acceleration and related particle losses. Several differences between the SADS and the µTCA-crate acquisition are evident. Firstly, the low-pass filtered µTCA-signal from acquisition chain, see Section 3.1.2, is less noisy than the SADS signal. Another apparent

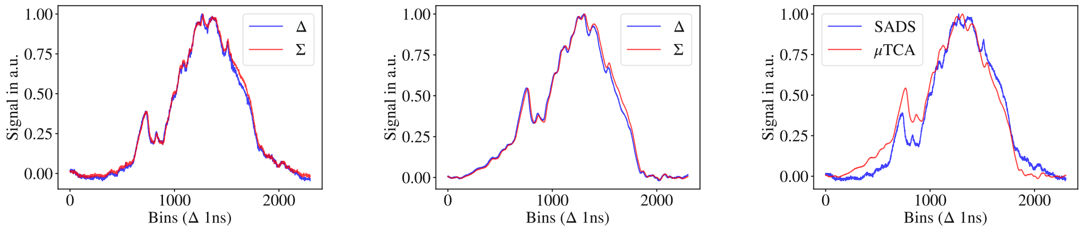

a) SADS b) µTCA c) comparison of Σ-signal

Figure 4.4: Comparison of the longitudinal profile acquired with MR-04-000-PUH (baseline corrected and normalised) acquired after capture of a 7 MeV proton beam. a) Σ- and Δ−signal acquired with the SADS, b) Σ- and Δ−signal acquired with the µTCA-crate and c) comparison of Σ-signal acquired with SADS and µTCA-crate.

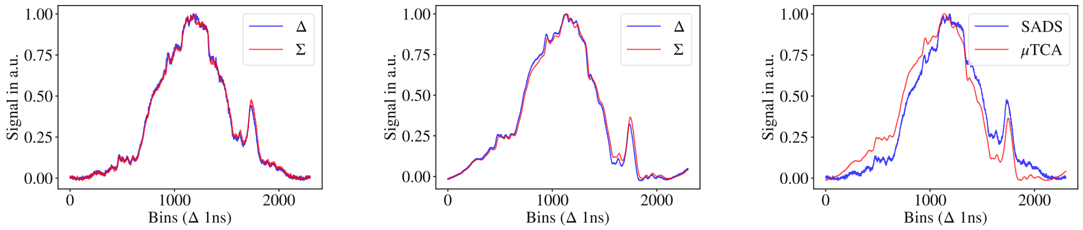

a) SADS b) µTCA c) comparison of Σ-signal

Figure 4.5: Comparison of the longitudinal profile acquired with MR-04-000-PUH (baseline corrected and normalised) acquired after capture of a 7 MeV proton beam. a) Σ- and Δ-signal acquired with the SADS, b) Σ- and Δ-signal acquired with the µTCA-crate and c) comparison of Σ-signal acquired with SADS and µTCA-crate.

difference between the two acquisition systems is the baseline and general shape of the signal. Especially noteworthy that the no-beam-signal is the same before and after the beam in the profile acquired with the SADS, but differs for the µTCA-crate measurement. These differences in signal shape are also evident when regarding the side-peak in Figs. 4.4 and 4.5c. Directly after the capture the beam is still filamenting and unevenly distributed over the phase space. Consequently the profile features peaks, which correspond to particle accumulations which oscillate around the synchronous phase with a phase offset of $\Phi \approx 102°$. The width and the height of the peak does not change drastically within one synchrotron period. The SADS measurements confirms this assumption. The fast rise before, seen in Fig. 4.4c, and decline in µTCA-signal, seen in Fig. 4.5c, after the beam are less reliable for tomography than the proportional peaks of the SADS acquisition. The asymmetrical peak height in the µTCA measurements increases the discrepancy of the reconstruction.

Figures 4.6 and 4.7 show a that s similar characteristic is observed for 7 MeV/u carbon beams at FB.

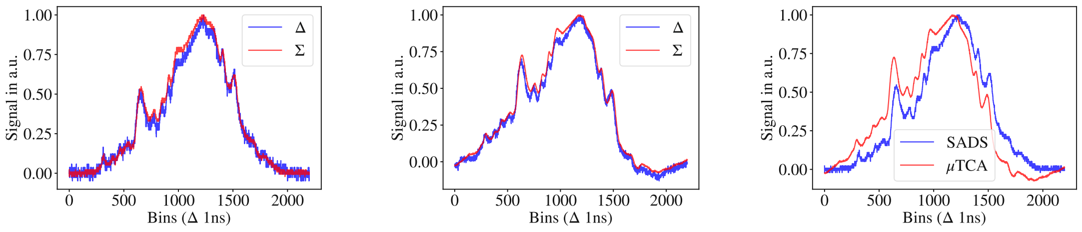

a) SADS b) µTCA c) comparison of Σ-signal

Figure 4.6: Comparison of the longitudinal profile acquired with MR-04-000-PUH (baseline corrected and normalised) acquired after capture of a 7 MeV/u carbon beam. a) Σ- and Δ-signal acquired with the SADS, b) Σ- and Δ-signal acquired with the µTCA-crate and c) comparison of Σ-signal acquired with SADS and µTCA-crate.

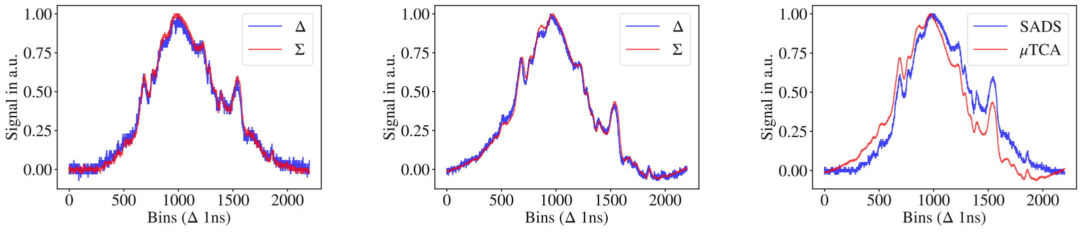

a) SADS b) µTCA c) comparison of Σ-signal

Figure 4.7: Comparison of the longitudinal profile acquired with MR-04-000-PUH (baseline corrected and normalised) acquired after capture of a 7 MeV/u carbon beam. a) Σ- and Δ-signal acquired with the SADS, b) Σ- and Δ-signal acquired with the µTCA-crate and c) comparison of Σ-signal acquired with SADS and µTCA-crate.

Comparison of SADS and µTCA-crate Acquisitions at FT

For measurements at FT of a 62.4 MeV proton beam the µTCA-crate delivers a more symmetrical signal than the SADS acquisition, see Fig. 4.8c. The signal-to-noise ratio of sum Σ- and difference Δ−signal of SADS and µTCA acquisition is comparable. Especially the low-pass filtered µTCA signals in Fig. 4.8b have very similar signal-to-noise ratios. The figure however exhibits a slight phase offset between Σ- and Δ-signal. When comparing the Σ-signal of the two acquisition systems the most noticeable difference is the asymmetry in the SADS signal, referred to as *tail*. When performing a tomographic reconstruction, this tail will cause an increase in the reconstructed momentum spread and emittance, as can be seen in the Section 4.4.

For higher energies the bunch length is shorter and the peak signifying the beam becomes smaller for constant sampling rates. In Fig. 4.8a-b the difference between Δ- and Σ-signal is more notable in both SADS and µTCA-crate acquisition.

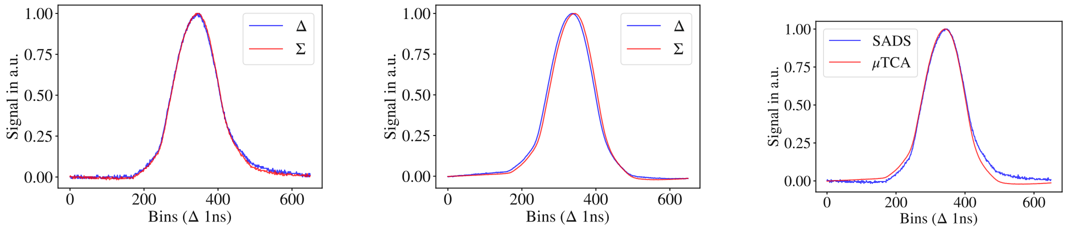

a) SADS b) µTCA c) comparison of Σ-signal

Figure 4.8: Comparison of the longitudinal profile acquired with MR-04-000-PUH (baseline corrected and normalised) acquired at FT of a 62.4 MeV proton cycle with 100% intensity: a) Σ- and Δ-signal acquired with the SADS, b) Σ- and Δ-signal acquired with the µTCA-crate and c) comparison of Σ-signal acquired with SADS and µTCA-crate.

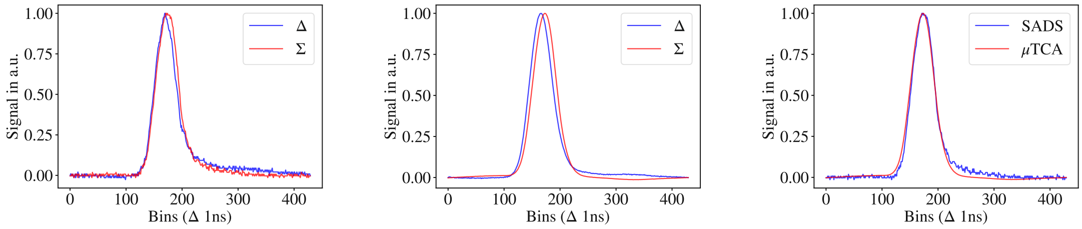

a) SADS b) µTCA c) comparison of Σ-signal

Figure 4.9: Comparison of the longitudinal profile acquired with MR-04-000-PUH (baseline corrected and normalised) acquired at FT of a 252.7 MeV proton cycle with 100% intensity: a) Σ- and Δ-signal acquired with the SADS, b) Σ- and Δ-signal acquired with the µTCA-crate and c) comparison of Σ-signal acquired with SADS and µTCA-crate.

The signals from carbon beam show the same behaviour and will be discussed in the next paragraph in regards to different intensities.

Comparison of SADS and µTCA-crate Acquisitions of Beams with Different Intensities

These tests aimed at qualitatively comparing the acquired longitudinal profiles for beams with different intensities, using a 120 MeV/u carbon beam of nominal intensity (100%) and a carbon beam with reduced intensity (20%). The FT, Fig. 4.10, and FB comparison, Fig. 4.11, show that the longitudinal profile are comparable to full intensity profiles and can be used for the tomographic reconstruction. However, in several turns of the 20% intensity beam signal baseline distortions have been observed. Examples of this

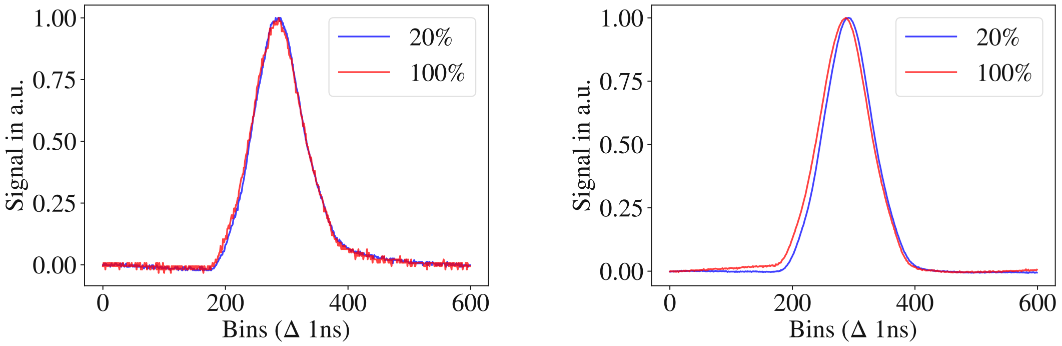

a) SADS

b) µTCA

Figure 4.10: Comparison of the longitudinal profile acquired with MR-04-000-PUH (baseline corrected and normalised) acquired at FT of a 120 MeV/u carbon cycle with 100% intensity and 20% intensity: a) Σ-signals acquired with the SADS and b) Σ-signals acquired with the µTCA-crate.

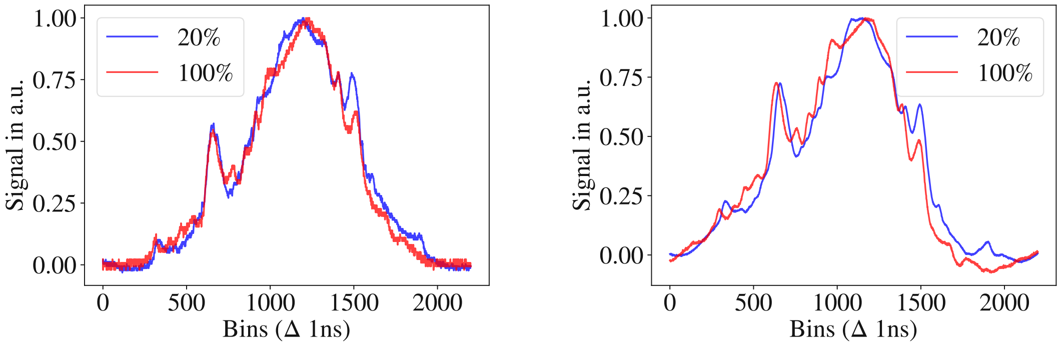

a) SADS

b) µTCA

Figure 4.11: Comparison of the longitudinal profile acquired with MR-04-000-PUH (baseline corrected and normalised) acquired after capture of a carbon beam with 100% intensity and 20% intensity: a) Σ-signals acquired with the SADS and b) Σ-signals acquired with the µTCA-crate.

are shown in Figs. 4.12 and 4.13, where the baseline for two profiles of the same cycle differ. This distortion impairs the quality of the tomographic reconstruction, which is still reasonably good for the test cases presented in this thesis. For low flux beams the tomography set-up as it is now might need to be further improved.

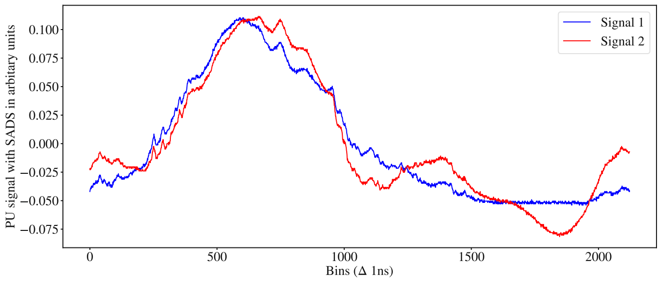

Figure 4.12: PU profile (sum signal) recorded with the SADS after capture of a carbon beam with 20% intensity. Signal 1 and 2 are from the same cycle, with two turns between the signals.

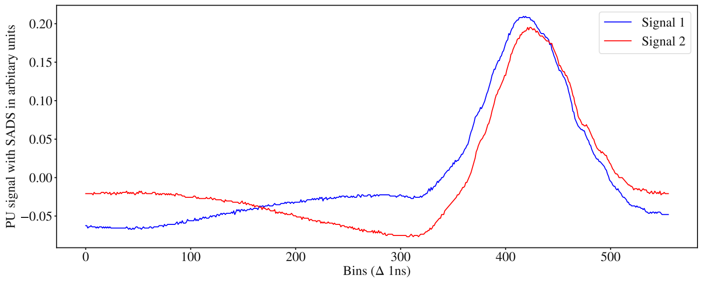

Figure 4.13: PU profile (sum signal) recorded with the SADS at FT of a 120 MeV/u carbon cycle with 20% intensity. Signal 1 and 2 are from the same cycle, with two turns between the signals.

4.3 Radio Frequency Voltage Calibration

Initial tests, particularly when aiming to reconstruct mismatched distributions, showed that the reconstruction did not perform as expected when using the nominally assumed machine and beam parameters as input parameters. The reconstructed profiles and the measurements did not align. However, varying the assumed RF voltage, when defining the input parameters for the tomography, lead to better reconstructions with lower discrepancy between measured and reconstructed profiles [49]. This can be seen in Fig. 4.14, which compares the reconstruction performance under the assumption of different RF voltages for different test cases. The quality of the reconstruction was evaluated via the *discrepancy*, as introduced in Eq. 1.49. The voltage used for reconstruction is given in relation to the operationally assumed voltage $\mathrm{V_{nom}}$. In each discrepancy-voltage plot of proton cycles a minimum can be observed at $\frac{\mathrm{V}}{\mathrm{V_{nom}}} \approx 1.43$.

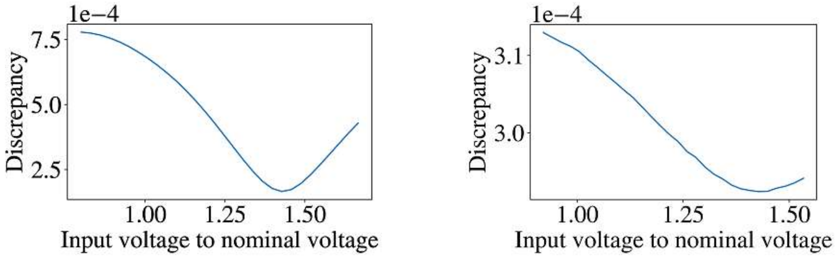

a) V1 reconstruction

b) P4 reconstruction

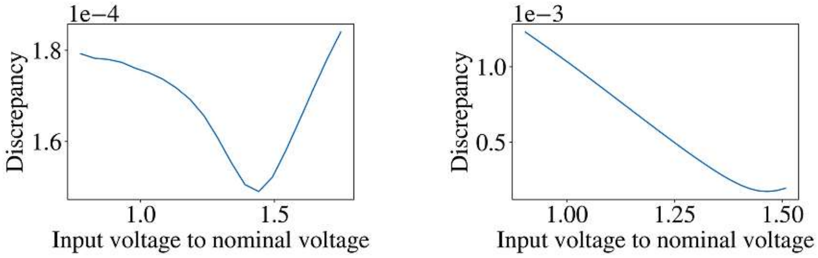

c) P1 reconstruction

d) K1 reconstruction

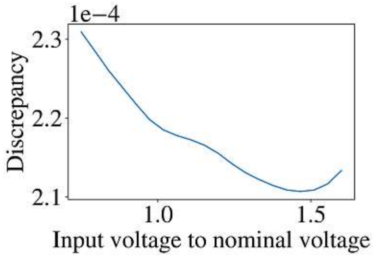

e) C1 reconstruction

Figure 4.14: Reconstruction discrepancy for different input voltages. The input voltage for the tomography is stated in relation to the operationally assumed voltage. The different test cases shown are a) Voltage jump from 663.5 to 1500 V at FT of a 252.7 MeV proton cycle, b) FT of a 62.4 MeV proton cycle with 50 % intensity, c) FB of a proton cycle, d) FT of a 252.7 MeV proton cycle with an constant frequency offset of 350 Hz and e) FB of a carbon beam. In all proton test cases the discrepancy is minimised for $\frac{\mathrm{V}}{\mathrm{V_{nom}}} \approx 1.43$, whereas the reconstruction of the carbon measurements is best for $\frac{\mathrm{V}}{\mathrm{V_{nom}}} \approx 1.46$.

To ensure the voltage mismatch is not only present in the reconstruction, the waterfall diagram of each test case is investigated in the next section, with particular focus on extracting an estimate of the synchrotron tune from measurements and comparing it to simulations and analytic approximations.

4.3.1 Synchrotron Tune Investigations

The waterfall diagrams of the test cases, whose minimisation of the discrepancy with higher input voltages was already shown in Fig. 4.14, were carefully analysed.

V1, Quadrupolar-Mode Oscillations due to a Voltage Jump of 126%: Figure 4.15 shows the measured and simulated waterfall diagram of a 252.7 MeV proton beam, which is mismatched at FT due to an instantaneous voltage jump from 663.52 to 1500 V. The waterfall clearly features the expected quadrupolar-mode oscillations due to the bucket height increase by 50%, which is initiated by the applied voltage jump as the longitudinal distribution no longer matches the bucket shape. The time intervals corresponding to both long and short bunch lengths or small and large momentum spread, respectively, are indicated in Fig. 4.15 with a blue and red box. The bright blue line represents the symmetry point for each tun, calculated with Eq. 3.4. By visually determining the turns needed for the beam to complete one synchrotron period, the synchrotron tune can be estimated. For quadrupolar-mode oscillations the borders of every second high relative momentum spread region were used to estimate the middle of this region, see Fig. 4.16. Estimating the synchrotron tune from the measurements yields $Q_s = 5.2 \times 10^{-4} \mathrel{\widehat{=}} 1928$ turns. The difference to the synchrotron tune, given as output in BLonD simulation and computed analytically, $Q_s = 4.4 \times 10^{-4} \mathrel{\widehat{=}} 2246$ turns can be explained by a discrepancy in the assumed cavity voltage. From the equation for the

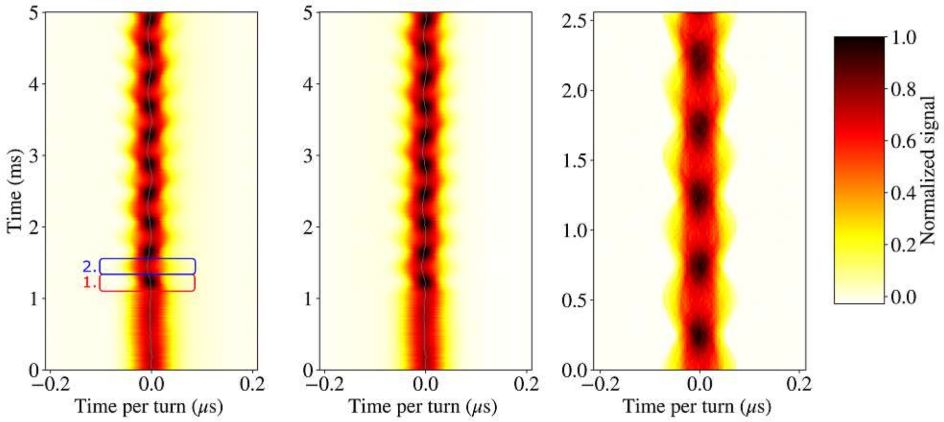

a) SADS b) μTCA c) BLonD

Figure 4.15: Waterfall diagrams, when instantaneously increasing the bucket voltage from the nominal 663 V to 1500 V, test case V1. The profiles are acquired with the a) SADS, the b) μTCA-crate and c) BLonD simulations. The red box indicates a time interval, during which the beam has a small bunch length and large momentum spread δ . The beam subsequently rotates in phase space, increasing the length and decreasing δ (blue box).

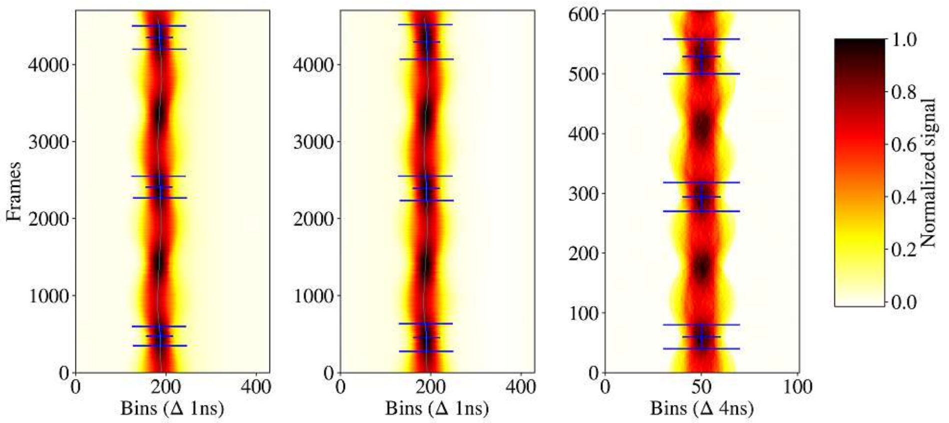

a) SADS b) μTCA c) BLonD

Figure 4.16: Waterfall diagrams of V1 zoomed in with visualisation of the synchrotron tune. Between each BLonD simulation frame 10 turns were performed (note the different horizontal scale).

synchrotron tune

$$Q_{s,0} = \frac{\omega_s}{\omega_0} = \sqrt{\frac{hqV|\eta_0 \cos(\Phi_s)|}{2\pi\beta^2 E}} \tag{4.3}$$

the relation

$$\left(\frac{Q_2}{Q_1}\right)^2 = \frac{\mathrm{V}_2}{\mathrm{V}_1} \tag{4.4}$$

can be derived. This observed difference in synchrotron tune can be explained by a voltage mismatch of $\mathrm{V}_2 \approx 1.35 \times \mathrm{V}_1$. Lastly, in order to establish the validity of the visual estimation of the synchrotron tune described above, the simulated tune is also determined from the BLonD simulation waterfall, which leads to $Q_s = 4.3 \times 10^{-4} \mathrel{\widehat{=}} 2345$ turns. The difference of ≈ 100 turns is attributed to errors when visually determining the maxima and minima of the oscillations, which is enhanced by the fact that only every 10th simulated profile is saved for the waterfall diagram. Looking at the propagation of uncertainty for the synchrotron tune (Eqs. 1.27 and 4.3)

$$\Delta Q = \frac{\partial Q}{\partial \mathrm{V}}\Delta \mathrm{V} + \frac{\partial Q}{\partial E}\Delta E + \frac{\partial Q}{\partial \alpha_c}\Delta\alpha_c \tag{4.5}$$

shows $\frac{\partial Q}{\partial \mathrm{V}} \approx 10^{-7}$, $\frac{\partial Q}{\partial E} \approx -10^{-12}$, if η and β are expressed with E and E_0, and $\frac{\partial Q}{\partial \alpha_c} \approx 10^{-4}$. Consequently, the energy difference for a discrepancy in synchrotron tune of $\mathcal{O}(10^{-4})$ has to be of $\mathcal{O}(10\,\mathrm{MeV})$. In a medical synchrotron the energy is well defined thus an energy offset of several 10 MeV can be ruled out. The momentum compaction factor α_c would have to change by 47% to facilitate the synchrotron tune change from 4.4×10^{-4} to 5.2×10^{-4}. As the momentum compaction factor is defined by the lattice, a discrepancy

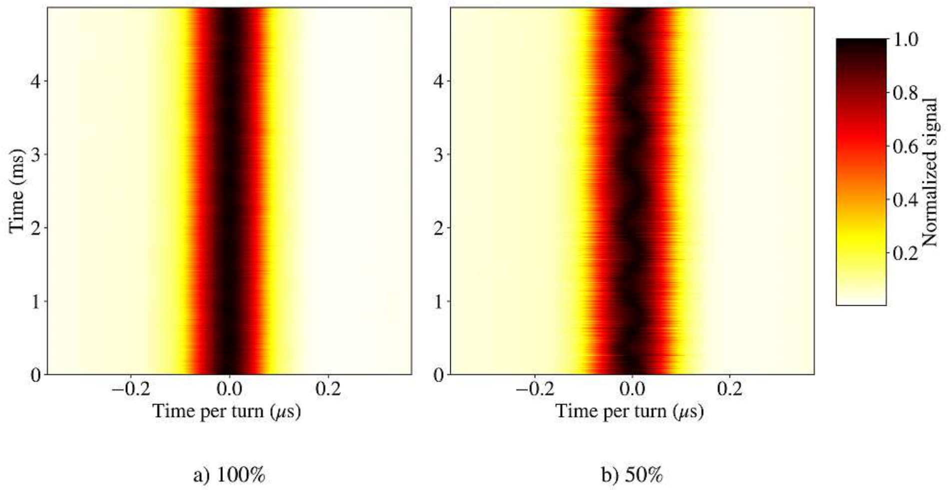

a) 100% b) 50%

Figure 4.17: Waterfall diagrams at FT of a 62.4 MeV proton cycle with 100 (P3) and 50 % (P4) intensity recorded by µTCA-crate. The waterfall of the lower intensity shows dipolar-mode oscillations.

this big is improbable. The other parameters $h = 1$, $q = 1$ and $E_0 = 938.272\,\mathrm{MeV}$ are also well defined. The only variable that is suspect to change is the cavity voltage.

P4, Proton Beam with 50% Intensity, measured at FT of a 62.4 MeV cycle: The measurements at FT of a 62.4 MeV proton cycle were performed with design intensity (100 %) and reduced intensity of 50 %. Figure 4.17 depicts the waterfall diagrams of the µTCA acquisition for 100 and 50 % intensity. Looking closely at Fig. 4.17b, dipolar-mode oscillations can be observed. As the oscillations are too small to visually ascertain, no reliable synchrotron tune estimate can be obtained from the waterfall diagram. However, as described above, the oscillations are accurately reconstructed with $\mathrm{V}_2 \approx 1.42 \times \mathrm{V}_1$.

P1, Proton Beam with 100% Intensity, measured at FB (7 MeV): At FB, before acceleration but after capture, the beam occupies most of the bucket. This can be seen in Fig. 4.18, where the measured longitudinal profiles (a and b) and the BLonD simulated profiles (c) span most of the revolution period. The measured waterfall diagrams shows off-centre particles performing oscillations. The first and second left-hand local maxima are separated by ≈ 1143 turns. The particles performing the oscillation have a phase offset of $\Delta\Phi \approx 102°$. By considering the amplitude-detuning, described in Section 1.1.4, the synchrotron tune for the synchronous particle $Q_{s,0}$, called *central* synchrotron tune, can be calculated. For $\Delta\Phi \approx 102°$ phase offset the synchrotron tune is consequently expected to decrease by 0.78, see Fig. 1.5. The estimated tune is $Q_s \approx 8.75 \times 10^{-4}$, which yields a small-amplitude synchrotron tune of $Q_{s,0} \approx 1.11 \times 10^{-3} \mathrel{\widehat{=}} 881$ turns. The Q_s gained from simulations is 9.25×10^{-4}. Assuming that energy and α_c are equal for simulation and measurement, this tune difference can be explained by a voltage discrepancy of

$V_2 \approx 1.43 \times V_1$.

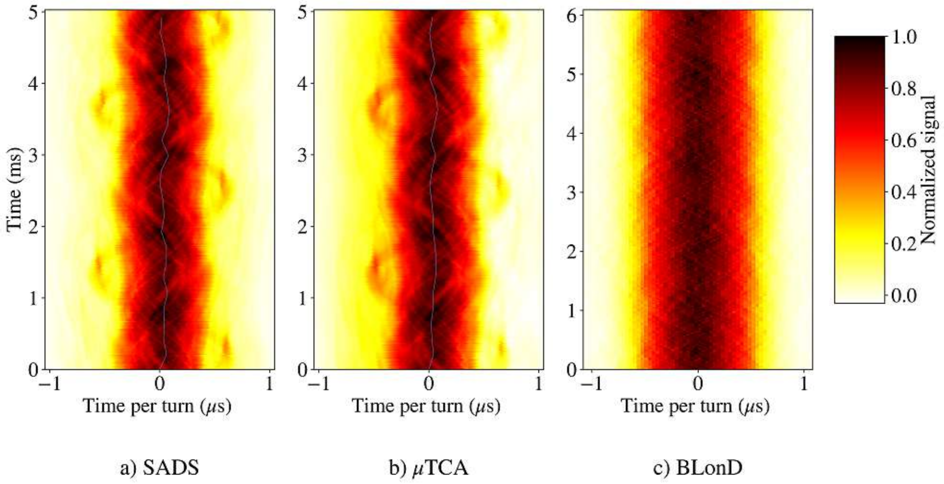

a) SADS b) μTCA c) BLonD

Figure 4.18: Waterfall diagrams at FB of proton cycle, test case P1. Profiles are acquired with a) the SADS, b) the µTCA-crate and obatianed from c) BlonD simulations.

K1, Dipolar-Mode Oscillations due to a Frequency Offset of 350 Hz: The baseline corrected and normalised waterfall diagrams of the K1 measurements (dipolar-mode oscillations introduced by frequency offset, which translate in an energy mismatch for a stationary 252.7 MeV proton beam) and simulations are shown in Fig. 4.19. The measured phase offset for SADS and µTCA is $\Delta\Phi \approx 24 - 25\,^\circ$ and the BLonD simulation with the adapted circumference and a modified initial beam distribution in the longitudinal phase space yields an offset of $\Delta\Phi \approx 28\,^\circ$. The most extreme symmetry points were evaluated and used to calculate the synchrotron tune of the measurements. The $Q_{s,0}$ obtained from measurements is $Q_{s,0} \approx 3.5 \times 10^{-4} \mathrel{\widehat{=}} 2857$ turns. As in the previously presented cases, this value differs from the Q_s obtained from simulations ($Q_s = 3.0 \times 10^{-4} \mathrel{\widehat{=}} 3377$ turns), which can again be attributed to a voltage difference of $\frac{V_2}{V_1} \approx 40\%$.,

C1, Carbon Beam with 100% Intensity, measured at FB (7 MeV/u): The longitudinal profiles acquired at FB of a nominal carbon cycle, visualised in Fig. 4.20, exhibit oscillations similar to the oscillations seen in Fig. 4.18, the FB of a proton cycle. An accumulation of filamenting particles is observed, which feature a maximum phase offset of $\Delta\Phi \approx 82° = 1.43$ rad. This oscillation takes about 1023 turns to complete, which leads to a synchrotron tune of $Q_s = 9.78 \times 10^{-4}$. Using Fig. 1.5, where the relation of $\frac{Q_s}{Q_{s0}}$ is plotted, the central synchrotron tune is calculated to be $Q_{s,0} = 1.09 \times 10^{-3}$. Again, the observed discrepancy between the measured and simulated synchrotron tune can be explained by a voltage error of $\frac{V_2}{V_1} \approx 40\%$.

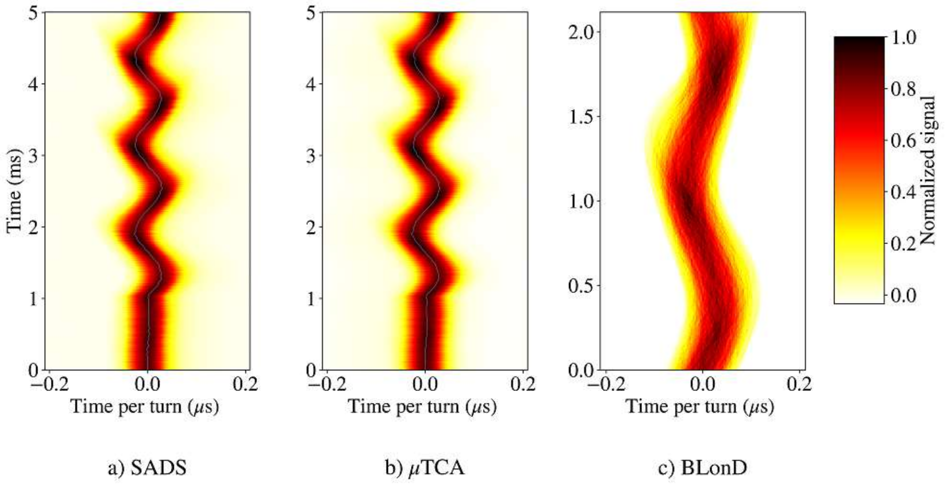

a) SADS b) μTCA c) BLonD

Figure 4.19: Waterfall diagrams after constant frequency offset of 350 Hz, test case K1, acquired with a) the SADS, b) the μTCA and obtained from c) BLonD simulations with a changed circumference and an initial distribution with energy offset.

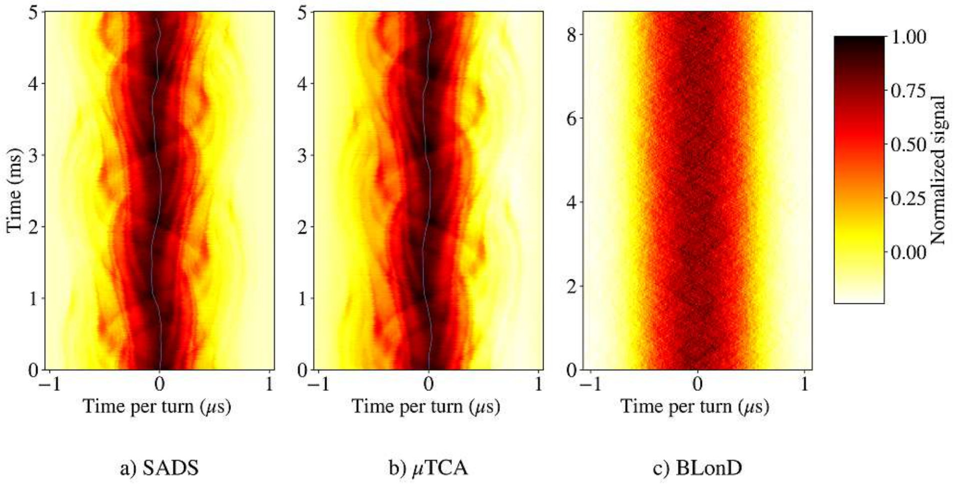

a) SADS b) μTCA c) BLonD

Figure 4.20: Waterfall diagrams at FB of a standard carbon cycle, test case C1, recorded with a) the SADS, b) the μTCA-crate and c) created with BLonD simulations.

4.3.2 Summary of Implications for the Tomography Set-Up

After failed and unsatisfying reconstructions of non-operational beams, a sweep of the RF cavity voltage used as input parameter was proposed [49]. These sweeps showed that the reconstruction quality improved for input voltage V_{rec} higher than the assumed operational voltage V_{nom}, $V_{rec} \approx 1.4 \times V_{nom}$. This could be seen in animations of the evolution of the longitudinal phase space distribution within the measured synchrotron period and the minimisation of the discrepancy, see Fig. 4.14. In Table 4.6 the estimated voltage discrepancy obtained from reconstructions and from analysing the waterfall diagrams are summarised. Due to similarity of the estimated cavity voltage present in waterfall diagrams and the reconstruction, all further reconstruction will use $\mathrm{V}_{\mathrm{rec}} = 1.42 \times \mathrm{V}_{\mathrm{nom}}$.

Case	Voltage Error from Reconstruction	Voltage Error from Waterfall Diagram
V1	1.43	1.35
P4	1.43	1.42
P1	1.43	1.43
K1	1.43	1.40
C1	1.46	1.40

Table 4.6: Summarising table of voltage discrepancy obtained from minimisation of the discrepancy of reconstructions and from measured waterfall diagrams via visual estimation.

Effect of Voltage Error on Matched and Mismatched Beams: As shown in Fig. 4.14 the reconstruction of mismatched beams significantly improves with a higher voltage. This is also displayed in Fig. 4.21, where a poor reconstruction with the nominal RF cavity voltage $\mathrm{V}_{\mathrm{nom}}$ and a better reconstruction with $1.42 \times \mathrm{V}_{\mathrm{nom}}$ are displayed. Additionally a matched distribution at FT of a 62.4 MeV proton was reconstructed with two voltage values to visualise the effect of the voltage error on the obtained beam parameters for the most simplistic case ($\Phi_s = 0$, $\dot{\mathrm{V}} = 0$, $\dot{\mathrm{B}} = 0$) with a symmetric and periodic beam signal. The resulting reconstructions are illustrated in Fig. 4.21 and the obtained longitudinal beam parameters are summarised in Table 4.7. The averaged longitudinal parameters gained from the phase space distribution every 100th time instance in three separate measurements. By increasing the voltage by 42%, the δ_{rms} increases by $\approx 18\%$.

Acquisition System	ϵ_{L} $[10^{-2}\,\mathrm{eVs}]$	δ_{rms} $[10^{-4}]$	$\mathbf{l}$ [ns]	Voltage [V]
SADS	1.49 ± 0.02	6.59 ± 0.04	241 ± 1.51	923.5
SADS	1.26 ± 0.01	5.54 ± 0.04	242 ± 1.45	652.9
µTCA	1.21 ± 0.02	5.99 ± 0.05	215 ± 1.97	923.5
µTCA	1.04 ± 0.01	5.08 ± 0.03	218 ± 01.86	652.9

Table 4.7: Longitudinal beam parameters obtained from the tomographic reconstruction of the SADS and µTCA-crate acquisitions at FT of a 62.4 MeV proton cycle with 100% intensity, test case P3. Reconstructions were performed with $\mathrm{V}_{\mathrm{nom}} = 652.9\,\mathrm{V}$ and $1.42 \times \mathrm{V}_{\mathrm{nom}}$. The reconstructed relative momentum spread rises by 18%, while the bunch length stays virtually constant, for an increase in RF cavity voltage of 42%.

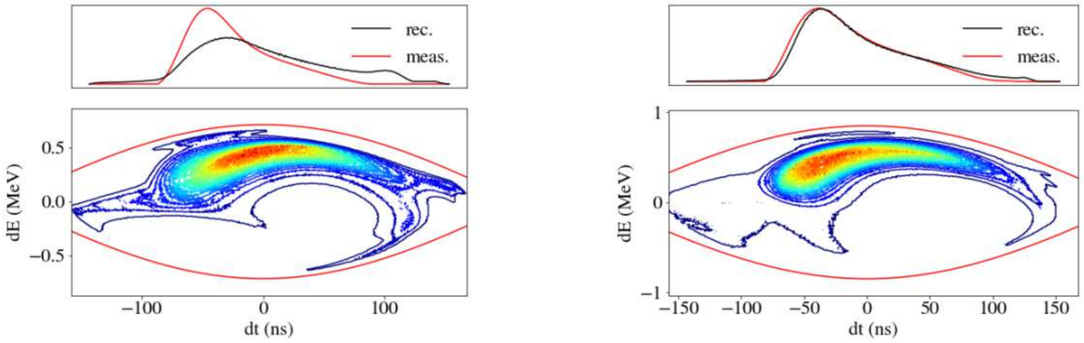

a) F2 reconstruction with operationally set voltage $V_{\text{nom}} = 663.5\,\text{V}$

b) F2 reconstruction with operationally set voltage $V_{\text{rec}} = 1.42 \times 663.5\,\text{V}$

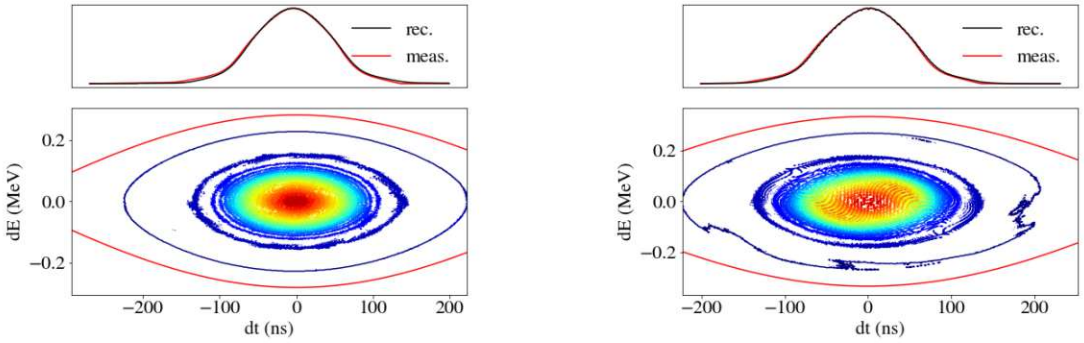

c) P3 reconstruction with operationally set voltage $V_{\text{nom}} = 652.9\,\text{V}$

d) P3 reconstruction with operationally set voltage $V_{\text{rec}} = 1.42 \times 652.9\,\text{V}$

Figure 4.21: Effect of input voltage on the reconstruction of mismatched and matched longitudinal phase space distributions. The reconstruction of the mismatch, specifically the dipolar-mode oscillations due to a phase offset, test case F2, greatly improve for the reconstruction with b) $V_{\text{rec}} = 1.42 \times 663.5\,\text{V}$ instead of a) $V_{\text{rec}} = V_{\text{nom}} = 663.5\,\text{V}$. The matched longitudinal phase space distribution is visually less affected by the increased voltage, as can be seen when comparing c) and d). The quantitative momentum spread increase corresponding to the increased bucket height is discussed in Table 4.7.

Measurements of RF Cavity Voltage: In a service slot shift the combined cavity signal (RFH-A) was recorded and a LeCroy WaveRunner 104MXi-A 1 GHz oscilloscope was connected to the monitor signal of each of the 12 cavity cells in the synchrotron hall for subsequent measurements. The contribution of each cell to the sum signal is unequal but reproducible. While these measurements show a difference between the voltage of the cavity and the voltage, which the LLRF regulates based on, further investigations are necessary.

4.4 Analysis of the Tomographic Reconstruction Performance

Taking into account the presented findings above concerning the quality of the acquired bunch profiles and the RF cavity voltage calibration, this section will present first results of the test cases listed in Section 4.1. All reconstructions were performed with $V_{\text{rec}} = 1.42 \times V_{\text{nom}}$ unless explicitly stated otherwise. To ensure the reproducibility of these measurements at MedAustron the nominal RF cavity voltage V_{nom} will be provided for each reconstruction.

All test cases were simulated with BLonD and the phase space was also reconstructed based on simulated profiles. However, these simulations were performed with the operationally assumed voltage and synchronous phase settings and are hence only presented for qualitative comparison.

4.4.1 Reconstruction of Matched Longitudinal Phase Space Distributions

The test series P, Table 4.1, and C, Table 4.2, comprise measurements taken of operational, matched proton and carbon beams with nominal and reduced intensities. In the following subsections, the reconstructed phase spaces are illustrated and described.

P1: Proton Beam with 100% Intensity, Measured at FB (7 MeV)

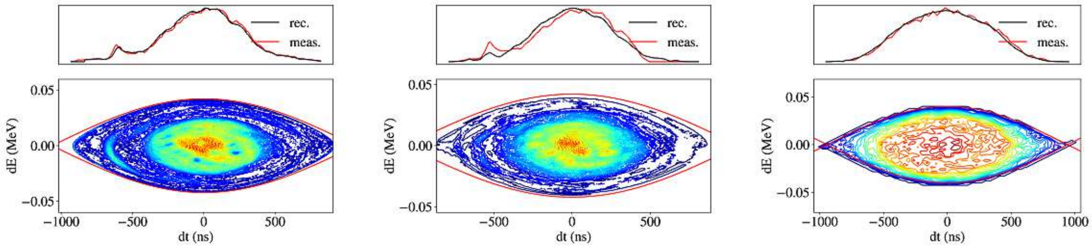

a) SADS b) µTCA c) BLonD simulation

Figure 4.22: Reconstructed phase space at FB of a proton cycle, test case P1. Profiles taken from the a) SADS acquisition, the b) µTCA-crate acquisition and c) BLonD simulation. For this test case the nominal RF cavity voltage is $V_{\text{nom}} = 103\,\text{V}$.

The reconstructed phase space distributions, based on longitudinal profiles acquired with the SADS and µTCA-crate, are illustrated in Fig. 4.22, as well as a reconstruction based on profiles obtained from BLonD simulations. As stated above, the BLonD simulations, as well as their reconstructions, are performed with the assumed operational voltage settings and are therefore only listed for qualitative comparison.

It is evident, that the discrepancy between the reconstructed and measured profiles is larger for the µTCA-crate than for the SADS measurements. This is attributed to the asymmetry and baseline distortion, observed in the µTCA-crate at low energies, as discussed in Section 4.2. The reconstructed beam behaviour in the longitudinal phase space at FB is more accurately depicted with the SADS measurements. Table 4.8 lists the parameters, which are extracted from the phase space reconstruction, averaged over every 100th profile used in the reconstructions of the three acquisitions. The longitudinal emittance, the relative momentum spread and bunch length for SADS measurements are larger by 25, 8 and 15% respectively, than when being acquired with the µTCA-crate. This might be due to the baseline correction applied in the tomography code, which takes the first 5% of the reference profile as baseline. The higher baseline, combined with the baseline distortion, might be the cause for the difference in the reconstructed parameters.

Acquisition System	ϵ_{L} [10^{-2} eVs]	δ_{rms} [10^{-3}]	l [µs]
SADS	1.43 ± 0.05	1.08 ± 0.03	1.20 ± 0.04
µTCA	1.14 ± 0.01	1.00 ± 0.02	1.04 ± 0.02

Table 4.8: Longitudinal beam parameters obtained from the tomographic reconstruction of the SADS and µTCA-crate acquisitions at FB of a 100% intensity proton cycle, test case P1. For this test case the nominal RF cavity voltage is $\mathrm{V_{nom}} = 103\,\mathrm{V}$.

In 2016, during the proton beam commissioning at MedAustron, an empty bucket scan was performed for estimating the momentum spread at FB [40]. This measurement yielded a momentum spread of $\delta = 9.65 \times 10^{-4}$ for a full intensity proton beam, which is comparable to the momentum spreads attained by the reconstruction.

P2: Proton Beam with 50% Intensity, Measured at FB (7 MeV)

The waterfall diagrams of one of the three measurements taken at FB of an operational proton cycle with 50% intensity is shown in Fig. 4.23. The depicted waterfall diagram are similar to the full intensity (Fig. 4.18). This is reflected in the similar values of the estimated longitudinal beam parameters in Table 4.9 for 50% and 100% intensity in Table 4.8.

P3: Proton Beam with 100% Intensity, Measured at FT of a 62.4 MeV Cycle

In Table 4.10 the reconstructed longitudinal beam parameters are presented, averaged over several time instances with in the three measurements. Again, the beam parameters computed from the SADS acquisitions are 23, 9 and 12% larger than the ones from the µTCA-crate measurement, which is attributed to the observed tail in the acquired

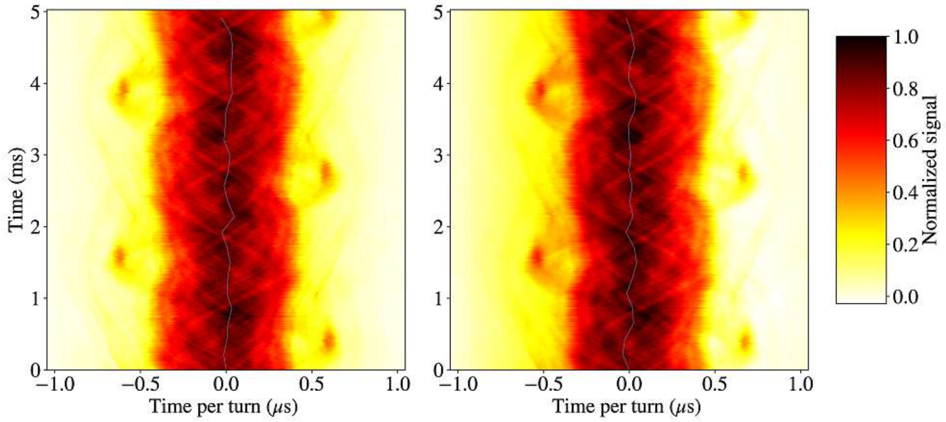

a) SADS

b) μTCA

Figure 4.23: Waterfall diagrams at FB of a proton cycle with 50% intensity, test case P2, acquired with the a) SADS and the b) µTCA-crate.

Acquisition System	ϵ_L [10^{-2} eVs]	δ_{rms} [10^{-3}]	l [µs]
SADS	1.44 ±0.03	1.10 ±0.04	1.19 ±0.04
µTCA	1.33 ±0.11	1.06 ±0.05	1.14 ±0.07

Table 4.9: Longitudinal beam parameters obtained from the tomographic reconstruction of the SADS and µTCA-crate acquisitions at FB of a 50% intensity proton cycle, test case P2. For this test case the nominal RF cavity voltage is $V_{nom} = 103\,V$.

Acquisition System	ϵ_L [10^{-2} eVs]	δ_{rms} [10^{-4}]	l [ns]
SADS	1.49 ± 0.02	6.59 ± 0.04	241 ± 1.51
µTCA	1.21 ± 0.02	5.99 ± 0.05	215 ± 1.97

Table 4.10: Longitudinal beam parameters obtained from the tomographic reconstruction of the SADS and µTCA-crate acquisitions at FT of a 62.4 MeV proton cycle with 100% intensity, test case P3. The nominal voltage for this test case is $V_{nom} = 652.9\,V$.

longitudinal profiles, as described in Section 4.2. The waterfall diagram of one P3 measurement can be seen in Fig. 4.17a and the reconstructed phase space distributions are illustrated in Fig. 4.21c and d.

The empty bucket scan of a 62.4 MeV proton beam with 10% intensity at FT during commissioning yielded a momentum spread of $\delta \approx 4.95 \times 10^{-4}$ [40]. The discrepancy between the momentum spread reconstructed from PU measurements and measured with the empty bucket scan might be due to the different intensities. To provide a current alternative reference measurement, new momentum spread measurements were performed with the Schottky frequency analyser. For this, the beam was debunched 1 ms prior to the cycle time at which the tomography data was acquired. Subsequently a Schottky spectrum was acquired over 100 ms resulting in $\delta \approx 6.22 \times 10^{-4} \pm 0.51 \times 10^{-4}$, which is in agreement with the values obtained with the tomography.

P4: Proton Beam with 50% Intensity, Measured at FT of a 62.4 MeV Cycle

The reconstructed phase space distribution of an operational 62.4 MeV proton beam with 50% intensity is illustrated in Fig. 4.24. The respective beam parameters, listed in Table 4.11, are for both acquisition systems approximately 10% larger than the respective values obtained for a 62.4 MeV proton beam with 100% intensity (Table 4.7). As described in Section 4.3, the waterfall diagram (Fig. 4.17) features small dipolar-oscillations, which can be explained by a previous mismatch along the cycle, which might still be visible at the measurement times, because of smaller decoherence rates due to the reduced intensity and related space charge effects. The tomographic reconstruction accurately reconstructs these coherent bunch oscillations, as visible in Fig. 4.24a and b, which illustrates two different time instances during one synchrotron oscillation.

Acquisition System	ϵ_L [10^{-2} eVs]	δ_{rms} [10^{-4}]	l [ns]
SADS	1.66 ± 0.06	6.88 ± 0.11	257 ± 5.29
µTCA	1.31 ± 0.03	6.23 ± 0.05	223 ± 2.64

Table 4.11: Longitudinal beam parameters obtained from the tomographic reconstruction of the SADS and µTCA-crate acquisitions at FT of a 50% intensity 62.4 MeV proton cycle, test case P4.

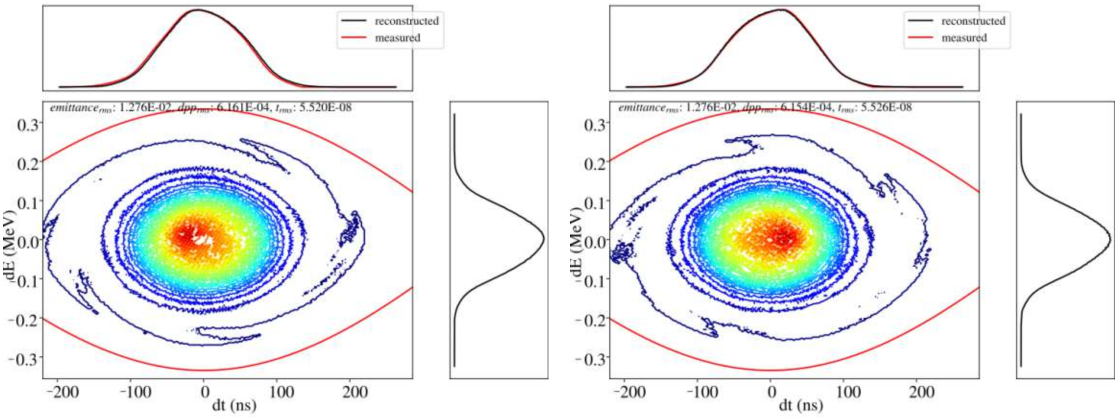

Figure 4.24: Reconstructed phase space at FT of a 62.4 MeV proton cycle with 50% intensity, test case P4. Two profiles from the µTCA-crate acquisition are depicted. For this test case the nominal RF cavity voltage is $V_{nom} = 652.9\,V$.

The estimate for the longitudinal beam parameters listed in Table 4.11 is, as described above, based on averaging the respective values obtained from both, all reconstructed time instances as well as from the three separate acquisitions. This is considered to be acceptable as the slight dipolar-mode oscillation only displaces the bunch in energy and phase, but does not alter the shape of the distribution significantly. This is also evident when regarding the reconstructed parameters for the two time instances illustrated in Fig. 4.24. However, it will be discussed below that, for quadrupolar-mode oscillations or dipolar-mode oscillations with increased phase offsets, averaging the reconstructed beam parameters over all turns within one synchrotron period is not fully representative.

P5: Proton Beam with 100% Intensity, Measured at FT of a 252.7 MeV Cycle

Figure 4.25 shows the waterfall diagrams for one measurement of an operational 252.7 MeV proton beam with 100% intensity at FT, acquired with the SADS and the µTCA-crate, as well as simulated with BLonD. As described in Section 2.2, the RF cavity voltage is ramped to increase the momentum spread prior to the phase jump. This voltage ramp has to be considered in the reconstruction, by changing the respective parameter (Section 3.2.1). However within the 1.7 ms used in the reconstruction the voltage does not change significantly and the reconstructed beam parameters can be averaged over several time instances in the three separate measurements, as described before. These values can be found in Table 4.12. As before the values obtained from the SADS measurements are bigger than that of the µTCA-crate acquisitions, by 26, 11 and 13% for the longitudinal emittance, the relative momentum spread and the bunch length, respectively. The increase of all parameters might be caused by the tail of the SADS profiles, described in Section 4.2 (specifically Fig. 4.9). The momentum spread was also measured with the Schottky spectrum analyser. As described in Section 4.4.1, the beam was debunched

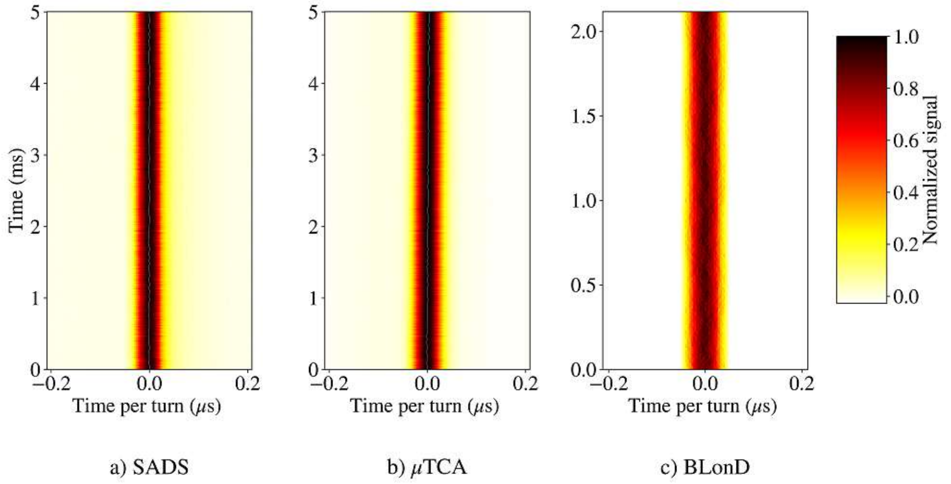

a) SADS b) µTCA c) BLonD

Figure 4.25: Waterfall diagrams at FB of a proton cycle with 100% intensity, test case P5, acquired with the a) SADS and the b) µTCA-crate and c) simulated with BLonD.

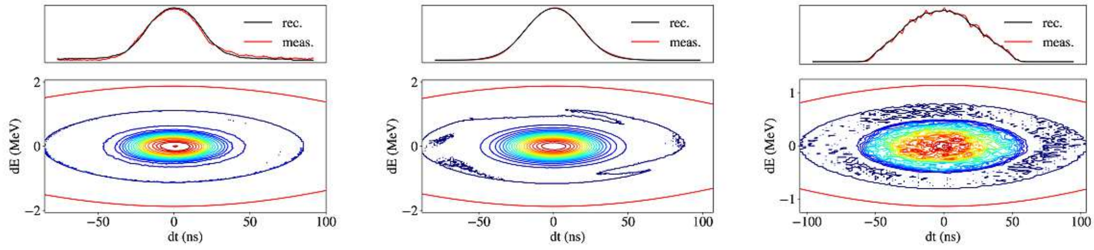

a) SADS b) µTCA c) BLonD simulation

Figure 4.26: Reconstructed phase space distribution at FT of a 252.7 MeV proton cycle with full intensity, test case P5. Profiles taken from the a) SADS acquisition, the b) µTCA-crate acquisition and c) BLonD simulations. For this test case the nominal RF cavity voltage is $\text{V}_{\text{nom}} = 663.5\,\text{V}$ and $\dot{\text{V}} = 33368.1\, V/s$.

1 ms before the reference acquisition time of the tomography. The Schottky monitor scanned the frequency range of interest within 100 ms. The measured momentum spread of $\delta = 6.5 \times 10^{-4} \pm 0.6 \times 10^{-4}$ agrees with the tomography results.

Acquisition System	ϵ_{L} [10^{-2} eVs]	δ_{rms} [10^{-4}]	$\mathbf{l}$ [ns]
SADS	2.07 ±0.02	6.64 ±0.03	89 ±0.45
µTCA	1.63 ±0.01	5.96 ±0.02	78 ±0.29

Table 4.12: Longitudinal beam parameters obtained from the tomographic reconstruction of the SADS and µTCA-crate acquisitions at FT of a 100% intensity 252.7 MeV proton cycle, test case P5. For this test case the nominal RF cavity voltage is $\text{V}_{\text{nom}} = 663.5\,\text{V}$ and $\dot{\text{V}} = 33\,368.1\,\text{V/s}$.

C1: Carbon Beam with 100% Intensity, Measured at FB (7 MeV/u)

In Fig. 4.27 the reconstruction of the SADS and µTCA-crate acquisitions, as well as the reconstructed phase distribution of a BLonD simulation are illustrated. As discussed for proton beams at FB (Section 4.4.1), the µTCA-crate reconstruction features higher discrepancy, due to the baseline distortion and the asymmetrical signal (see Section 4.2). The averaged values can be found in Table 4.13, where a difference of 11, 4 and 6% between the parameters (longitudinal emittance, relative momentum spread and bunch length), obtained from the SADS and the µTCA-crate measurements, is found. As mentioned before, this might be due to baseline correction within the tomography code, in which the first 5% of the reference profile are used to calculate the baseline.

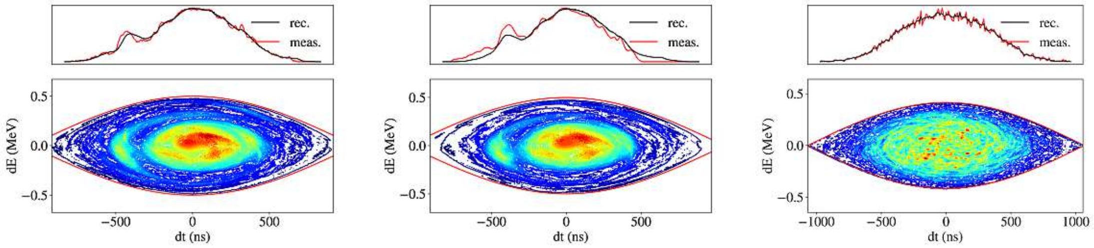

a) SADS. b) µTCA. c) BLonD simulation.

Figure 4.27: Reconstructed phase space at FB of a carbon cycle, test case C1. Profiles taken from the a) SADS acquisition, the b) µTCA-crate acquisition and c) BLonD simulations. For this test case the nominal RF cavity voltage is $V_{nom} = 200\,V$.

Acquisition System	ϵ_L [10^{-1} eVs]	δ_{rms} [10^{-3}]	l [µs]
SADS	1.69 ± 0.03	1.08 ± 0.32	1.19± 0.03
µTCA	1.52 ± 0.06	1.03 ± 0.38	1.12 ± 0.04

Table 4.13: Longitudinal beam parameters obtained from the tomographic reconstruction of the SADS and µTCA-crate acquisitions at FB of a 100% intensity carbon cycle, test case C1. For this test case the nominal RF cavity voltage is $V_{nom} = 200\,V$.

C2: Carbon Beam with 20% Intensity, Measured at FB (7 MeV/u)

Figure 4.28 displays the waterfall diagram of one measurement of a carbon beam with 20% intensity, measured at FB. The beam performs slight dipolar-mode oscillations. Additionally the baseline distortion, which was discussed in Section 4.2, specifically Figs. 4.12 and 4.13, leads to a less well defined beam signal. However, the reconstruction with the acquired PU signals was acceptable and the averaged longitudinal beam parameter values in Table 4.14 differ approximately +2% to the values at full intensity for the SADS acquisitions and -6% for the µTCA-crate measurements. Again the baseline distortion might be the cause of this behaviour.

Acquisition System	ϵ_L [10^{-1} eVs]	δ_{rms} [10^{-4}]	l [µs]
SADS	1.73 ±0.06	10.83 ±0.22	1.21 ±0.03
µTCA	1.39 ±0.06	9.96 ±0.26	1.06 ±0.03

Table 4.14: Longitudinal beam parameters obtained from the tomographic reconstruction of the SADS and µTCA-crate acquisitions at FB of a 20% intensity carbon cycle, test case C2. For this test case the nominal RF cavity voltage is $V_{nom} = 200\,V$.

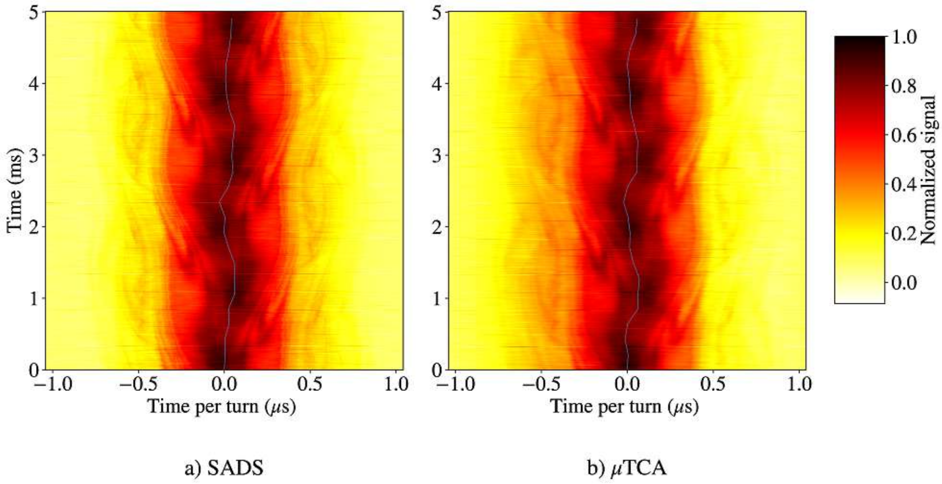

a) SADS

b) μTCA

Figure 4.28: Waterfall diagrams at FB of a carbon cycle with 20% intensity, test case C2, recorded with the a) SADS and the b) µTCA-crate.

C3: Carbon Beam with 100% Intensity, Measured at FT of a 120 MeV/u Cycle

As discussed with the profiles of 62.4 MeV proton beams (Fig. 4.8), the µTCA-signal exhibits more symmetry than the SADS signal. This can also be observed in the waterfall diagram (Fig. 4.29), when comparing the left- and right-hand-side of the SADS and the µTCA-crate measurements. At first sight, no significant impact of this asymmetry the reconstruction performance is observed. However, evaluating potential implications in detail goes beyond the scope of this thesis and is subject to further studies. The

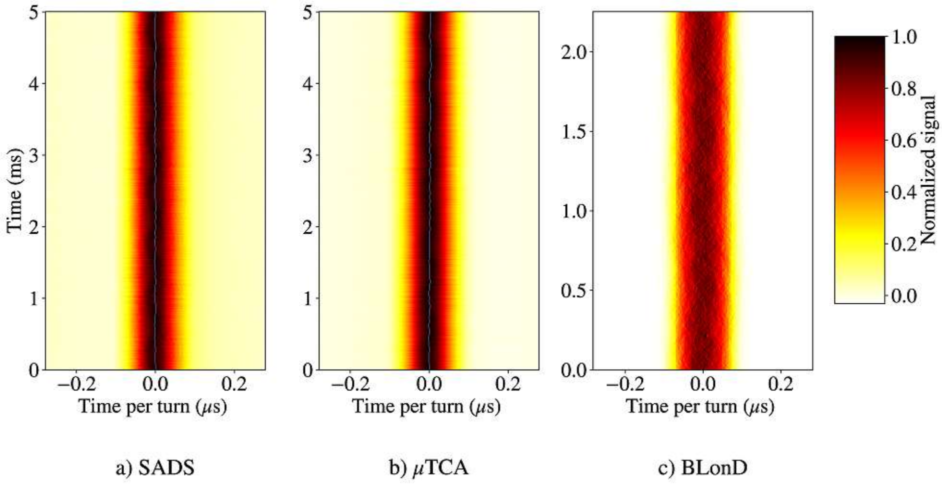

a) SADS

b) μTCA

c) BLonD

Figure 4.29: Waterfall diagram at FT of a 120 MeV/u carbon cycle, test case C3, recorded with the a) SADS and the b) µTCA-crate and c) simulated profiles with BLonD.

longitudinal parameter values gained from the reconstructed phase space distribution are averaged over several time instance of the three acquisitions and summarised in Table 4.15. Again, most likely due to the tail of the SADS profiles the obtained longitudinal emittance, the relative momentum spread and the bunch length are 28, 12 and 15% higher for these measurements than the values from µTCA-crate acquisitions.

Acquisition System	ϵ_L [10^{-1} eVs]	δ_{rms} [10^{-4}]	$\mathbf{l}$ [ns]
SADS	2.37 ± 0.04	6.20 ± 0.05	180 ± 1.54
µTCA	1.85 ± 0.02	5.56 ± 0.02	157 ± 0.72

Table 4.15: Longitudinal beam parameters obtained from the tomographic reconstruction of the SADS and µTCA-crate acquisitions at FT of a 100% intensity 120 MeV/u carbon cycle, test case C3. For this test case the nominal RF cavity voltage is $V_{\mathrm{nom}} = 1872.1\,\mathrm{V}$.

C4: Carbon Beam with 20% Intensity, Measured at FT of a 120 MeV/u Cycle

Measurements with the beam intensity set to 20% were also performed at FT of a 120 MeV/u carbon cycle. As for the measurement at FB (Fig. 4.28), the waterfall diagram at FT, shown in Fig. 4.30, displays a baseline distortion. The values reconstructed with $1.42 \times V_{\mathrm{nom}}$ yield similar values to the full intensity. These values can be found in Table 4.14, depicting the reconstructed values averaged every 100th profile over 4000 profiles in three separate measurements.

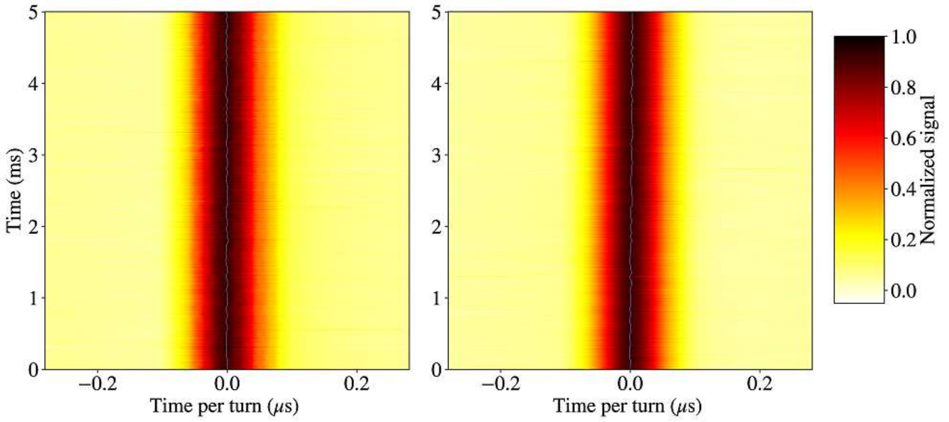

a) SADS

b) µTCA

Figure 4.30: Waterfall diagram at FT of a 120 MeV/u carbon cycle with 20% intensity, test case C4, recorded with the a) SADS and the b) µTCA-crate.

Acquisition System	ϵ_L [10^{-1} eVs]	δ_{rms} [10^{-4}]	l [ns]
SADS	2.27 ± 0.10	6.07 ± 0.12	176 ± 4.50
µTCA	1.89 ± 0.02	5.60 ± 0.03	159 ± 0.85

Table 4.16: Longitudinal beam parameters obtained from the tomographic reconstruction of the SADS and µTCA-crate acquisitions at FT of a 20% intensity 120 MeV/u carbon cycle, test case C4. For this test case the nominal RF cavity voltage is $V_{nom} = 1872.1\,V$.

C5: Carbon Beam with 100% Intensity, Measured at FT of a 402.8 MeV/u Cycle

Figure 4.31a displays a difference in the baseline of the left-hand-side and the right-hand-side of the shown SADS acquisition. Again, as also described for cases Section 4.4.1, these measurements feature a slight asymmetry in the SADS acquisitions, which is attributed to the tail observed in the profiles acquired with the SADS at FT energies (see Section 4.2). Table 4.17 presents the average of the reconstructed values every 100th turn over 4000 turns in three separate measurements. Here the biggest differences between the values obtained from the SADS and the µTCA-crate acquisition are found. The longitudinal emittance is 44% bigger for SADS profiles than for µTCA-crate signals, the relative momentum spread and bunch length are 17 and 23% bigger, respectively. The most likely cause for this significant difference is the noticeable tail of the SADS profiles, as described before.

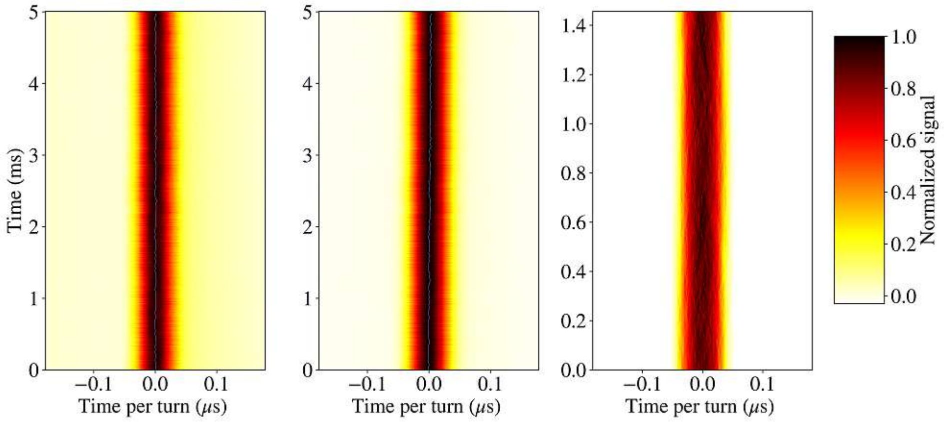

a) SADS b) µTCA c) BLonD

Figure 4.31: Waterfall diagrams at FT of a 402.8 MeV/u carbon cycle, test case C5, acquired with the a) SADS and the b) µTCA-crate and c) obtained from BLonD simulations.

Acquisition System	ϵ_L [10^{-1} eVs]	δ_{rms} [10^{-4}]	l [ns]
SADS	3.62 ± 0.12	5.07 ± 0.08	111 ± 2.08
µTCA	2.54 ± 0.07	4.36 ± 0.05	91 ± 1.38

Table 4.17: Longitudinal beam parameters obtained from the tomographic reconstruction of the SADS and µTCA-crate acquisitions at FT of a 100% intensity 402.8 MeV/u carbon cycle, test case C5. For this test case the nominal RF cavity voltage is $V_{nom} = 1963.6\,V$.

4.4.2 Reconstruction of Mismatched Beams

In this section the reconstruction and simulation of the test cases in Tables 4.3 to 4.5, which introduce quadrupolar- and dipolar-mode oscillations at FT of a 252.7 MeV proton beam with 100% intensity, are presented. As the longitudinal phase space distribution is intentionally mismatched, the reconstructed longitudinal beam parameters are no longer averaged over several time instances in one measurement.

V1: Quadrupolar-Mode Oscillations due to a Voltage Jump of 126%

Coherent quadrupolar-mode bunch oscillations are introduced by a voltage jump of the set voltage from 663.5 to 1500 V, i.e. an increase of 126%. The time intervals corresponding to both long and short bunch lengths or small and large momentum spread, respectively, are indicated in Fig. 4.15 with a blue and red box and are referred to as region 1 (large δ, small l) and 2 (small δ, large l). Table 4.18 depicts the longitudinal emittance ϵ_L,

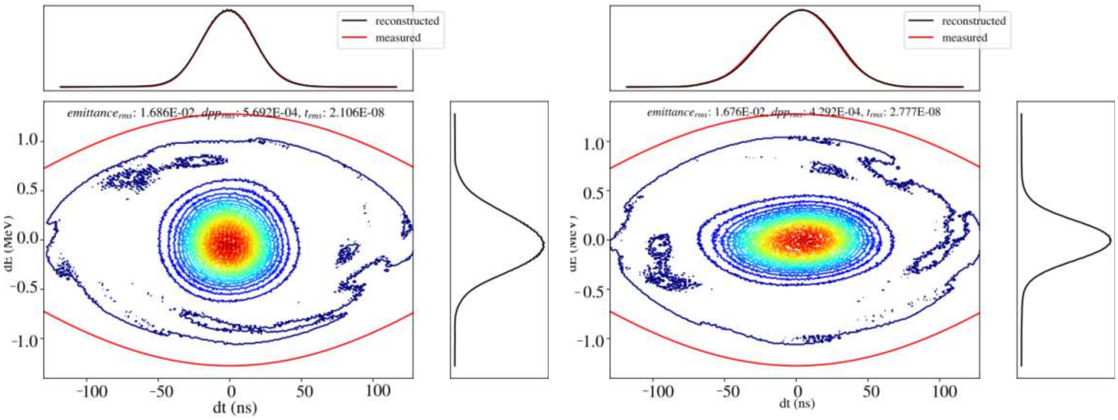

Figure 4.32: Reconstructed phase space during quadrupolar-mode oscillations introduced at FT of a 100% intensity 252.7 MeV proton cycle by an instantaneous voltage jump of 126%, test case V1. Two profiles from the µTCA-crate acquisition are depicted to visualise the difference between region 1 and 2. For this test case the nominal RF cavity voltage jumps from $V_{nom} = 663.52\,V$ to $V_{nom} = 1500\,V$.

the δ_{rms} and bunch length l defined as $4 \times t_{rms}$ reconstructed from three measurements.

Additionally, the values obtained from a BLonD simulation with the nominal RF cavity voltage settings and its reconstruction are shown for qualitative comparison between simulation and measurement. The observed effect is bigger in the simulation and its reconstruction with 50% difference in δ_{rms} from region 2 to region 1, compared to 25 and 30% with the SADS and µTCA-crate measurement, respectively. The reconstruction of one such measurement with the µTCA-crate is shown in Fig. 4.32 for region 1 and 2.

Acquisition System	ϵ_{L} [10^{-2} eVs]	δ_{rms} [10^{-4}]	$\mathbf{l}$ [ns]
SADS	1.91 ± 0.02	5.85 ± 0.01	93 ± 0.91
µTCA	1.67 ± 0.02	5.58 ± 0.06	85 ± 1.09
rec. BlonD	1.77	5.52	91
BlonD	1.68	5.58	86

a)

Acquisition System	ϵ_{L} [10^{-2} eVs]	δ_{rms} [10^{-4}]	$\mathbf{l}$ [ns]
SADS	1.89 ± 0.02	4.66 ± 0.03	115 ± 0.17
µTCA	1.67 ± 0.02	4.31 ± 0.06	110 ± 0.54
rec. BLonD	1.72	3.73	131
BLonD	1.68	3.71	129

b)

Table 4.18: Longitudinal beam parameters obtained from the tomographic reconstruction of the SADS and µTCA-crate acquisitions during quadrupolar-mode oscillations introduced at FT of a 100% intensity 252.7 MeV proton cycle by an instantaneous voltage jump of 126%, test case V1. The shown values are the a) maximum and b) minimum δ spread recorded within one synchrotron period averaged over three separate measurements. The BLonD simulation and reconstruction used the nominal RF cavity voltage $\mathsf{V}_{\mathsf{nom}} = 1500\,\mathsf{V}$, but the reconstruction of the SADS and µTCA-crate measurements used $\mathsf{V}_{\mathsf{rec}} = 1.42 \times \mathsf{V}_{\mathsf{nom}}$.

V2: Quadrupolar-Mode Oscillations due to a Voltage Jump of 35%

The same measurements were taken for a voltage jump from 663.52 V to 900 V, instead of 1500 V. Figure 4.33 shows the effect of the voltage jump becoming significantly lower. This is reflected in Table 4.19, where the reconstructed longitudinal beam parameters for region 1 and 2 of Fig. 4.33 are summarised. The difference of δ between region 1 and 2 is $\approx 15\%$ in the simulation and ≈ 10 and 14% for the SADS and µTCA reconstructions, respectively.

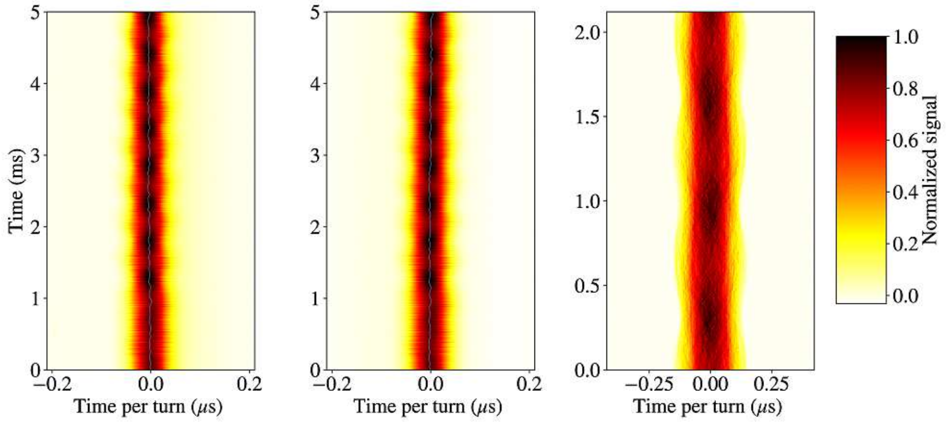

a) SADS b) μTCA c) BLonD

Figure 4.33: Waterfall diagrams showing the quadrupolar-mode oscillations introduced by a sudden voltage increase of 35% 1 ms after the beginning of the acquisition (a,b), test case V2. The profiles are obtained from the a) SADS-, the b) µTCA-crate-acquisitions and c) BLonD simulations, in which a matched beam distribution is loaded and an instantaneous voltage jump from 663.5 to 900 V is applied.

Acquisition System	ϵ_L [10^{-2} eVs]	δ_{rms} [10^{-4}]	**l** [ns]
SADS	1.85	4.71	111
µTCA	1.40	4.24	94
rec. BLonD	1.71	4.25	115
BLonD	1.68	4.29	112

a)

Acquisition System	ϵ_L [10^{-2} eVs]	δ_{rms} [10^{-4}]	**l** [ns]
SADS	1.83	4.27	122
µTCA	1.39	3.71	107
rec. BLonD	1.70	3.68	132
BLonD	1.68	3.71	129

b)

Table 4.19: Longitudinal beam parameters obtained from the tomographic reconstruction of the SADS and µTCA-crate acquisitions during quadrupolar-mode oscillations introduced at FT of a 100% intensity 252.7 MeV proton cycle by an instantaneous voltage jump of 35%, test case V2. The shown values are the a) maximum and b) minimum δ spread recorded within one synchrotron period. The BLonD simulation and reconstructions used the nominal RF cavity voltage $V_{nom} = 900$ V, but the reconstruction of the SADS and µTCA-crate measurements used $V_{rec} = 1.42 \times V_{nom}$.

F1: Dipolar-Mode Oscillations due to a Phase Offset of 36°

In this test case dipolar-mode coherent bunch oscillations were introduced by a short but large frequency offset of 5 kHz over 20 µs, during which a phase offset between RF cavity and beam phase could accumulate. Figure 4.34 shows the waterfall diagrams

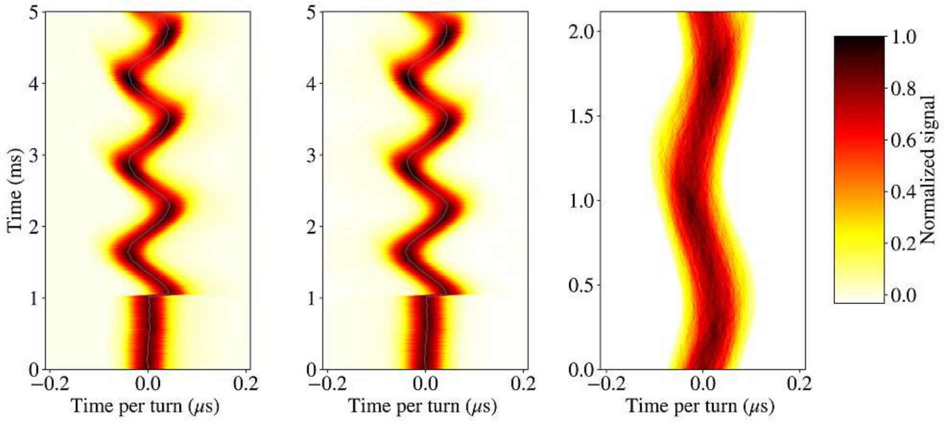

a) SADS b) μTCA c) BLonD

Figure 4.34: Waterfall diagrams of 5 kHz frequency jump at FT of 252.7 MeV proton cycle, which introduces dipolar-mode oscillations, test case F1, measured with the a) SADS and the b) µTCA-crate and c) shows the BLonD simulation with a phase offset of $\Delta\Phi\, 32.6°$. The measured oscillations fit the expected phase offset of $\Delta\Phi = 36°$.

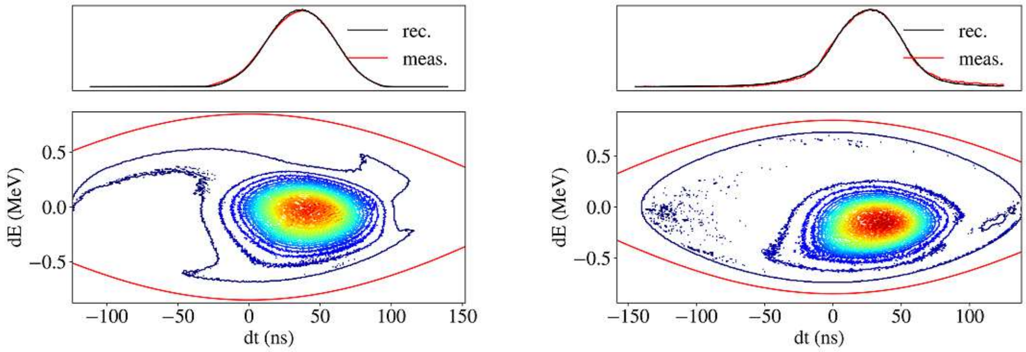

a) µTCA b) SADS

Figure 4.35: Reconstructed phase space of frequency jump of 5 kHz at FT of a 100% intensity 252.7 MeV proton cycle, test case F1. The frequency jump allows an accumulation of phase offset between RF cavity and beam phase. The resulting dipolar-mode oscillations are reconstructed from a) the µTCA-crate- and b) the SADS-acquisition. For this test case the nominal RF cavity voltage is $V_{\text{nom}} = 663.5\,\text{V}$.

measured with SADS and the µTCA-crate, where a clear start of these oscillations can be observed at 1 ms after the start of the acquisition. The maximum phase offset of the measured oscillations match the expected phase offset of $\Delta\Phi = 36°$. Additionally the BLonD simulation (Fig. 4.34c), performed as described in Section 4.1.3, shows an offset of $\Delta\Phi = 32.6°$. A snapshot of the reconstructed phase space 3600 turns after the first recorded profile and reference point is shown in Fig. 4.35 for both acquisition systems. The slight differences of the phase space distributions are most likely due the low-pass filter and the higher symmetry of µTCA-crate signal.

F2: Dipolar-Mode Oscillations due to a Phase Offset of 72°

The dipolar-mode oscillations are even more pronounced in measurements with a 10 kHz frequency jump over 20 µs, whose waterfall diagram is shown in Fig. 4.36. The measured

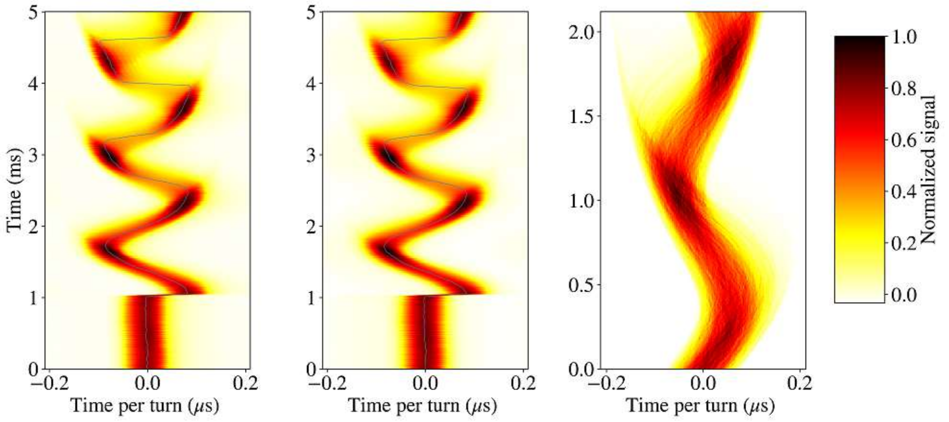

a) SADS b) µTCA c) BLonD

Figure 4.36: Waterfall diagrams of 10 kHz frequency jump at FT of 252.7 MeV proton cycle, which introduces dipolar-mode oscillations, test case F2, measured with the a) SADS and the b) µTCA-crate and c) shows the BLonD simulation with a phase offset of $\Delta\Phi\,68°$. The measured oscillations fit the expected phase offset of $\Delta\Phi = 72°$.

offset is in agreement with the calculated offset of $\Delta\Phi = 72°$, Eq. 4.1. The BLonD simulation, done similar to the procedure before in Section 4.4.2, shows a phase displacement of $\Delta\Phi \approx 68°$. Figure 4.37 showcases snapshots of the reconstruction 3600 profiles after the reference profile. While the reconstruction is not perfect, it still features the main characteristics of the measured profiles correctly and is thus considered as acceptable tool for such studies. These measurements nicely illustrate the fast decoherence rate and consequent filamentation of the mismatched distribution due to the strong non-linearities in the proximity of the separatrix.

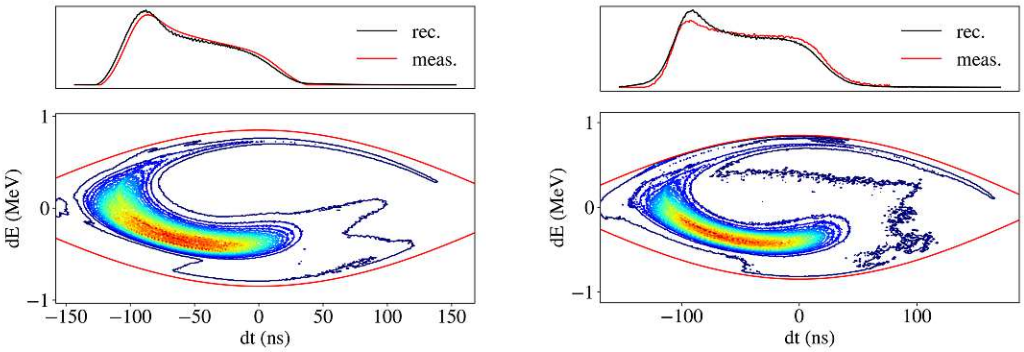

a) µTCA b) SADS

Figure 4.37: Reconstructed phase space of frequency jump of $10\,\mathrm{kHz}$ at FT of a 100% intensity 252.7 MeV proton cycle, test case F2. The frequency jump allows an accumulation of phase offset between RF cavity and beam phase. The resulting dipolar-mode oscillations are reconstructed from a) the µTCA-crate- and b) the SADS-acquisition. For this test case the nominal RF cavity voltage is $V_{\mathrm{nom}} = 663.5\,\mathrm{V}$.

K1: Dipolar-Mode Oscillations due to a Frequency Offset of 350 Hz

By introducing a constant frequency offset, an energy offset is created, which in turn leads to dipolar-mode oscillations. In Fig. 4.19 the waterfall diagrams acquired by the SADS and µTCA-crate of a constant frequency offset applied 1 ms after the trigger StartEVS are shown and compared to a BLonD simulation. The measured phase offset for SADS and µTCA is $\Delta\Phi \approx 24 - 25\,°$ and the BLonD simulation with the adapted circumference and a modified initial distribution yields an offset of $\Delta\Phi \approx 28\,°$. The reconstructed phase

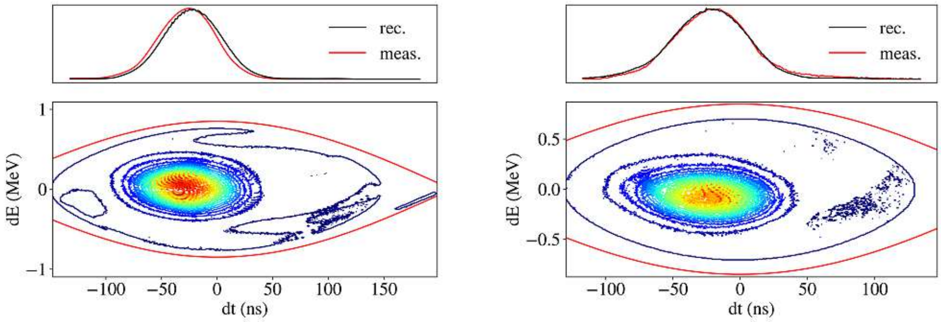

a) b)

Figure 4.38: Reconstructed phase space after frequency offset of 350 Hz at FT of a 100% intensity 252.7 MeV proton cycle, test case K1. The dipolar-mode oscillations, resulting from the energy offset, are reconstructed from the a) µTCA-crate- and the b) SADS-acquisition. For this test case the nominal RF cavity voltage is $V_{\mathrm{nom}} = 663.5\,\mathrm{V}$.

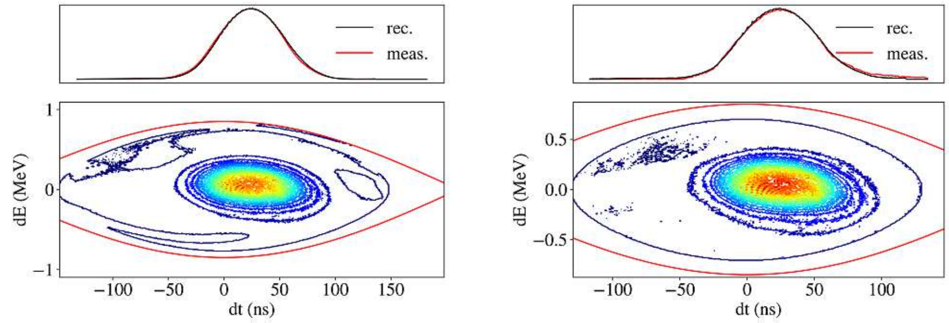

a) b)

Figure 4.39: Reconstructed phase space after frequency offset of 350 Hz at FT of a 100% intensity 252.7 MeV proton cycle, test case K1. The dipolar-mode oscillations, resulting from the energy offset, are reconstructed from the a) µTCA-crate- and the b) SADS-acquisition. For this test case the nominal RF cavity voltage is $V_{\text{nom}} = 663.5\,\text{V}$.

space of the two acquisition systems are remarkably similar, as can be seen in Fig. 4.38. In the Appendix the longitudinal profiles gained from the BLonD simulation within one synchrotron period are shown. These profiles are used in the reconstruction, which is also depicted in the Appendix.

K2: Dipolar-Mode Oscillations in a Bucket with Increased Height and a Frequency Offset of 416 Hz

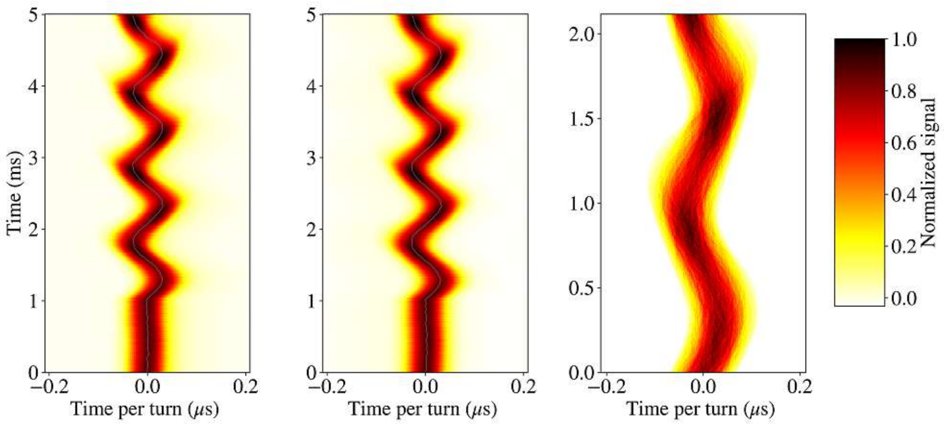

a) SADS b) μTCA c) BLonD

Figure 4.40: Waterfall diagrams showing the dipolar-mode oscillations caused by a constant frequency offset of 416 Hz after an adiabatic increase of the nominal voltage to 900 V. The measurements were taken at FT of a 252.7 MeV proton beam with full intensity and the aforementioned changes with the a) SADS, the b) µTCA-crate and simulated with c) BLonD with changed circumference and initial distribution with energy offset.

By increasing the bucket height, a higher constant frequency offset can be tested without losing the beam. The waterfall diagrams of the measurements with SADS and µTCA-crate are compared with a BLonD simulation in Fig. 4.40. The measurement show a proton 252.7 MeV cycle where the voltage is slowly increased from 663.5 to 900 V before the trigger event and a frequency offset of 416 Hz is applied 1 ms afterwards. In the measurements a maximal phase offset of the dipolar-mode oscillations is $\Delta\Phi \approx 26°$. The BLonD simulation shows a phase displacement of $\Delta\Phi = 32°$. The phase space distribution, shown in Fig. 4.41, is the reconstruction 3600 turns after the reference profile for µTCA-crate and SADS acquisitions.

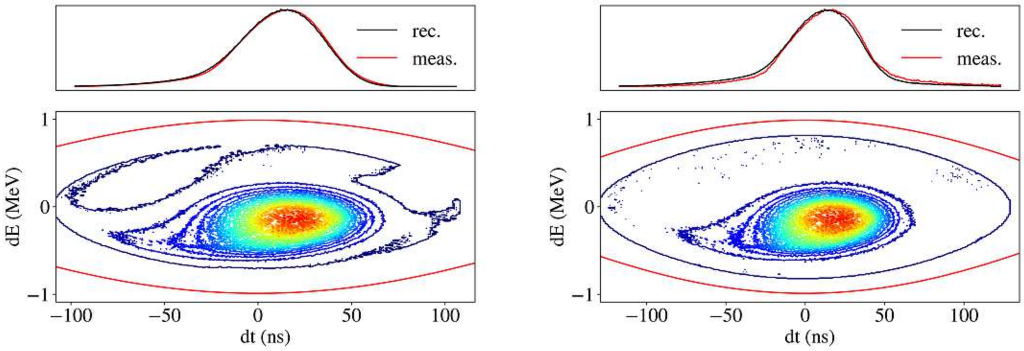

a) µTCA b) SADS

Figure 4.41: Reconstructed phase space after frequency offset of 416 Hz at FT of a 100% intensity 252.7 MeV proton cycle with adiabatic voltage increase to 900 V, test case K2. The dipolar-mode oscillations, resulting from the energy offset, are reconstructed from a and c) the µTCA-crate- and b and d) the SADS-acquisition. For this test case the nominal RF cavity voltage is $V_{nom} = 900\,V$.

4.5 Summary and Discussion

The key findings of these investigations is the feasibility of longitudinal tomography at MedAustron. For all test cases a reasonably good reconstruction was achieved for both acquisition systems, the µTCA-crate and the SADS, when basing the reconstruction on an RF cavity voltage $V_{rec} = 1.42 \times V_{nom}$, with V_{nom} being the operationally set voltage. In Fig. 4.42 the results obtained from the SADS and µTCA-crate measurements are compared for test case of series P, C and V, featuring the discrepancy as a measure for the quality of the tomographic reconstruction, as well as the longitudinal beam parameters gained from the reconstructed phase space distribution. The longitudinal beam parameters are shown as relative values of the SADS to the µTCA-crate reconstruction ($\frac{\epsilon_{L,\,SADS}}{\epsilon_{L,\mu TCA}}$, $\frac{\delta_{rms,\,SADS}}{\delta_{rms,\mu TCA}}$ and $\frac{l_{L,\,SADS}}{l_{L,\mu TCA}}$). The discrepancy plot affirms the discussion concerning the symmetry of the profiles: For lower energies the discrepancy from SADS reconstruction is lower than that of the µTCA-crate. This behaviour is most likely due to the asymmetric nature of the µTCA-crate profiles, discussed in Section 4.2. However, for higher energies, where the SADS profiles show a tail and less symmetry than the µTCA-crate profiles (Section 4.2), the discrepancy of the µTCA-crate reconstruction is lower than that of the SADS, most notable for P5 and C5. It is evident, that the longitudinal beam parameters extracted from the reconstruction of SADS measurements are systematically higher than the values obtained with the µTCA-crate. The $\delta_{\text{rms, SADS}}$ are in general 11-14% larger. The most extreme difference is observed in C5 measurements with a δ difference of 19% and 23% difference in the bunch length.

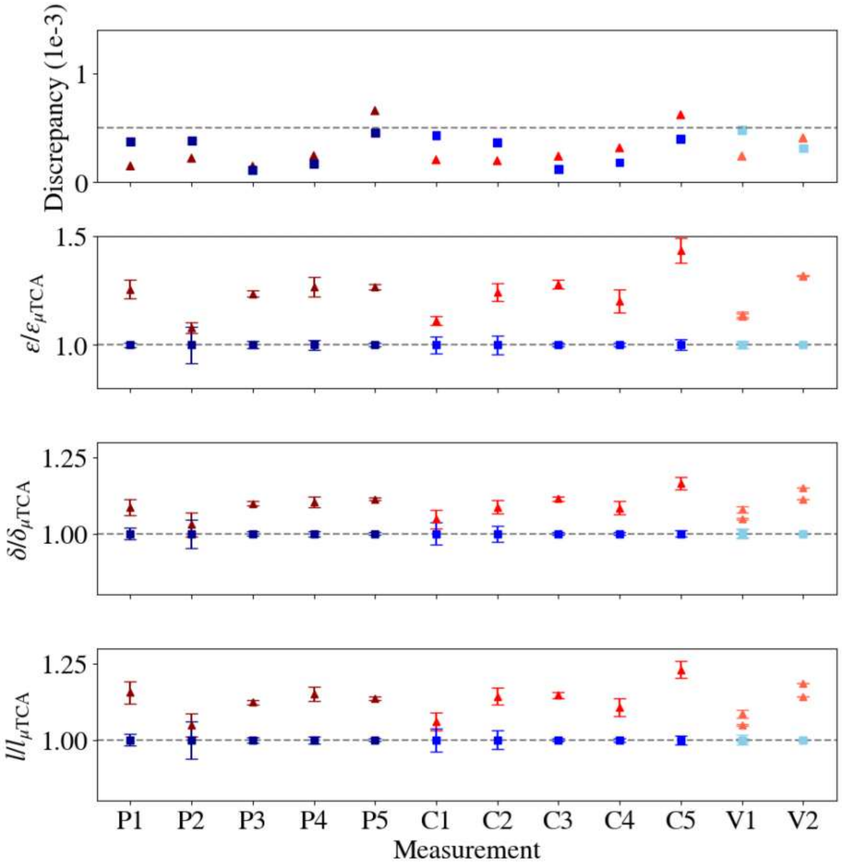

Figure 4.42: These four plots show the discrepancy of reconstructions with SADS (triangle) and µ TCA-crate (square) acquisitions in the upper plot. The emittance, the relative momentum spread and the bunch length in the plots below are the ratio of reconstructed parameters from SADS profiles to that of µTCA profiles. The two values for V1 and V2 represent the high and low momentum spread regions.

Using the simulation tool BLonD [9][15][16] provided by CERN showed that the simulated profiles could be reproduced with very high accuracy, as the discrepancy was lower than 1×10^{-3} for nearly all test cases. These test aimed at validating the reconstruction

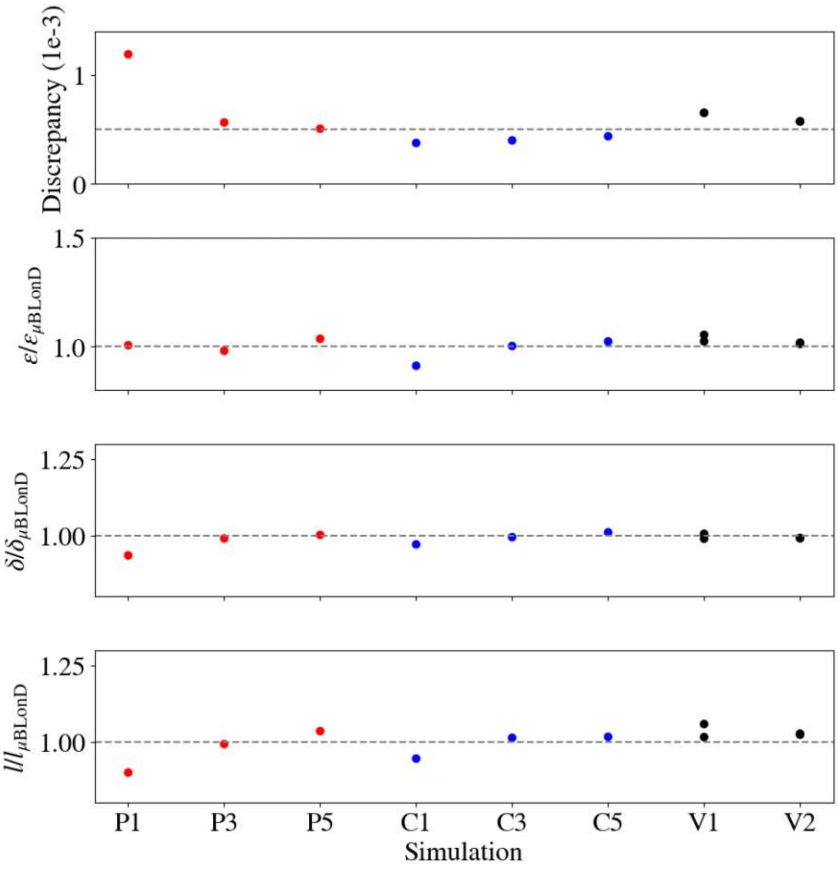

Figure 4.43: These four plots show the difference between the BLonD simulation and its reconstruction for all test cases. The first (upper) plot depicts the discrepancy of each reconstruction. The second plot shows $\frac{\epsilon_{\text{L rec}}}{\epsilon_{\text{L sim}}}$. $\frac{\delta_{\text{rec}}}{\delta_{\text{sim}}}$ and $\frac{\text{l}_{\text{rec}}}{\text{l}_{\text{sim}}}$ are depicted in the lower plots. The two values for V1 and V2 represent the high and low momentum spread regions.

independent of potential machine inaccuracies and signal distortions. All BLonD simulation were performed with the nominal voltage and B-field. The longitudinal parameters are reconstructed with high precision, even though the discrepancy is bigger than for the measurements' reconstructions. This is most likely due to the high binning in the profiles from the simulated distributions, see Fig. 4.22. The reconstruction of all BLonD simulations and their reconstructions are summarised in Fig. 4.43. The differences $\frac{\delta_{\text{rec}}}{\delta_{\text{sim}}}$ and $\frac{\text{l}_{\text{rec}}}{\text{l}_{\text{sim}}}$ are beneath 5% for all standard beams, except P1 with 7% difference of reconstructed and simulated momentum spread. The momentum spread in BLonD is calculated based on the distance from the synchronous particle. For mismatched longitudinal phase space distributions with a phase offset, this calculation is not completely correct, as the momentum and time spread should be calculated from the deviation within the projected distribution. The longitudinal beam parameters of quadrupolar-mode oscillations are calculated correctly, as the bunch is still centred. The two values at V1 and V2 representing the high and small momentum spread regions behave in a very similar way and nearly overlap for V2.

Conclusion and Outlook

This thesis shows that longitudinal tomography at MedAustron is feasible. Compared to previous methods for momentum spread measurements, Schottky frequency analyser and empty bucket scanning, the tomography offers the opportunity to measure and illustrate dynamic effects of bunched beams in the longitudinal phase space. Detailed preparatory studies analysed the available options for acquiring the required turn-by-turn longitudinal profiles at MedAustron. Using the sum Σ-signal of the orbit pick-up for the reconstruction proved to be suitable and reproducible.

Subsequent studies focused on mitigating potential errors and inaccuracies in the acquisition chain or the assumed machine parameters. A key part of these efforts was dedicated to the accurate segmentation of the acquired pick-up signals to obtain the profile of each turn with the correct phase, as described in Section 3.1.3. This was achieved by acquiring the RF signal in a second channel of the oscilloscope, while simultaneously measuring the sum signal of the pick-up. This method provides two main benefits compared to the previous attempts to segment the acquired profiles based on a revolution frequency estimate obtained via FFT. Utilising the RF measurements instead of the FFT allows to segment the profiles with higher accuracy and consequently also facilitates the selection of any point in the cycle, including during the ramp. The necessary frequency resolutions for a precise arranging of the profiles with FFT would require long acquisition times. While the µTCA-crate setup enables longer recording times, the internal data storage of the SADS does not allow long measurements with a high sampling rate (maximum 5×10^6 samples). Consequently, at the time of writing, it is more practical to use the SADS for acquiring data for tomographic reconstructions as it enables to simultaneously measure the RF signal and the beam profiles. It is recommended to implement this option for the µTCA-crate in the future. Considering the signal characteristics, the best choice for acquisition system for any use case depends on the energy range of interest. At low energies, the SADS system is preferable to the µTCA-crate, as the µTCA-crate signals feature a baseline distortion, as described in Section 4.2. For higher energies, the SADS profiles are less symmetrical than the µTCA-crate signals, which hold true for both proton and carbon. A detailed analysis of the respective signal distortions at different energies and intensities is subject to further studies. These studies include the effect of low flux beams on the acquired pick-up signals. The beams with reduced intensity (50% intensity for proton and 20% intensity for carbon beams) investigated in this thesis displayed baseline distortions (Section 4.2), which could still be used for the tomographic reconstruction with reasonably good results, see Section 4.4.1.

A key discovery, presented in Section 4.3, is the suspected RF voltage calibration error. Both, the reconstruction performance of the longitudinal tomography, as well as estimates of the synchrotron tune obtained from waterfall diagrams, of mismatched phase space distributions indicate that the RF cavity voltage is in fact $\mathrm{V}\,\{\approx 1.4 \times \mathrm{V}_{\mathrm{nom}}$, with $\mathrm{V}_{\mathrm{nom}}$ being the operationally set voltage. Subsequent RF cavity voltage measurements have been performed and provided further indications of this voltage error.

In the first implementation of longitudinal tomography at MedAustron space charge effects were neglected, due the low beam intensities. While the reconstruction of all test cases is in good agreement with the measurements, follow-up studies are recommended to asses the impact of space charge.

The developed tomography set-up and the related analysis scripts will be an invaluable diagnostic tool for the ongoing and future development of new beam manipulation techniques at MedAustron, such as multi-energy extraction or RF operation with multiple harmonics.

Bibliography

[1] S. Deycmar *et al.*, "The relative biological effectiveness of proton irradiation in dependence of DNA damage repair," *The British Journal of Radiology*, vol. 93, p. 20190494, Nov. 2019.

[2] S.-Y. Lee, *Accelerator physics*. Singapore: World Scientific Publishing Company, fourth ed., 2018.

[3] R. Steinbrügge *et al.*, "Towards multiple energy extraction operation in ion beam therapy," in *Proc. IPAC'23*, pp. 5039–5041, May 2023.

[4] F. Kuehteubl *et al.*, "Investigating alternative extraction methods at MedAustron," in *Proc. IPAC'23*, pp. 2419–2422, May 2023.

[5] CERN, "Iterative tomography - longitudinal phasespace tomography." `https://tomowebtest.docs.cern.ch/home_page/iter_tomo/iter_tomo` (accessed: 01.July 2024).

[6] D. Quartullo *et al.*, "RF Voltage Calibration Using Phase Space Tomography in the CERN SPS," in *Proc. IPAC'22*, pp. 841–844, July 2022.

[7] D. Quartullo *et al.*, "High-precision RF voltage measurements using longitudinal phase-space tomography in CERN PSB and SPS," in *Low Level RF Workshop 2023*, Oct. 2023.

[8] S. C. P. Albright *et al.*, "Two-Dimensional Longitudinal Painting at Injection into the CERN PS Booster," in *Proc. HB'23*, pp. 563–566, Mar. 2024.

[9] BLonD Development Team, "Beam Longitudinal Dynamics code (BLonD)," 2024. CERN, `http://blond.web.cern.ch` (accessed: 01.July 2024).

[10] S. Hancock, "A simple algorithm for longitudinal phase space tomography," Rep. CERN-PS-RF-NOTE-97-06, CERN, Geneva, Switzerland, May 1997.

[11] C. H. Grindheim and S. Albright, "Longitudinal phase space tomography version 3," Rep. CERN-ACC-Note-2021-0004, CERN, Geneva, Switzerland, Jan. 2021.

[12] H. Wiedemann, *Particle Accelerator Physics*. Graduate Texts in Physics, Netherlands: Springer Open, 3 ed., 2015.

[13] E. Renner, "Accelerator physics," Apr.-July 2024. Lecture at TU Wien.

[14] F. Tecker, "Longitudinal Beam Dynamics," in *CAS - CERN Accelerator School: Advanced Accelerator Physics: Trondheim, Norway 18 - 29 Aug. 2013. CAS - CERN Accelerator School: Advanced Accelerator Physics Course* (W. Herr, ed.), CERN, 2014. Organisers: Dr. Roger Bailey (Head of CAS); Barbara Strasser (CAS Assistant).

[15] BLonD Development Team, "Beam Longitudinal Dynamics Code (BLonD) ," 2024. `https://blond-admin.github.io/BLonD/index.html` (accessed: 01.July 2024).

[16] BLonD Development Team, "Beam Longitudinal Dynamics (BLonD) code GitHub," 2024. `https://github.com/blond-admin/BLonD/tree/master` (accessed: 01.July 2024).

[17] A. Verdier, "Chromaticity (particle accelerators)," 1995.

[18] M. Barnes *et al.*, "Injection and extraction magnets: septa," , presented at the CERN Accelerator School CAS 2009: Specialised Course on Magnets, Bruges, June 2009.

[19] M. Barnes, "Kicker systems," *CERN Yellow Rep. School Proc.*, vol. 5, p. 229, 2018.

[20] P. Baudrenghien, "Low-level RF - Part I: Longitudinal dynamics and beam-based loops in synchrotrons," contribution to the CERN Accelerator School CAS: Specialised Course on RF for Accelerators, Ebeltoft, June 2010.

[21] F. Gerigk, "Cavity types," 2011. presented at the CERN Accelerator School CAS 2010: RF for Accelerators, Ebeltoft, June 2010.

[22] R. Williamson, "Accelerator Physics Lecture 6: Longitudinal Dynamics," Oct. 2019. Lecture at John Adams Institute for Accelerator Science.

[23] M. Pivi and A. Garonna, "Space Charge Effect Estimation for Synchrotrons with Third-order Resonant Extraction," in *Proc. IPAC'15*, pp. 3677–3679, June 2015.

[24] K. Lasocha and D. Alves, "Estimation of longitudinal bunch characteristics in the LHC using Schottky-based diagnostics," *Physical Review Accelerators and Beams*, vol. 23, no. 6, p. 062803, 2020.

[25] BLonD Admin, "BLonD: Kick.cpp." `https://github.com/blond-admin/BLonD/blob/a3a0c986399048f13a6ff769d2b9a76cecbbdfae/blond/cpp_routines/kick.cpp` (accessed: 01.July 2024).

[26] K. L. Wininger, "Basis of CT: the Radon transform," *Radiologic technology*, vol. 84, no. 4, pp. 413–418, 2013.

[27] P. Glendinning, “View from the Pennines: Using Maths I, Tomography and Johann Radon,” *Mathematics Today-Bulletin of the Institute of Mathematics and its Applications*, vol. 42, no. 4, pp. 132–133, 2006.

[28] J. Gareyte, “LHC main parameters,” *Particle Accelerators*, vol. 50, pp. 61–68, 1995.

[29] R. Gordon, “A tutorial on ART (algebraic reconstruction techniques),” *IEEE Transactions on Nuclear Science*, vol. 21, no. 3, pp. 78–93, 1974.

[30] B. Abreu Figueiredo, “Evaluation of Different Methods for Runtime Optimization of Longitudinal Phase Space Tomography,” 2024. presented 11 Mar. 2024 at Hochschule Karlsruhe.

[31] M. Pivi, “The medaustron particle therapy accelerator facility,” *Health Technology*, 2024.

[32] F. Ulrich-Pur *et al.*, “Commissioning of low particle flux for proton beams at MedAustron,” *Nuclear Instruments and Methods in Physics Research Section A: Accelerators, Spectrometers, Detectors and Associated Equipment*, vol. 1010, p. 165570, Sep. 2021.

[33] M. Kausel *et al.*, “Injector and synchrotron commissioning of helium ion beams at the MedAustron Ion Therapy Center,” in *Proc. IPAC’23*, IPAC’23, pp. 1713–1716, May 2023.

[34] U. Ratzinger, “H-type linac structures,” 2005.

[35] L. Badano *et al.*, *Proton-Ion Medical Machine Study (PIMMS), 1.* 2000.

[36] C. Schmitzer *et al.*, “MedAustron Synchrotron RF Commissioning for Medical Proton Beams,” in *Proc. IPAC’16*, pp. 844–846, June 2016.

[37] M. Wolf *et al.*, “Development and Integration of a New Low-Level RF System for MedAustron,” in *Proc. LINAC’22*, pp. 764–766, Sep. 2022.

[38] S. Simrock and M. Grecki, “LLRF & HPRF Cavity Field Control - Cavity Theory,” in *5th LC School*, 2010. LLRF Lecture Part 3.1, ITER / DESY.

[39] M. Repovž *et al.*, “Development of a New Measurement System for Beam Position Pickups in the LINAC and Beam Energy Measurement (Time of Flight) in the MEBT for Medaustron,” in *Proc. IBIC’22*, pp. 238–240, Dec. 2022.

[40] MedAustron, “Internal technical documentation.”

[41] R. Cappi and C. Steinbach, “Low Frequency Duty Factor Improvement for the CERN PS Slow Extraction Using RF Phase Displacement Techniques,” *IEEE Transactions on Nuclear Science*, vol. 28, no. 3, pp. 2806–2808, 1981.

[42] A. De Franco *et al.*, “Slow Extraction Optimization at the MedAustron Ion Therapy Center: Implementation of Front End Acceleration and RF Knock Out,” in *Proc. IPAC’18*, pp. 453–456, June 2018.

[43] P. Forck. Lecture on Beam Instrumentation and Diagnostics at the Joint University Accelerator School (JUAS), `http://www-bd.gsi.de/conf/juas/juas.html` (accessed: 12.Nov. 2023).

[44] D. Kelliher *et al.*, “Longitudinal Tomography in a Scaling FFA,” in *Proc. IPAC’19*, pp. 719–722, June 2019.

[45] R. Singh, P. Forck, and P. Kowina, “Tutorial on beam measurements using schottky signal analysis.” presented at IBIC’17, Grand Rapids, MI, USA, Aug. 2017.

[46] V. Balbekov and S. Nagaitsev, “Longitudinal Schottky Spectra of Bunched Beams,” in *Proc. EPAC 2004*, July 2004.

[47] F. Kuehteubl, “Private communications.” (23.Apr. 2024).

[48] M. Wolf, “Private communications.” (19.Jan. 2024).

[49] S. Albright, “Private communications.” (17.May 2024).

[50] S. Albright, “Phasespacetomography - github repository,” 2019. `https://github.com/PhaseSpaceTomography/longitudinal-tomography` (accessed: 01.July 2024).

Appendices

A.1: BLonD Simulation and Reconstruction of Constant Frequency Offset

Figure A.1.1 shows the longitudinal profiles gained from the BLonD simulation within one synchrotron period. These profiles are used in the reconstruction, depicted in Figure A.1.2. As for the measurements acquired with the SADS and µTCA-crate, which can be found in Section 4.4.2, the reconstruction accurately depicts the beam's behaviour in the longitudinal phase space.

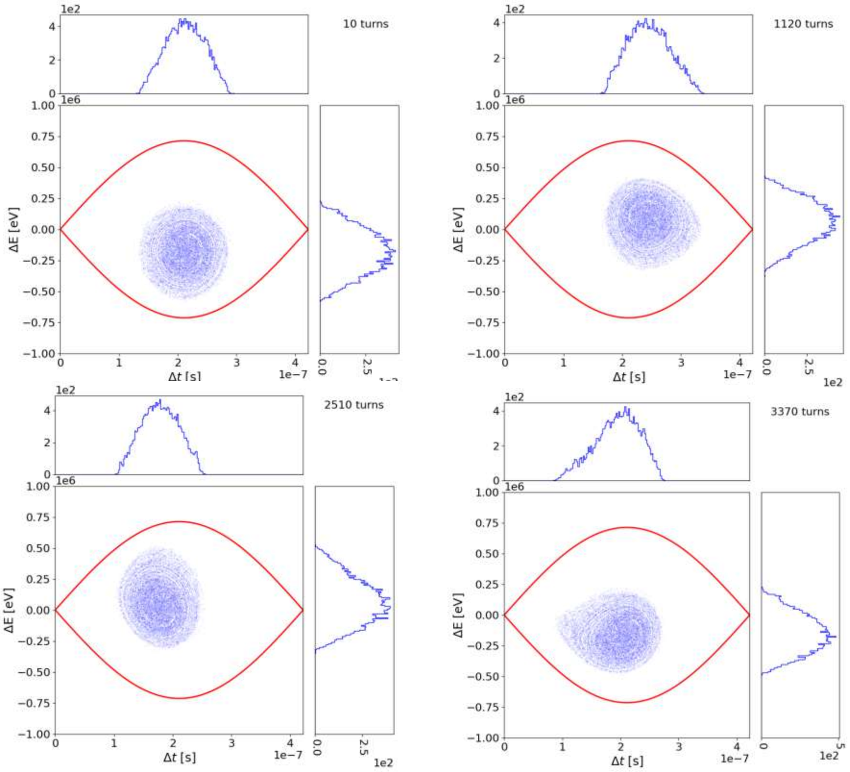

Figure A.1.1: Longitudinal profile gained from BLonD simulation with changed circumference and initial distribution shifted down to simulate the frequency shift, test case K1.

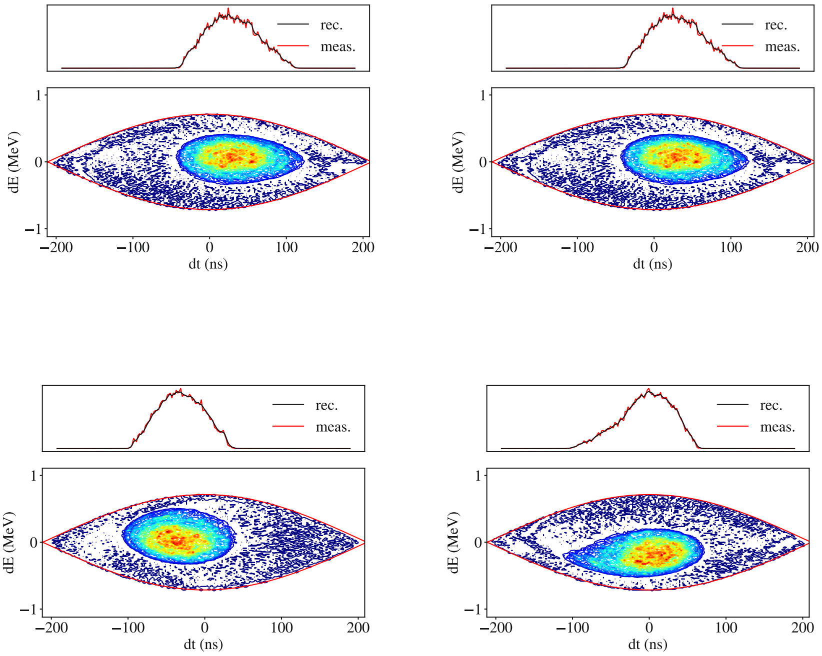

Figure A.1.2: Reconstruction of BLonD simulation shown above.

A.2: Example of Input File for Tomography

Here an example of the structure in the input file, required by the tomography algorithm [50], is given. The description of the parameters can be found in Section 3.2.1. This structure should not be changed, if rewrites are to be avoided.

```








! Version 2
!
! Data Format:
! Input data file =
pipe
! Directory in which to write all output =
/tmp/
! Number of frames in input data =
400
! Number of frames to ignore =
0
! Number of bins in each frame =
427
! Width (in s) of each frame bin =
1e-09
! Number of machine turns between frames =
10
! Number of frame bins before the lower profile bound to ignore =
80
! Number of frame bins after the upper profile bound to ignore =
10
! Number of frame bins after the lower profile bound to treat as empty
! at the reconstructed time =
0
! Number of frame bins before the upper profile bound to treat as empty
! at the reconstructed time =
0
! Number of frame bins to rebin into one profile bin =
1
! Time (in frame bins) from the lower profile bound to the synchronous phase
! (if <0, a fit is performed) in the "bunch reference" frame =
178
! Max energy (in eV) of reconstructed phase space (if >0) =
-2000000.0
! Number of the first profile at which to reconstruct =
1
! Number of the last profile at which to reconstruct =
400
! Step between reconstructions =
```

```
10
! Number of iterations for each reconstruction =
50
! Square root of the number of test particles to track per cell =
3
! Flag to extend the region in phase space of map elements (if =1) =
1
! Reference frame for bunch parameters (synchronous phase, baseline, integral
    ) =
1
! Reference frame for machine parameters (RF voltages, B-field) =
1
!
! Machine and Particle Parameters:
! Peak RF voltage (in V) of principal RF system =
938.3589829057961
! and its time derivative (in V/s) =
0.0
! Peak RF voltage (in V) of higher-harmonic RF system =
0.0
! and its time derivative (in V/s) =
0.0
! Harmonic number of principal RF system =
1
! Ratio of harmonics between RF systems =
1.0
! Phase difference (in radians of the principal harmonic) between RF systems
    =
0.0
! Dipole magnetic field (in T) =
0.5723
! and its time derivative (in T/s) =
0.0
! Machine radius (in m) =
12.359074
! Bending radius (in m) =
4.251506377
! Gamma transition =
1.99
! Rest mass (in eV/c**2) of accelerated particle =
938272310.0
! Charge state of accelerated particle =
1
!
! Space Charge Parameters:
! Flag to include self-fields in the tracking (if =1) =
0
! Geometrical coupling coefficient =
0.0
! Reactive impedance (in Ohms per mode number) over a machine turn =
0.0
! Effective pick-up sensitivity (in digitizer units per instantaneous Amp) =
0.69
```

```
-3671.0
-3654.0
-3669.0
-3683.0
-3671.0
-3682.0
-3681.0
-3682.0
-3696.0
-3690.0
+ rest of frame data.
```

A.3: Supplementary Information to the Acquisition Systems

This is an addendum to the acquisition systems described in Section 3.1.2.

µTCA-crate: The essential components of the µTCA-architecture are [37][47]:

- **Vadatech AMC560**: The field programmable gate array (FPGA) carrier provides the computational power needed to connect the supervision systems and offer a local control interface. The baseband conversion and cavity regulation is done by the FPGA.
- **Vadatech FMC231**: A board providing a AD/DAC (analog-digital/ digital-analog converter) with 16bit conversion at 1 GS/s or 2.5 GS/s on 4 channels.
- **Vadatech FMC105**: The FPGA module connects to the MedAustron Control System, which acts as the supervising system, via fibre optic links.
- **Vadatech FMC155**: The general purpose input/output (GPIO) on the FPGA carrier are used for interlocks and modbus for the eigenfrequency regulation of the RF-cavity.
- **Vadatech UTC004**: µTCA architecture.

SADS: Further components of the SADS [40] include the peripheral component interconnect extensions express (PXIe), which offers a bus system with high band to connect the fast input signals to one oscilloscope via the timing receiver and the fast signal multiplex. The two other oscilloscopes can connect to up to 4 slow analogue signals and external triggers via signal matrices, which are controlled by the signal routing control application via a LAN extensions for instrumentation (LXI) based network interface.